

1

# UNIVERSITY OF BRISTOL

2

## DOCTORAL THESIS

3

4

# Investigating, implementing, and creating methods for analysing large neuronal ensembles

5

6

7

*Author:*

Thomas J. DELANEY

*Supervisors:*

Dr. Cian O'DONNELL

Dr. Michael C. ASHBY

8

*A thesis submitted in fulfillment of the requirements*

*for the degree of Doctor of Philosophy*

9

*in the*

10

Biological Intelligence & Machine Learning Unit

11

Department of Computer Science

12

July 13, 2020

13

Word count: 39000



<sup>16</sup> **Declaration of Authorship**

<sup>17</sup> I declare that the work in this dissertation was carried out in accordance with the requirements of the University's Regulations and Code of Practice for Research Degree Programmes  
<sup>18</sup> and that it has not been submitted for any other academic award. Except where indicated by  
<sup>19</sup> specific reference in the text, the work is the candidate's own work. Work done in collabora-  
<sup>20</sup> tion with, or with the assistance of, others, is indicated as such. Any views expressed in the  
<sup>21</sup> dissertation are those of the author.

<sup>22</sup> Signed:

<sup>23</sup> \_\_\_\_\_

<sup>24</sup> Date:

<sup>25</sup> \_\_\_\_\_



## *Acknowledgements*

28 I would like to thank my supervisors, Cian O'Donnell and Mike Ashby, for their help, en-  
29 couragement, advice, and patience over the last four years. This includes not only helping  
30 with research, but also enabling and encouraging me to make the most of my opportunities  
31 during that time. Without their help, I would not have grown as much as I have done in those  
32 years. I very grateful for their time and effort.

33 I would also like to thank the members of the Bristol Computational Neuroscience Unit  
34 for introducing me to all the various aspects of computer science, neuroscience, and machine  
35 learning, of which I otherwise would not have heard. As the first person to introduce me to  
36 the concept of mathematical neuroscience during my undergraduate days, and a great source  
37 of advice and guidance during my PhD, I would also like to thank Conor Houghton.

38 Personally, I would to thank my girlfriend Ashley, who has been nothing but helpful since  
39 I met her.

40 Finally, I would like to that my father, mother, brother and sister. I am truly fortunate to  
41 have such a good family. I thank them for their love, encouragement, and excellent example.



## 42 *Abstract*

43 Since the use of multi-electrode recording in neuroscience began, the number neurons  
44 being recorded in parallel has been increasing. Recently developed methods using calcium  
45 or voltage imaging have also contributed to the growth in neuronal datasets. As datasets grow,  
46 the need for new analysis methods also grows. In this research we attempted to address some  
47 of the problems associated with reading from large neuronal ensembles using fluorescent  
48 calcium indicators, and some of the problems with analysing data read from large neuronal  
49 ensembles.

50 We created a biophysical model for the fluorescence trace produced by a calcium indicator  
51 responding to a given spike train. Our model reproduced the characteristics of a real  
52 fluorescence trace recognised by spike inference algorithms. This model will be useful for  
53 anyone using or considering calcium imaging.

54 To find order in the correlated behaviour of a large multi-region neuronal ensemble, we  
55 applied a novel method from network science to detect structure and communities in corre-  
56 lated behaviour. We investigated the similarities between these communities and their brain  
57 anatomy. Our results indicate local correlated networks function at shorter timescales (<  
58 50ms), while multi-region correlated networks function over longer timescales (> 100ms).  
59 This result agrees with previous findings from EEG data, but has not been shown before using  
60 spiking data.

61 We developed a statistical model for the number of neurons spiking in a neuronal ensem-  
62 ble based on the Conway-Maxwell-binomial distribution. Our aim was to capture correlated  
63 activity in a neuronal population without measuring correlation coefficients directly. The  
64 model captured correlated activity at very short timescales better than measuring correlation  
65 coefficients. We also replicated one of the findings of Churchland et al. (2010) relating to  
66 the quenching of neural variability at stimulus onset. We propose a connection between this  
67 result and the changes in association captured by our model.



# 68 **Contents**

69	<b>Declaration of Authorship</b>	iii
70	<b>Acknowledgements</b>	v
71	<b>Abstract</b>	vii
72	<b>1 Introduction</b>	1
73	1.1 Overview . . . . .	1
74	1.2 Modelling the fluorescence of calcium indicators . . . . .	2
75	1.3 Functional networks . . . . .	4
76	1.4 A new statistical model for capturing correlated behaviour . . . . .	6
77	<b>2 Sensitivity of the spikes-to-fluorescence transform to calcium indicator and neu-</b>	
78	<b>ron properties</b>	9
79	2.1 Introduction . . . . .	10
80	2.2 Methods . . . . .	12
81	2.2.1 Calcium dynamics model . . . . .	12
82	Photon release & capture . . . . .	14
83	2.2.2 Parameter optimisation . . . . .	15
84	Fixed parameters . . . . .	16
85	2.2.3 Julia . . . . .	18
86	2.2.4 Spike inference . . . . .	18
87	Comparing spike inference quality . . . . .	20
88	2.2.5 Perturbation analysis . . . . .	20
89	2.2.6 Signal-to-noise ratio . . . . .	21
90	2.2.7 Data sources . . . . .	21
91	2.3 Results . . . . .	21
92	2.3.1 A biophysical computational model can generate accurate fluores-	
93	cence traces from spike trains . . . . .	21

94	2.3.2	Spike inference algorithms perform similarly on real data compared with time series simulated from the model . . . . .	22
95	2.3.3	Relative effects of various buffers to the fluorescence signal . . . . .	24
96	2.3.4	Spike inference accuracy is sensitive to indicator properties, and likely varies within and between cells . . . . .	26
97	2.3.5	Single spike inference accuracy drops for high firing rates, but firing rate itself can be estimated from mean fluorescence amplitude . . . . .	31
98	2.4	Discussion . . . . .	31
102	<b>3</b>	<b>Functional networks expand across anatomical boundaries as correlation time- scale increases</b>	<b>35</b>
103	3.1	Introduction . . . . .	36
104	3.2	Data . . . . .	37
105	3.2.1	Brain regions . . . . .	37
106	3.2.2	Video recordings . . . . .	38
107	3.3	Methods . . . . .	38
108	3.3.1	Binning data . . . . .	38
109	3.3.2	Correlation coefficients . . . . .	39
110		Total correlations, $r_{SC}$ . . . . .	39
111		Shuffled total correlations . . . . .	40
112		Separating Correlations & Anti-correlations . . . . .	40
113	3.3.3	Conditioning on behavioural data . . . . .	40
114		Linear regression . . . . .	40
115		Elastic net regularisation . . . . .	41
116		Conditional covariance . . . . .	42
117		Measures of conditional correlation . . . . .	42
118	3.3.4	Information Theory . . . . .	43
119		Entropy $H(X)$ . . . . .	43
120		Maximum entropy limit . . . . .	44
121		Mutual Information $I(X; Y)$ . . . . .	45
122		Variation of Information $VI(X, Y)$ . . . . .	46
123		Measuring entropies & mutual information . . . . .	46
124	3.3.5	Network analysis . . . . .	47
125		Correlation networks . . . . .	47

127	Rectified correlations . . . . .	47
128	Sparsifying data networks . . . . .	47
129	Communities . . . . .	47
130	Weighted configuration model . . . . .	48
131	Sparse weighted configuration model . . . . .	48
132	Spectral rejection . . . . .	48
133	Node rejection . . . . .	49
134	Community detection . . . . .	50
135	3.3.6 Clustering Comparison . . . . .	50
136	Adjusted Rand Index . . . . .	50
137	Clusterings as random variables . . . . .	51
138	Information based similarity measures . . . . .	52
139	Information based metrics . . . . .	53
140	Comparing detected communities and anatomical divisions . . . . .	53
141	3.4 Results . . . . .	54
142	3.4.1 Average correlation size increases with increasing time bin width . .	54
143	3.4.2 Goodness-of-fit for Poisson and Gaussian distributions across increasing time bin widths . . . . .	55
144	3.4.3 Differences between and inter- and intra- regional correlations decrease with increasing bin width . . . . .	57
145	3.4.4 Connected and divided structure in correlation based networks reduces in dimension with increasing bin width . . . . .	58
146	3.4.5 Detecting communities in correlation based networks . . . . .	62
147	3.4.6 Functional communities resemble anatomical division at short timescales	62
148	3.4.7 Conditional correlations & signal correlations . . . . .	64
149	3.4.8 Absolute correlations and negative rectified correlations . . . . .	68
150	3.5 Discussion . . . . .	72
151	<b>4 A simple two parameter distribution for modelling neuronal activity and capturing neuronal association</b>	<b>75</b>
152	4.1 Introduction . . . . .	76
153	4.2 Data . . . . .	77
154	4.2.1 Experimental protocol . . . . .	77
155	4.3 Methods . . . . .	78

160	4.3.1	Binning data . . . . .	78
161	4.3.2	Number of <i>active</i> neurons . . . . .	78
162	4.3.3	Moving windows for measurements . . . . .	78
163	4.3.4	Fano factor . . . . .	80
164	4.3.5	Probability Distributions suitable for modelling ensemble activity . . . . .	80
165		Association . . . . .	80
166		Binomial distribution . . . . .	81
167		Beta-binomial distribution . . . . .	81
168		Conway-Maxwell-binomial distribution . . . . .	82
169	4.3.6	Fitting . . . . .	84
170	4.3.7	Goodness-of-fit . . . . .	86
171	4.4	Results . . . . .	86
172	4.4.1	Increases in mean number of active neurons and variance in number of active neurons at stimulus onset in some regions . . . . .	86
173		Primary visual cortex . . . . .	87
174		Hippocampus . . . . .	87
175		Thalamus . . . . .	87
176	4.4.2	Conway-Maxwell-binomial distribution is usually a better fit than binomial or beta-binomial . . . . .	87
177	4.4.3	Conway-Maxwell-binomial distribution captures changes in association at stimulus onset . . . . .	92
178	4.4.4	Replicating stimulus related quenching of neural variability . . . . .	92
179	4.5	Discussion . . . . .	94
183	<b>5</b>	<b>Studies with practical limitations &amp; negative results</b>	<b>97</b>
184	5.1	Dynamic state space model of pairwise and higher order neuronal correlations	98
185	5.2	A multiscale model for hierarchical data applied to neuronal data . . . . .	98
187	<b>6</b>	<b>Discussion</b>	<b>101</b>
188	<b>Bibliography</b>		<b>109</b>

# <sup>189</sup> List of Figures

190	2.1 A: Example spike train (blue) and the corresponding GCaMP6s fluorescence	
191	trace (green), data replotted from (Berens et al., 2018). Inset shows zoomed	
192	section of traces to highlight slow decay of GCaMP6s fluorescence relative	
193	to spike time intervals. B: Schematic diagram of the neuron calcium and	
194	GCaMP computational model. C: Good visual match of data fluorescence	
195	trace (green) and model simulated fluorescence (orange) in response to an	
196	identical spike train (blue). . . . .	11
197	2.2 A: Workflow to compare spike inference for real versus simulated fluores-	
198	cence data. B: True positive rates achieved by three different spike inference	
199	algorithms when applied to observed spike trains, and simulated spike trains.	
200	Data points overlaid as blue circles. The performance is similar from real	
201	and simulated data for each of the algorithms. . . . .	23
202	2.3 <b>Calcium Buffering Dynamics</b> (A) The proportions of bound and free cal-	
203	cium concentrations within a cell, with the associated spike train. (B)-(F)	
204	The dynamics of the concentration of (B) excited indicator bound calcium,	
205	(C) indicator bound calcium, (D) immobile endogenous buffer bound cal-	
206	cium, (E) mobile endogenous buffer bound calcium, and (F) free calcium in	
207	response to an action potential at $\sim 23.2\text{s}$ . . . . .	25
208	2.4 (A) An example trace for each of the five pairs of values used for the binding	
209	and unbinding rates of the fluorescent calcium indicator. (B) The signal-to-	
210	noise ratio of the modelled fluorescence traces using each of the four per-	
211	turbed value pairs, and the experimental value. The SNRs for the value pairs	
212	perturbed downward are lower than that for the unperturbed value pair or	
213	the higher value pairs. (C) The true-positive rates of the deconvolution al-	
214	gorithm's predictions when inferring from the observed data, and inferring	
215	from modelled traces using the perturbed and experimental values. . . . .	27

216	2.5 (A) An example trace for each of the five perturbed values for the concen-	
217	tration of fluorescent calcium indicator. The top two traces are produced	
218	by the lower perturbed values, the middle trace is produced by the experi-	
219	mental value, and the lowest two traces are produced when using the higher	
220	perturbed values. (B) The signal-to-noise ratio of the modelled fluorescence	
221	traces using each of the four perturbed values, and the experimental value.	
222	Extreme perturbations of the concentration either above or below the experi-	
223	mental level lowered the SNR. (C) The true-positive rates of the deconvolu-	
224	tion algorithm's predictions when inferring from the observed data, and	
225	inferring from modelled traces using the perturbed and experimental values.	
226	We found that the algorithms performs equally badly on the two most ex-	
227	treme values, and performs equally well on the experimental value, and the	
228	next higher perturbed value. . . . .	28
229	2.6 (A) An example trace for each of the five perturbed values for the concen-	
230	tration of immobile endogenous buffer. (B) The signal-to-noise ratio of the	
231	modelled fluorescence traces using each of the four perturbed values, and	
232	the experimental value. The lower values for the immobile buffer produce	
233	the same SNR as the experimental value. But the higher perturbed values	
234	produce fluorescence traces with a lower SNR. (C) The true-positive rates of	
235	the deconvolution algorithm's predictions when inferring from the observed	
236	data, and inferring from modelled traces using the perturbed and experimen-	
237	tal values. . . . .	30
238	2.7 <b>Simulating fluorescence traces at different firing rates</b> Example modelled	
239	traces created using simulated spike trains with a mean firing rate of 1Hz	
240	(left column), 5Hz (middle column), and 10Hz (right column). Note the	
241	difference in amplitude with different mean firing rates. . . . .	32
242	2.8 <b>Inference quality and <math>\Delta F/F_0</math> vs Firing rate</b> (left) The spike inference ac-	
243	curacy when applied to 30 traces created using simulated spike trains with	
244	mean firing rates of 1, 5, and 10 Hz. (right) The mean $\Delta F/F_0$ across those	
245	30 traces for each frequency. . . . .	32
246	3.1 <b>Probe Locations:</b> The locations of the probes in each of the three mouse	
247	brains (Stringer et al., 2019). . . . .	38

248	3.2	<b>Entropy Limit:</b> The upper limit on entropy of binned spike count data as a function of the maximum observed spike count. The orange line is the analytical maximum. The blue line is the entropy of samples with $N = 1000$ data points taken from the discrete uniform distribution. . . . .	44
252	3.3	(A) An example of the correlation coefficients between two different pairs of cells, one where both cells are in the same brain region (intra-regional pair), and one where both cells are in different brain regions (inter-regional pair). The correlation coefficients have been measured using different time bin widths, ranging from 5ms to 3s. Note the increasing amplitude of the correlations with increasing bin width. (B) A raster plot showing the spike times of each pair of cells. . . . .	54
256	3.4	Mean correlation coefficients measured from pairs of 50 randomly chosen neurons. (A) All possible pairs, (B) positively correlated pairs, and (C) neg- atively correlated pairs. (D) Mean and standard error of $\chi^2$ test statistics for Poisson and Gaussian distributions fitted to neuron spike counts. . . . .	56
260	3.5	(Left)The mean intra-region and inter-region correlations using all possible pairs of $\sim 500$ neurons, spread across 9 different brain regions. (Right) Courtesy of Stringer et al. (2019), mean inter-regional (out-of-area) correla- tion coefficients vs mean intra-regional (within-area) correlation coefficients for a bin width of 1.2s. Note that the intra-regional coefficients are higher in each case. . . . .	58
264	3.6	The mean intra-regional correlations (coloured dots) and mean inter-regional correlations (black dots) for a given region, indicated on the x-axis, for dif- ferent time bin widths. Each black dot represents the mean inter-regional correlations between the region indicated on the x-axis and one other region. (A) shows these measurements when we used a time bin width of 5ms. (B) shows these measurements when we used a time bin width of 1s. Note that the difference between the mean inter-regional correlations and mean intra- regional correlations is smaller for 1s bins. . . . .	59
268	3.7	Mean inter-regional (main diagonal) and intra-regional (off diagonal) corre- lation coefficients. (A) Shows these measurements when spike times were binned using 5ms time bins. (B) Shows the same, using 1s time bins. Note that the matrices are ordered according to the main diagonal values, therefore the ordering is different in each subfigure. . . . .	60

282	3.8 The number of dimensions in the $k$ -partite and connected structure in the cor-	
283	relation based networks beyond the structure captured by a sparse weighted	
284	configuration null network model (see section 3.3.5), shown for different time	
285	bin widths. Note that the $k$ -partite structure disappears for time bin width	
286	greater than 200ms for all three subjects. The dimension of the connected	
287	structure reduces with increasing bin width for 2 of the 3 subjects (top row). . . . .	61
288	3.9 (A-B) Correlation matrices with detected communities indicated by white	
289	lines. Each off main diagonal entry in the matrix represents a pair of neu-	
290	rons. Those entries within a white square indicate that both of those neurons	
291	are in the same community as detected by our community detection proce-	
292	dure. Matrices shown are for 5ms and 1s time bin widths respectively. Main	
293	diagonal entries were set to 0. (C-D) Matrices showing the anatomical dis-	
294	tribution of pairs along with their community membership. Entries where	
295	both cells are in the same region are given a colour indicated by the colour	
296	bar. Entries where cells are in different regions are given the grey colour also	
297	indicated by the colour bar. . . . .	63
298	3.10 (A) The variation of information is a measure of distance between cluster-	
299	ings. The distance between the anatomical ‘clustering’ and community de-	
300	tection ‘clustering’ increases with increasing time bin width. (B) The ad-	
301	justed Rand index is a normalised similarity measure between clusterings.	
302	The anatomical and community detection clusterings become less similar as	
303	the time bin width increases. . . . .	64
304	3.11 Comparing the components of the total covariance across different values for	
305	the time bin width. We observed a consistent increase in $E[\text{cov}(X, Y Z)]$ as	
306	the time bin width increased. But we saw different trends for $\text{cov}(E[X Z], E[Y Z])$	
307	for each mouse. . . . .	65
308	3.12 Comparing the components of the total covariance across different values for	
309	the time bin width. We saw a consistent increase in $\rho_{X,Y Z}$ as the time bin	
310	width increased in all three subjects. But we saw different trends in $\rho_{\text{signal}}$ for	
311	each of the subjects. . . . .	66

312	3.13 Matrices showing the regional membership of pairs by colour, and the com-	
313	munities in which those pairs lie. (A-B) Detected communities and regional	
314	membership matrix for network based on rectified spike count correlation	
315	$\rho_{X,Y Z}$ , using time bin widths of 0.005s and 1s respectively. (C-D) Detected	
316	communities and regional membership matrix for network based on rectified	
317	signal correlation $\rho_{\text{signal}}$ , using time bin widths of 0.005s and 1s respectively.	67
318	3.14 Distance and similarity measures between the anatomical division of the neu-	
319	rons, and the communities detected in the network based on the spike count	
320	correlations $\rho_{X,Y Z}$ . (A) The variation of information is a ‘distance’ mea-	
321	sure between clusterings. The distance between the anatomical ‘clustering’	
322	and the community clustering increases as the time bin width increases. (B)	
323	The adjusted Rand index is a similarity measure between clusterings. The	
324	detected communities become less similar to the anatomical division of the	
325	cells as the time bin width increases. . . . .	68
326	3.15 Distance and similarity measures between the anatomical division of the neu-	
327	rons, and the communities detected in the network based on the signal cor-	
328	relations $\rho_{\text{signal}}$ . (A) The variation of information is a ‘distance’ measure be-	
329	tween clusterings. The distance between the anatomical ‘clustering’ and the	
330	community clustering increases as the time bin width increases. (B) The ad-	
331	justed Rand index is a similarity measure between clusterings. The detected	
332	communities become less similar to the anatomical division of the cells as	
333	the time bin width increases. . . . .	69
334	3.16 (A-B) Absolute correlation matrices with detected communities indicated by	
335	white lines. These communities are based on the absolute value of the total	
336	correlation between each pair of cells. Those entries within a white square in-	
337	dicate that both of those neurons are in the same community. Matrices shown	
338	are for 5ms and 1s time bin widths respectively. Main diagonal entries were	
339	set to 0. (C-D) Matrices showing the anatomical distribution of pairs along	
340	with their community membership. Regional membership is indicated by the	
341	colour bar. (E) Variation of information between the anatomical division of	
342	the cells, and the detected communities. (F) Adjusted Rand index between	
343	the anatomical division, and the detected communities. . . . .	70

344	3.17 (A-B) Sign reversed rectified correlation matrices with detected communities indicated by white lines. Those entries within a white square indicate that both of those neurons are in the same community. Matrices shown are for 5ms and 1s time bin widths respectively. Main diagonal entries were set to 0. (C-D) Matrices showing the anatomical distribution of pairs along with their community membership. Regional membership is indicated by the colour bar. (E) Variation of information between the anatomical division of the cells, and the detected communities. (F) Adjusted Rand index between the anatomical division, and the detected communities. . . . .	71
353	4.1 Figures showing the over-dispersion possible for a beta-binomial distribution relative to a binomial distribution. Parameters are shown in the captions. . .	82
355	4.2 Figures showing (A) the under-dispersion and (B) over-dispersion permitted by the COMb distribution relative to a binomial distribution. (C) illustrates that the $p$ parameter of the COMb distribution does not correspond to the mean of the distribution, as it does for the binomial and beta-binomial distributions. (D) shows a heatmap for the value of the Kullback-Liebler divergence between the COMb distribution and the standard binomial distribution with same value for $n$ , as a function of $p$ and $\nu$ . Parameters are shown in the captions. . . . .	85
363	4.3 (A) Raster plot showing the spikes fired by 33 randomly chosen neurons in the primary visual cortex. (B-C) (B) average and (C) variance of the number of active neurons, measured using a sliding window 100ms wide, split into 100 bins. The midpoint of the time interval for each window is used as the timepoint (x-axis point) for the measurements using that window. The grey shaded area indicates the presence of a visual stimulus. The opaque line is an average across the 160 trials that included a visual stimulus of any kind. We can see a transient increase in the average number of active neurons and the variance of this number, followed by a fluctuation and another increase. .	88

372	4.4 (A) Raster plot showing the spikes fired by 33 randomly chosen neurons in	
373	the hippocampus. (B-C) (B) average and (C) variance of the number of active	
374	neurons, measured using a sliding window 100ms wide, split into 100 bins.	
375	The midpoint of the time interval for each window is used as the timepoint (x-	
376	axis point) for the measurements using that window. The grey shaded area	
377	indicates the presence of a visual stimulus. The opaque line is an average	
378	across the 160 trials that included a visual stimulus of any kind. We can see	
379	a transient increase in the average number of active neurons and the variance	
380	of this number at stimulus onset. . . . .	89
381	4.5 (A) Raster plot showing the spikes fired by 33 randomly chosen neurons in	
382	the thalamus. (B-C) (B) average and (C) variance of the number of active	
383	neurons, measured using a sliding window 100ms wide, split into 100 bins.	
384	The midpoint of the time interval for each window is used as the timepoint (x-	
385	axis point) for the measurements using that window. The grey shaded area	
386	indicates the presence of a visual stimulus. The opaque line is an average	
387	across the 160 trials that included a visual stimulus of any kind. We can	
388	see in immediate increase at stimulus onset, a subsequent fall, and another	
389	sustained increased until the stimulus presentation ends. . . . .	90
390	4.6 (A) An example of the binomial, beta-binomial, and Conway-Maxwell-binomial	
391	distributions fitted to a sample of neural activity. The Conway-Maxwell-	
392	binomial distribution is the best fit in this case. The histogram shows the	
393	empirical distribution of the sample. The probability mass function of each	
394	distribution is indicated by a different coloured line. (B) Across all samples	
395	in all trials, the proportion of samples for which each fitted distribution was	
396	the the best fit. The Conway-Maxwell-binomial distribution was the best fit	
397	for 93% of the samples taken from V1 using a bin width of 1ms. . . . .	91

398	4.7 (A) We fit a Conway-Maxwell-binomial distribution to the number of active	
399	neurons in 1ms time bins of a 100ms sliding window. We did this for all	
400	trials with a visual stimulus and took the average across those trials. We see	
401	a transient drop in value for the distribution's $\nu$ parameter at stimulus onset.	
402	This shows an increase in positive association between the neurons. (B) We	
403	measured the correlation coefficient between the spike counts of all possible	
404	pairs of neurons in the same sliding window. The took the average of those	
405	coefficients. We also did this for every visually stimulated trial, and took the	
406	average across trials. The increase in positive association is not reflected with	
407	an increase in average correlation. . . . .	93
408	4.8 (A) The mean Fano factor of the spike counts of the cells in the primary visual	
409	cortex. Means were taken across cells first, then across trials. There was a	
410	significant decrease in the Fano factors immediately after stimulus onset. (B)	
411	The mean Fano factor of the spike counts of the cells in the motor cortex. No	
412	significant change in measurements at any point. . . . .	94

# 413 List of Tables

414	2.1	Fixed parameters A table of the parameters fixed before optimising the model. The values of these parameters could be changed to model different fluorescent calcium indicators. . . . .	17
415	4.1	Details of the different bin width and analysis window sizes used when binning spike times, and analysing those data. . . . .	79
416	4.2	Relative dispersion of the COMb distribution, and association between Bernoulli variables as represented by the value of the $\nu$ parameter. . . . .	84
417	4.3	Proportion of samples for which each distribution was the best fit, grouped by bin width. The COMb distribution is the best fit most of the time. . . . .	92
418			
419			
420			
421			
422			



# List of Abbreviations

<b>COMb</b>	Conway-Maxwell-binomial (distribution)
<b>OASIS</b>	Online active set method to infer spikes
<b>SNR</b>	Signal to noise ratio
<b>NMI</b>	Normalised mutual information
<b>AMI</b>	Adjusted mutual information
<b>VI</b>	Variation of information



# List of Symbols

$[Ca^{2+}]$	Free calcium concentration	mol
$[BCa]$	Fluorescent indicator bound calcium	mol
$[ECa]$	Endogenous mobile buffer bound calcium	mol
$[ImCa]$	Immobile mobile buffer bound calcium	mol
$[BCa^*]$	excited fluorescent indicator bound calcium	mol
$k_{X_f}$	binding (affinity) rate	$mol^{-1} s^{-1}$
$k_{X_b}$	unbinding (dissociation) rate	$s^{-1}$



425 **Chapter 1**

426 **Introduction**

427 **1.1 Overview**

428 Since Hodgkin and Huxley's squid experiments featuring a single axon (Hodgkin and Hux-  
429 ley, 1939), to more recent research with spike sorted data from  $\sim 24000$  neurons from 34  
430 brain regions from 21 mice (Allen et al., 2019), the number of neurons contributing to elec-  
431 trophysiological datasets has been growing. The number of simultaneously recorded neurons  
432 has doubled approximately every seven years since the use of multi-electrode recording in  
433 neuroscience began (Stevenson and Kording, 2011). Recording methods using two-photon  
434 calcium imaging have also been used to extract data from populations containing over 10000  
435 neurons (Peron et al., 2015). This dramatic growth in the number of neurons available for  
436 analysis requires a dramatic change in analysis methods.

437 There are multiple methods for reading activity from neuronal ensembles: electrophysiolog-  
438 ical, calcium imaging, and voltage imaging. Electrophysiology involves inserting electrodes  
439 into the brain of an animal. The electrodes read extra-cellular membrane potential, and using  
440 these readings we observe activity in the ensemble. Calcium imaging and voltage imaging  
441 use indicator dyes or fluorescent proteins that emit fluorescence traces that indicate either  
442 the concentration of calcium in a neuron's cytoplasm, or the neuron's membrane potential.  
443 In this project, we have attempted to address some of the difficulties in collecting data from  
444 these large ensembles using fluorescent calcium indicators, and some of the difficulties in  
445 analysing the collected data.

446 The rest of this introductory chapter will give some background about methods of record-  
447 ing from the brain, and some background for the rest of the document. Chapter two describes  
448 a biophysical model for the fluorescence trace induced by a given spike train in a cell con-  
449 taining a fluorescent calcium indicator. Our third chapter describes our investigations into

450 the correlated activity across different regions of a mouse behaving spontaneously. We ap-  
451 plied a novel community detection method (Humphries et al., 2019) from network science  
452 to correlation based networks of neurons, and observed differences in the structure of these  
453 correlations at different timescales. In our fourth chapter, we detail a new statistical model  
454 for the number of neurons spiking in a neuronal ensemble at any given moment. With this  
455 model, we attempted to capture correlated activity in a new way. The fifth chapter is a brief  
456 description of the work that yielded negative results or was abandoned. The final chapter is a  
457 discussion of our work and results from the previous chapters and their implications.

## 458 1.2 Modelling the fluorescence of calcium indicators

459 To focus on calcium imaging for a start, a neuron that contains a fluorescent calcium indicator  
460 in its cytoplasm will fluoresce when bombarded with photons. The amount that the cell  
461 will fluoresce is dependent on the concentration of fluorescent indicator within the cell, and  
462 the concentration of calcium within the cell. When a neuron fires an action potential, the  
463 influx of free calcium ions causes an increase in fluorescence when those ions bond with the  
464 fluorescent indicator and those bounded molecules are bombarded with photons. After the  
465 action potential, as calcium is extruded from the cell the fluorescence returns to a baseline  
466 level. This is the basic mechanism of fluorescent calcium indicator based imaging.

467 This method has some advantages over electrophysiology as measure of neuronal ensem-  
468 ble activity. Many of the problems with electrophysiology are within the processes used to  
469 isolate spikes in the extracellular voltage readings, and assign these spikes to individual cells.  
470 These processes are collectively called ‘spike sorting’. A comparison of many different spike  
471 sorting algorithms found that these algorithms only agreed on a fraction of cases (Buccino  
472 et al., 2019). Furthermore, because electrodes measure extracellular voltage, neurons that do  
473 not spike will not be detected. Isolating individual neurons is easier and more reliable when  
474 using calcium imaging data, because cells will emit a baseline level of fluorescence when not  
475 firing action potentials. Another advantage is that calcium imaging sites can be re-used for  
476 weeks for longitudinal studies (Chen et al., 2013). One of the methods of delivering the flu-  
477 orescent indicator is by adeno-associated viruses, consequently there can be problems with  
478 indicator gradients around the infection site, and expression levels will change in individual  
479 cells over weeks (Tian et al., 2009; Chen et al., 2013). This delivery method can also cause  
480 cell pathology, and nuclear filling (Zariwala et al., 2012), but these problems can be solved by  
481 using lines of transgenic mice (Dana et al., 2014). The fluorescence signal itself can serve a a

482 good indicator of cell activity, but similarly to electrophysiology, the aim of calcium imaging  
483 is often spike detection.

484 If the imaging data is collected at a high enough frequency, and the signal-to-noise ratio  
485 of the fluorescence trace is high enough, it should be possible to infer the spike times to some  
486 level of accuracy. For example, the calmodulin based indicator GCaMP6s has a sufficiently  
487 high signal-to-noise ratio that isolated action potentials can be detected and inferred (Chen  
488 et al., 2013). Many spike inference algorithms exist (Vogelstein et al., 2010; Pnevmatikakis  
489 et al., 2016; Friedrich and Paninski, 2016; Pnevmatikakis et al., 2013; Pnevmatikakis et al.,  
490 2014; Deneux et al., 2016; Greenberg et al., 2018), and some of these can perform both cell  
491 isolation and spike detection simultaneously (Vogelstein et al., 2010; Pnevmatikakis et al.,  
492 2016; Pnevmatikakis et al., 2014; Deneux et al., 2016). But the relationship between spik-  
493 ing and fluorescence change is not fully understood. For example, the fluorescent indicator  
494 will act like an additional calcium buffer within the cell cytoplasm and will compete with  
495 the other endogenous buffers to bind with free calcium ions. Therefore, the concentration  
496 of those endogenous buffers, and the binding dynamics of those buffers will have an effect  
497 on the change in fluorescence in response to an action potential. Furthermore, the binding  
498 dynamics of the fluorescent indicator itself will have an effect on the change in fluorescence.  
499 For example, the GCaMP series of fluorescence indicators are based on the calcium buffer  
500 protein calmodulin. This protein has four binding sites, whose affinities interact non-linearly.  
501 But most of the spike inference algorithms model the fluorescence as a linear function of  
502 a calcium trace, and they model this calcium trace as a first or second order autoregression  
503 with a pulse input to represent action potentials. Deneux et al. (2016) developed two dif-  
504 ferent calcium fluorescence models behind their spike inference algorithm (MLspike) with a  
505 more biological inspiration. For their simpler model, they take a physiological approach and  
506 account for baseline calcium indicator dynamics. They end up with a system of first order  
507 differential equations defining the dynamics of calcium concentration, baseline fluorescence,  
508 and fluorescence. For their more complicated model specifically for genetically encoded cal-  
509 cium indicators, they also took into account indicator binding and unbinding rates, which  
510 added another equation to their system of equations. The algorithms that use the autore-  
511 gression model and the MLspike algorithm are outperformed by the most recently published  
512 spike inference algorithm (Greenberg et al., 2018). This algorithm takes into account the  
513 binding dynamics of both the endogenous buffers and fluorescent calcium indicator, and the  
514 concentrations of free calcium, indicator, and endogenous buffer within the cell cytoplasm.  
515 The performance of this algorithm shows that there is value in more biologically inspired

516 models of fluorescent calcium indicators.

517 In light of the growing popularity of two-photon calcium imaging, and the lack of biolog-  
518 ically inspired spike inference algorithms (Greenberg et al. developed their spike inference  
519 algorithm in parallel to our work), we decided to develop a biologically inspired model for  
520 fluorescent calcium indicator fluorescence. The idea being that our model would take a spike  
521 train, or simply spike times, provided by the user, and return the fluorescence trace that would  
522 be induced by this spike train or spike times. The model contains parameters for concentra-  
523 tions of indicator and endogenous buffers, as well as affinity and unbinding rates for these  
524 buffers. There are also parameters for the baseline concentration of free calcium in the cell  
525 cytoplasm, and the cell radius (as a means for calculating the cell volume). With this model,  
526 we hoped that experimentalists would be able to test out different calcium indicators on the  
527 types of spike trains that they expect to encounter. This way they could decide ahead of time  
528 which indicator suited their situation best. Since the output of our model is a fluorescence  
529 trace, the spike inference models mentioned above can be applied to the modelled fluores-  
530 cence. This means that the model could also be used to benchmark the performance of these  
531 spike inference algorithms, and to investigate the impact of variations in the model on spike  
532 inference accuracy.

### 533 1.3 Functional networks

534 We have outlined some of the advantages that calcium imaging has over electrophysiology.  
535 But electrophysiology is more useful in some situations. One particular drawback for two-  
536 photon calcium imaging is that usually it can only be used for imaging near to the surface  
537 of the brain. This problem can be solved by removing the tissue around the area to be im-  
538 aged, and custom building a two-photon microscope Dombeck et al., 2010. Imaging with  
539 three (or presumably more) photons may solve this problem in the future (Ouzounov et al.,  
540 2017). A better option for reading activity from neurons beyond the surface of the brain is to  
541 use Neuropixels probes (Jun et al., 2017). These probes can be used to read from thousands  
542 of neurons simultaneously in many different areas of the brain (Allen et al., 2019; Stringer  
543 et al., 2019; Steinmetz, Carandini, and Harris, 2019; Steinmetz et al., 2019). This brings us  
544 to another problem for which we require new innovations in our analysis methods. Specif-  
545 ically, analysing correlated behaviour in neural ensembles consisting of neurons from many  
546 different brain regions.

547 Until the invention of new technologies such as the Neuropixels probes, most elec-  
548 trophysiology datasets read from neurons in only one or two regions. Therefore most of  
549 the research on interactions between neurons in different regions is limited to two regions  
550 (Wierzynski et al., 2009; Patterson et al., 2014; Girard, Hupé, and Bullier, 2001). In chapters  
551 3 and 4 we used datasets with neurons from 9 and 5 different brain regions respectively. In  
552 their review of the interaction between growing the number of neurons in datasets and the  
553 analysis methods applied to those dataset, Stevenson and Kording (2011) assert that an im-  
554 portant objective of computational neuroscience is to find order in these kinds multi-neuron  
555 of datasets. This was our main aim for the research described in chapter 3.

556 In light of recent findings based on correlated behaviour showing that spontaneous be-  
557 haviours explain activity in many different parts of the brain that would otherwise be regarded  
558 as noise (Stringer et al., 2019), that satiety is represented brain wide (Allen et al., 2019), and  
559 that exploratory and non-exploratory states are represented in the amygdala (Gründemann  
560 et al., 2019), it was clear that state representation or motor control had an influence on cor-  
561 related behaviour in areas of the brain not usually associated with these tasks. Also, given  
562 differences in timescales of fluctuations in different brain regions (Murray et al., 2014), and  
563 different timescales for event representation in different brain regions (Baldassano et al.,  
564 2017), we decided to investigate brain wide correlated behaviour at timescales ranging from  
565 5ms up to 3s.

566 We started off measuring the correlations in spike counts between individual neurons in  
567 our ensemble. These measurements induced a weighted undirected graph where each node  
568 represented a neuron, and the weight of each edge was the strength of the correlation be-  
569 tween the neurons represented by the nodes at either end of that edge. In order to put the  
570 neurons into groups with correlated behaviour, we applied a novel community detection al-  
571 gorithm (Humphries et al., 2019) to this graph. We repeated this analysis for timescales  
572 from milliseconds to seconds. Bear in mind that our correlation based graph was completely  
573 agnostic of the anatomical regions in which our cells resided. We then compared our corre-  
574 lated communities to their anatomy at each timescale. In this way, we used a novel method,  
575 never applied neuronal data before, to analyse the makeup of correlated communities across  
576 different regions at different timescales.

## 577 1.4 A new statistical model for capturing correlated behaviour

578 Many important findings have been made by measuring the correlations between binned  
 579 spike counts, but there are some problems with this method of analysis. Firstly, the width  
 580 of the bins used to bin spike times into spike counts has an effect on the magnitude of the  
 581 correlations measured. Using a short bin width can cause your measurements to be artificially  
 582 small (Cohen and Kohn, 2011). This may not be an issue if one is considering relative size of  
 583 correlations when using the same bin width, but it is still not ideal. Secondly, while pairwise  
 584 correlations can capture most of the information in a small network (up to 40 cells) of highly  
 585 correlated cells (Schneidman et al., 2006), a model based on pairwise correlations alone will  
 586 fail to capture the activity of larger ( $\sim 100$  cells) networks, higher order correlated activity  
 587 is required (Ganmor, Segev, and Schneidman, 2011). One problem with these higher order  
 588 correlations is that they may be defined in different ways (Staude, Grün, and Rotter, 2010).  
 589 Furthermore if we want to include them in a model this usually involves greatly increasing the  
 590 number of parameters to fit, which increases the dimension of the parameter space leading  
 591 to the ‘curse of dimensionality’. Some models attempt to sidestep these problems while  
 592 still capturing higher-order correlations. These models attempt to capture the relationship  
 593 between each individual neuron in the ensemble, and the ensemble as a whole. Okun et al  
 594 (2015) called the strength of this relationship the ‘population coupling’, and demonstrated  
 595 that this quantity can predict an individual neuron’s response to optogenetic stimulation of  
 596 the whole ensemble. They also showed that this quantity was an indicator of the neuron’s  
 597 synaptic connectivity (Okun et al., 2015). With the ‘population tracking model’, O’Donnell  
 598 et al. (2016) linked the probability of firing an action potential for each individual neuron  
 599 with the distribution of the number of active neurons. This allowed model fitting for a large  
 600 number of neurons, as well as calculation of full pattern probabilities, and population entropy  
 601 (O’Donnell et al., 2017).

602 In this work, we also aimed to capture correlated behaviour between the neurons in a  
 603 neuronal ensemble without measuring correlations directly. Correlation coefficients capture  
 604 the linear component of the relationship between two random variables, but will not mea-  
 605 sure any relationship beyond linearity. Also, measuring correlation coefficients using short  
 606 timebins can be difficult for neuronal data (Cohen and Kohn, 2011). We decided to abandon  
 607 correlation, and we aimed to quantify a more general concept of association by modelling  
 608 the number of active neurons in the ensemble using a Conway-Maxwell-binomial (COMb)  
 609 distribution (Kadane, 2016).

610        The COMb distribution is a probability distribution over the number of successes in a  
611        sequence of Bernoulli trials, where these trials can be associated in some way. The COMb  
612        distribution is an extension of the standard binomial distribution, with an additional parameter  
613        to model association between the Bernoulli variables. Using this additional parameter the  
614        distribution can capture positive association, where the Bernoulli variables tend to take the  
615        same value, negative association, where the Bernoulli variables tend to take opposite values,  
616        or no association i.e. the standard binomial distribution.

617        We fit a COMb distribution to spike sorted electrophysiological data taken from five  
618        different regions in the brain of an awake mouse exposed to visual stimuli (Steinmetz et al.,  
619        2019). We examined whether or not a model based on the COMb distribution was able to  
620        capture changes in the number of active neurons in these neuronal ensembles in response to  
621        the stimuli. We also investigated the relationship between the changes as captured by the  
622        COMb model and the change in neural variability as measured by Churchland et al. in their  
623        famous paper (Churchland et al., 2010).

624        Our overall aim was to investigate some of the challenges in analysing large ensembles  
625        of neurons present today. That included collecting the data to analyse (via calcium imaging),  
626        and subsequently analysing these data. We felt that this was a worthwhile project because  
627        the size of datasets, in terms of numbers of neurons and data collected, is growing rapidly.  
628        Consequently these challenges will only become greater unless they are addressed. This is  
629        our attempt at addressing them.



630 **Chapter 2**

631 **Sensitivity of the**  
632 **spikes-to-fluorescence transform to**  
633 **calcium indicator and neuron**  
634 **properties**

635 *Abstract*

636 Fluorescent calcium indicators such as GCaMP are widely used to monitor neuronal activity.  
637 However the relationship between the fluorescence signal and the underlying action potential  
638 firing is poorly understood. This lack of knowledge makes it difficult for experimenters  
639 to decide between different indicator variants for a given application. We addressed this  
640 problem by studying a basic biophysical model of calcium dynamics in neuronal soma. We  
641 fit the model parameters to publicly available data where GCaMP6s fluorescence and whole-  
642 cell electrophysiological recordings were made simultaneously in the same single neurons.  
643 We systematically varied the model's parameters to characterise the sensitivity of spike train  
644 inference algorithms to the calcium indicator's main biophysical properties: binding rate,  
645 dissociation rate, and molecular concentration. This model should have two potential uses:  
646 experimental researchers may use it to help them select the optimal indicator for their desired  
647 experiment; and computational researchers may use it to generate simulated data to aid design  
648 of spike inference algorithms.

649 **2.1 Introduction**

650 Although fluorescent calcium indicators such as GCaMP are widely used to monitor neuronal  
651 activity, the relationship between the fluorescence signal and the underlying action potential  
652 firing is imperfect. The fluorescence signal has a low signal-to-noise ratio, and most indica-  
653 tors' kinetics are slow relative to the millisecond-timescale dynamics of the membrane volt-  
654 age (example in figure 2.1A). This makes spike inference difficult. Furthermore, the effects  
655 of the indicator and cell properties on the fluorescence signal are unknown. For example,  
656 genetically encoded indicators can accumulate within neurons over weeks and months (Chen  
657 et al., 2013). Studies using calcium-sensitive fluorescent dyes have shown that indicator con-  
658 centration has substantial effects on the spike-to-fluorescence relationship (Maravall et al.,  
659 2000). Therefore spike rates inferred from GCaMP fluorescence signals may give mislead-  
660 ing results if comparing across imaging sessions. More generally, the poor understanding of  
661 the spike-to-fluorescence transform means experimenters may not know whether to trust the  
662 outputs of spike train inference methods in any given application.

663 Spike trains are usually inferred from the time series of intensity values of one pixel of the  
664 fluorescence image, where the pixel is located at the cell's soma. The problems of identifying  
665 these pixels, and inferring spikes from their time series can solved separately or together.  
666 When attempting to infer spikes, the fluorescence trace is modelled as a linear combination of  
667 calcium concentration dynamics, a baseline calcium concentration, and some Gaussian noise.  
668 The calcium concentration dynamics are modelled as an autoregressive process of degree 1  
669 or 2 with a pulse input corresponding to the spike train, or the number of spikes fired in a  
670 time step. The model includes no dynamics for the fluorescent indicator itself. Furthermore,  
671 in order to make this model into an easily solvable linear programming problem the number  
672 of spikes fired in a timestep is not restricted to non-negative integers but to arbitrary non-  
673 negative values (Vogelstein et al., 2010; Pnevmatikakis et al., 2016; Friedrich and Paninski,  
674 2016; Pnevmatikakis et al., 2013; Pnevmatikakis et al., 2014). More biologically inspired  
675 spike inference models do exist (Deneux et al., 2016), but their fundamentals are very similar.  
676 In this work, we investigated the effect of changing dynamics and buffer concentrations on  
677 the accuracy of the inference algorithms based on these models.

678 The aim of this project was to model the fluorescence traces produced by a fluorescent  
679 calcium indicator in a neuron soma resulting from a specific spike train, given calcium indi-  
680 cator parameters such as binding rate, dissociation rate, and molecular concentration. Such

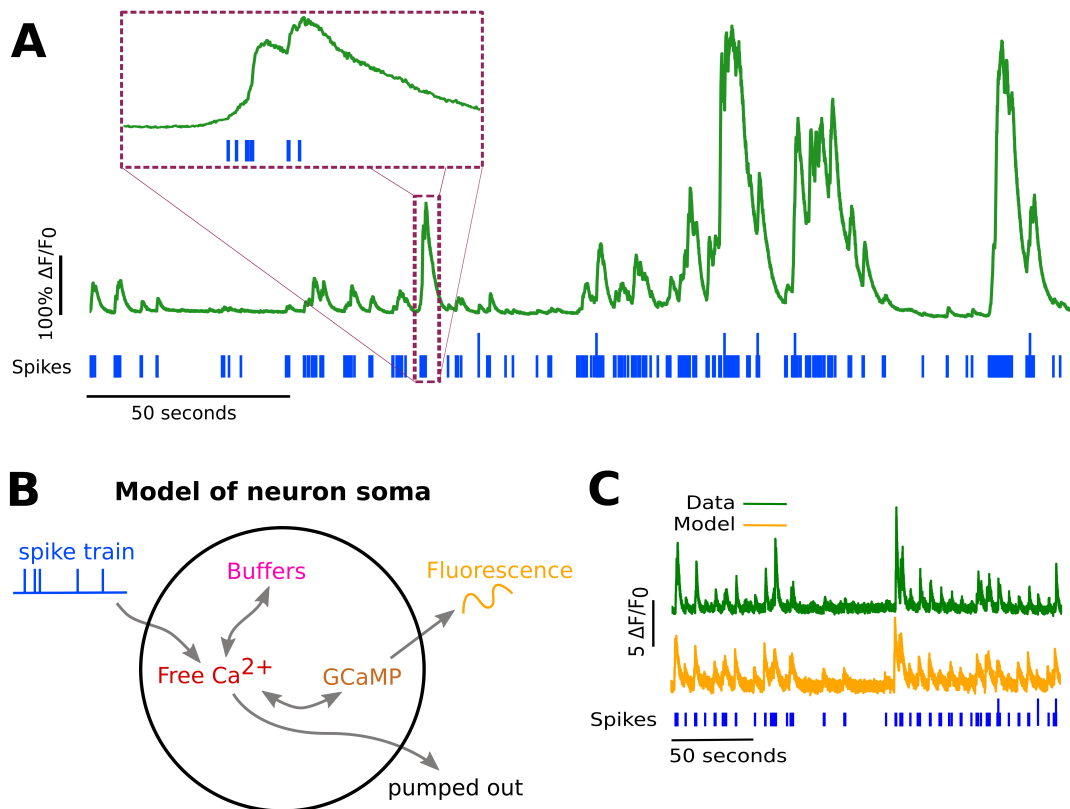


FIGURE 2.1:

- A: Example spike train (blue) and the corresponding GCaMP6s fluorescence trace (green), data replotted from (Berens et al., 2018). Inset shows zoomed section of traces to highlight slow decay of GCaMP6s fluorescence relative to spike time intervals.
- B: Schematic diagram of the neuron calcium and GCaMP computational model.
- C: Good visual match of data fluorescence trace (green) and model simulated fluorescence (orange) in response to an identical spike train (blue).

681 a model would allow benchmarking of various spike inference algorithms, and enable under-  
682 standing of how indicator characteristics affect the quality of spike train inference.

683 The model we developed consisted of free calcium, fluorescent indicator molecules, and  
684 mobile and immobile endogenous calcium buffers. The indicator molecules which were  
685 bound to a calcium molecule could be either excited, i.e. able to release a photon, or relaxed.  
686 In order to reproduce the noise inherent in the data collection, we modelled the release of  
687 photons from the excited indicator bound calcium as a stochastic process.

688 The fluorescence traces produced by the simulation were calibrated to reproduce the  
689 signal-to-noise ratio observed in experimental data. Previously published spike inference  
690 algorithms were then used to infer spike trains from the experimental fluorescence traces and  
691 the modelled fluorescence traces. The parameters of the model were then varied in order to  
692 determine the effect on the system dynamics and the effects on spike inference.

## 693 2.2 Methods

### 694 2.2.1 Calcium dynamics model

695 We wrote a biophysical model of the calcium dynamics within a cell soma. When a neuron  
696 fires an action potential, voltage-dependent calcium ion-channels open up that allow a current  
697 of calcium ions ( $\text{Ca}^{2+}$ ) to flow into the neuron (Koch, 1999). The increase in the free calcium  
698 ion concentration inside of the cell, along with changes in the concentration of potassium  
699 and sodium, causes the change in cell membrane potential, which must be repolarised. The  
700 depolarising process consists of free calcium ions leaving the cell through open ion channels,  
701 or binding to molecules within the cell called buffers, or calcium storage by organelles such  
702 as the endoplasmic reticulum. A diagram illustrating the cell, its channels, and its buffers  
703 can be seen in figure 2.1A. There are several different types of calcium buffer, each with  
704 different dynamics and different concentrations within different types of excitable cell. The  
705 fluorescent calcium indicator is another calcium buffer, with the useful property that when it  
706 is bound to a calcium ion, the bound molecule may become excited by a photon and release  
707 a photon in return. This is what creates the fluorescence. After the action potential has taken  
708 place, the free calcium concentration within the cell will return to a baseline level (Maravall  
709 et al., 2000).

710 We modelled the the dynamics of five molecular concentrations,

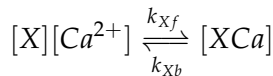
- 711 • Free calcium ion concentration,  $[\text{Ca}^{2+}]$

## 2.2. Methods

---

- 712     • Fluorescent indicator bound calcium,  $[BCa]$   
 713     • Endogenous mobile buffer bound calcium,  $[ECa]$   
 714     • Endogenous immobile buffer bound calcium,  $[ImCa]$   
 715     • Excited buffered calcium,  $[BCa^*]$

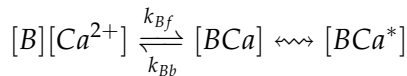
The term ‘buffering’ refers to free calcium ions coming into contact with buffer molecules followed by the binding of those molecules. Diagrammatically:



716 where  $[X]$  represents any buffer molecule, and  $k_{X_f}$  and  $k_{X_b}$  represent the binding (association)  
 717 and unbinding (dissociation) rates in units of per molar concentration per second ( $M^{-1}$   
 718  $s^{-1}$ ) and per second ( $s^{-1}$ ) respectively. The speed of this chemical reaction is determined by  
 719 the binding and unbinding rates.

720 There are a number different endogenous buffers in any neuron. Which buffers are  
 721 present, and the buffers’ concentrations vary from cell to cell. In order to capture the ef-  
 722 fects of mobile and immobile endogenous buffers without introducing several parameters,  
 723 they were modelled as two buffers. One representing mobile buffers and the other represent-  
 724 ing immobile buffers. Each with their own binding and unbinding rates. Note that since the  
 725 model has no spatial component, the mobile and immobile buffers only differ in their binding  
 726 and unbinding rates.

The fluorescent calcium indicator behaves similarly to the other calcium buffers. The calcium is buffered by the indicator in the same way. But an indicator bound calcium molecule can become excited by absorbing the energy from a photon. An excited indicator bound calcium molecule can then release a photon to go back to its ‘relaxed’ state.



727 The released photons are captured by a photon collector. This gives us the fluorescence trace.  
 728 The system of equations we used to model all of these interactions is as follows:

$$\begin{aligned} \frac{d[Ca^{2+}]}{dt} = & k_{Bb}[BCa] + k_{Eb}[ECa] + k_{Imb}[ImCa] \\ & - k_{Bf}[B][Ca^{2+}] - k_{Ef}[E][Ca^{2+}] - k_{Imf}[Im][Ca^{2+}] \\ & + \beta([Ca_0^{2+}] - [Ca^{2+}]) \end{aligned} \quad (2.1)$$

$$\frac{d[BCa]}{dt} = k_{Bf}[B][Ca^{2+}] - k_{Bb}[BCa] + r[BCa^*] - \eta[BCa] \quad (2.2)$$

$$\frac{d[ECa]}{dt} = k_{Ef}[E][Ca^{2+}] - k_{Eb}[ECa] \quad (2.3)$$

$$\frac{d[ImCa]}{dt} = k_{Imf}[Im][Ca^{2+}] - k_{Imb}[ImCa] \quad (2.4)$$

$$\frac{d[BCa^*]}{dt} = \eta[BCa] - r[BCa^*] \quad (2.5)$$

where  $[Ca_0^{2+}]$  is the baseline calcium concentration within the cell soma,  $\beta$  is a rate defining how quickly free calcium enters or leaves the cell in the absence of an action potential,  $\eta$  is the excitation rate for indicator bound calcium,  $r$  is the photon release rate for the excited indicator bound calcium, and  $f$  and  $b$  are used to indicate the forward and backward rates for chemical reactions respectively. The excitation rate defines the proportion of indicator bound calcium that becomes excited at each time step. The photon release rate defines the proportion of excited indicator bound calcium that releases a photon and returns to its relaxed state at each time step. An action potential is modelled as a discontinuous increase in the free calcium concentration to an appropriate value (Maravall et al., 2000).

Note that each of the three pairs of binding and unbinding terms in the first equation has a corresponding pair in one of the subsequent three equations. Binding removes a free calcium molecule and adds a bound calcium molecule, and unbinding does the opposite.

When using this model to simulate a fluorescence trace, the system of equations above are first solved over a period of 25s without action potentials. This lets each of the five tracked chemical concentrations reach their steady state. Then we use the given spike train and the parameters to model the fluorescence trace.

#### Photon release & capture

We used a simple model for the photon release. The number of photons released at each time step was controlled by the number of excited indicator bound calcium molecules in the cell and a parameter called the ‘release rate’. The release rate is an optimised free parameter of the model.

As for the photon capture, in two-photon excitation microscopy the photons scattered by the fluorescent indicator get scattered in all directions. Therefore the number of photons detected is stochastic. This made the process for capturing photons the natural source of noise in the system. The number of photons captured, and therefore the intensity of the fluorescence, is modelled using a binomial distribution. The number of photons released was

## 2.2. Methods

---

755 used as the number of trials. The probability of success, or ‘capture rate’ was a free parameter  
756 of the model that we optimised.

757 **2.2.2 Parameter optimisation**

758 The free parameters of the model are as follows:

759 **Calcium rate,  $\beta$**  Controls how quickly the concentration of free calcium will be driven to  
760 the baseline concentration.

761 **Capture rate,  $p$**  The average proportion of photons captured by the photon detector.

762 **Excitation rate,  $\eta$**  The number of indicator bound calcium molecules that become excited  
763 by photon bombardment at each time step.

764 **Release rate,  $r$**  The number of excited indicator bound calcium molecules that release a  
765 photon at each time step.

766 To optimise the free parameters given a fluorescence trace, we applied the following proce-  
767 dure:

- 768 1. The frequency power spectrum of the trace was measured.
- 769 2. The power spectrum was smoothed using a boxcar smoother (aka. sliding average, box  
770 smoother).
- 771 3. The log of the smoothed power spectrum was measured.
- 772 4. Use the model to create a modelled fluorescence trace.
- 773 5. Apply steps 1, 2, and 3 to the modelled fluorescence trace.
- 774 6. Calculate the root mean squared difference between the log power of the actual fluo-  
775 rescence trace, and the log power of the modelled fluorescence trace.
- 776 7. Calculate the root mean squared difference between the actual fluorescence trace and  
777 the modelled fluorescence trace.
- 778 8. Use an optimisation algorithm to reapply this process, attempting to minimize the sum  
779 of the two root mean squared differences at each iteration.

780 Using the root mean squared difference of the log power spectra as part of the objective  
781 function forces the model to match the noise frequency of the actual fluorescence. Using

782 the root mean squared difference of the traces themselves forces the model to match the  
783 amplitude of the fluorescence trace more accurately.

784 In order to minimise the objective function, a suite of meta-heuristic optimisation (aka.  
785 black-box optimisation) algorithms were implemented on each of the traces in the dataset.  
786 These methods were chosen because they don't require a gradient for the objective function  
787 (gradient-free) and they are particularly useful for minimising stochastic objective functions  
788 like the one we used here. The free parameters were optimised for each individual fluores-  
789 cence trace. The most successful method for each trace was recorded. The method that was  
790 most often successful was probabilistic descent, and the second most successful method was  
791 generating set search. Both of these methods are examples of pattern search. These two  
792 methods were the best optimisers on about 75% of the traces in the dataset. The other meth-  
793 ods were differential evolution (with and without radius limited sampling, adaptive and not  
794 adaptive), natural evolution strategy, and random search for comparison.

795 Although this optimisation procedure minimises the value of the optimisation function,  
796 the value never reaches zero for a number of reasons. Firstly, the fluorescence traces carry  
797 low frequency fluctuations that cannot be captured by the model. Secondly, the model as-  
798 sumes that the process of calcium binding to the fluorescent indicator is linear in time (see  
799 equation 1), but there are more complicated dynamics involved here. Fluorescent calcium  
800 indicators, the GCaMP series for example, are often built upon the calcium binding protein  
801 called 'calmodulin'. This protein has four calcium binding sites. These sites are locally split  
802 into two pairs. Each pair has a different affinity for calcium, and the affinity of the binding  
803 sites is affected by the occupancy of the other binding sites (Kilhoffer et al., 1992). So the  
804 calcium to calcium indicator binding process is non-linear, but the model does not take this  
805 into account.

## 806 Fixed parameters

807 As well as the optimised parameters mentioned in section 2.2.2, the model also has thirteen  
808 fixed parameters. Please see table 2.1 for details of these parameters and their values. In  
809 an application of the model, these parameters can be changed in order to model any given  
810 fluorescent calcium indicator, or even prospective indicators that only exist in theory.

## 2.2. Methods

---

Parameter	Description	Value	Source
baseline	The baseline concentration of free calcium within the cell soma	$4.5 \times 10^{-8} M$	(Maravall et al., 2000)
cell radius	The radius of the soma (assumed to be spherical)	$10^{-5} M$	(Fiala and Harris, 1999)
endogenous	The concentration of endogenous mobile buffer within the cell soma	$10^{-4} M$	(Faas et al., 2011)
frequency	The frequency at which the spike trains are sampled.	100Hz	
immobile	The concentration of endogenous immobile buffer within the cell soma	$7.87 \times 10^{-5} M$	(Bartol et al., 2015)
indicator	The concentration of fluorescent indicator within the cell soma	$10^{-4} M$	(Maravall et al., 2000)
$k_{Bb}$	The unbinding rate of the fluorescent calcium indicator	$160 s^{-1}$	(Bartol et al., 2015)
$k_{Bf}$	The binding rate of the fluorescent calcium indicator	$7.77 \times 10^8 s^{-1} M^{-1}$	(Bartol et al., 2015)
$k_{Eb}$	The unbinding rate of the endogenous mobile buffer	$10^4 s^{-1}$	(Bartol et al., 2015)
$k_{ef}$	The binding rate of the endogenous mobile buffer	$10^8 s^{-1} M^{-1}$	(Bartol et al., 2015)
$k_{Imb}$	The unbinding rate of the endogenous immobile buffer	$524 s^{-1}$	(Bartol et al., 2015)
$k_{Imf}$	The binding rate of the endogenous immobile buffer	$2.47 \times 10^8 s^{-1} M^{-1}$	(Bartol et al., 2015)
peak	The increase in free calcium concentration within the cell induced by an action potential	$2.9 \times 10^{-7} M$	(Maravall et al., 2000)

TABLE 2.1: **Fixed parameters** A table of the parameters fixed before optimising the model. The values of these parameters could be changed to model different fluorescent calcium indicators.

811 **2.2.3 Julia**

812 The programming language used to write and execute the model was ‘Julia’. Julia is a dy-  
813 namic programming language designed for technical computing. Julia was designed specif-  
814 ically to provide a convenient high-level dynamic language similar to MATLAB, or Python,  
815 with improved performance. Julia’s type system and Julia’s direct interfaces with C and  
816 Fortran allow this aim to be achieved (Bezanson et al., 2012). The Julia version of the  
817 ‘Sundials’ package for ODE solving was used to solve the system of equations above. The  
818 BlackBoxOptim.jl package for Julia was used to perform the optimisation.

819 **2.2.4 Spike inference**

820 We used spike inference algorithms to compare the quality of spike inference using the mod-  
821 eled traces to the quality of spike inference using the observed traces. We also used the  
822 spike inference algorithms to assess the effect of parameter perturbation on the spike infer-  
823 ence. Three algorithms were used:

824 **Constrained non-negative matrix deconvolution algorithm (aka CNMD algorithm)** The  
825 underlying model models the fluorescence as a linear function of a calcium trace with  
826 additional noise. This calcium trace is a first order autoregression with a pulse input to  
827 represent action potentials. This algorithm uses a constrained version of non-negative  
828 Weiner deconvolution to infer a calcium signal and a ‘spiking activity signal’ from the  
829 fluorescence trace (Vogelstein et al., 2010; Pnevmatikakis et al., 2016). The spiking ac-  
830 tivity signal is a non-negative vector of real numbers reflecting the cell’s activity rather  
831 than an actual spike train. We inferred a spike train by choosing an optimised thresh-  
832 old for the spiking activity signal. Whenever the spiking activity signal exceeded that  
833 threshold, an action potential was inferred. The threshold was optimised by minimis-  
834 ing the difference between the number of spikes observed and the number of spikes  
835 predicted.

836 **MLSpike algorithm** Deneux et al. (2016) developed two different calcium fluorescence  
837 models behind their spike inference algorithm (MLspike) with a more biological in-  
838 spiration. For their simpler model, they take a physiological approach and account for  
839 baseline calcium indicator dynamics. They end up with a system of first order differen-  
840 tial equations defining the dynamics of calcium concentration, baseline fluorescence,  
841 and fluorescence. For their more complicated model specifically for genetically en-  
842 coded calcium indicators, they also took into account indicator binding and unbinding

## 2.2. Methods

---

843 rates, which added another equation to their system of equations. This algorithm uses a  
844 generalised version of the Viterbi algorithm to return the spike train that maximises the  
845 likelihood of producing the given fluorescence trace. The Viterbi algorithm is an algo-  
846 rithm for estimating the most likely sequence of hidden states resulting in a sequence  
847 of observed states in a discrete-time finite-state Markov process (Forney, 1973). In this  
848 case, each hidden state is defined by the presence or absence of an action potential, and  
849 each observed state is the value of the fluorescence trace at each time step. (Deneux  
850 et al., 2016).

851 **Online Active Set method to Infer Spikes (OASIS)** This algorithm is once again based on  
852 an auto-regressive model of the fluorescence trace, but can be generalised to any or-  
853 der. Both the first and second order versions can be fit to a spike train in a reasonable  
854 time. The algorithm itself is a generalisation of the pool adjacent violators algorithm  
855 (PAVA) that is used in isotonic regression. The OASIS algorithm works through the  
856 fluorescence trace from beginning to end, this combined with the speed of the algo-  
857 rithm means that it could be used for real-time online spike inference (Friedrich and  
858 Paninski, 2016). Given a fluorescence trace, the algorithm will return the most likely  
859 spike train and an inferred denoised fluorescence signal.

860 In order to quantify the quality of spike inference for a given algorithm, we ran that algorithm  
861 on all of the fluorescence traces in dataset number eight of the spike finder datasets. Then we  
862 measured some binary classification measures on the results. These measures included

- 863     ● Accuracy
- 864     ● True positive rate (aka recall, sensitivity, hit rate)
- 865     ● True negative rate (aka specificity)
- 866     ● Precision
- 867     ● Negative predicted value
- 868     ● False negative rate (aka miss rate)
- 869     ● False positive rate (aka fall-out)
- 870     ● False discovery rate
- 871     ● False omission rate

872 In making these measurements, we allowed a tolerance of two subsequent time bins for spike  
873 prediction. For example, the spike train data is a vector of 0s and 1s, with one element for  
874 each time bin. A ‘0’ denotes inactivity, a ‘1’ denotes the presence of at least one action  
875 potential. The inferred spike trains produced by the spike inference algorithms take the same  
876 form. In our analysis, if a spike appeared in the inferred spike train up to two time frames  
877 after a spike in the observed spike train, that spike was considered correctly inferred i.e. a  
878 true positive. However, once a spike in the inferred spike train was matched to a spike from  
879 the observed spike train, the inferred spike could not be matched to another observed spike.  
880 To illustrate, if two spikes were inferred in the two time bins following an isolated observed  
881 spike, the first inferred spike was considered correctly inferred, but the second inferred spike  
882 was considered incorrectly inferred, i.e. a false positive.

883 The most useful measure was the true positive rate. This is because the spiking is sparse  
884 and this measurement is sensitive to the number of spikes observed and inferred, but is not  
885 affected by the true negative or false negative rates. After optimising the parameters for each  
886 fluorescence trace we measured the spike inference quality for the observed fluorescence  
887 traces, and compared this to the spike inference quality for the modelled traces.

888 When measuring the spike inference quality for higher frequency spike train (1 – 10Hz),  
889 we used the accuracy as our binary classification measure. At these frequencies the variance  
890 of the fluorescence trace was much higher than for sparser spiking regimes, therefore we  
891 wanted to take into account the number of false negatives inferred by the algorithm.

## 892 Comparing spike inference quality

893 In order to compare spike inference quality we had to use methods for comparing samples.  
894 When comparing the true positive rate distributions arising from two different datasets, or  
895 two different algorithms on the same dataset, we compared the distributions using a paired  
896 t-test.

### 897 2.2.5 Perturbation analysis

898 In order to measure the sensitivity of spike inference to changes in a given model parameter,  
899 we perturbed the parameter and compared the quality of spike inference with the perturbed  
900 parameters to the quality of spike inference with the experimental or optimised parameters.  
901 In order to maximise the possibility of observing a difference due to the perturbation, we  
902 perturbed the chosen parameter by a relatively large amount. For example, the experimen-  
903 tal value for the molar concentration of the fluorescent indicator within the cell was  $10^{-4}M$

## 2.3. Results

---

904 (Maravall et al., 2000). The perturbed values used for this parameter were  $10^{-2}M$ ,  $10^{-3}M$ ,  
905  $10^{-5}M$ , and  $10^{-6}M$ . The quality of the inference was compared by measuring the true posi-  
906 tive rate for each perturbed value and using a t-test to compare the distributions of the results.

### 907 2.2.6 Signal-to-noise ratio

908 To assess the effect of perturbation on the modelled traces, we measured and compared the  
909 signal to noise ratio (SNR) on each of the modelled traces. We calculated the SNR as the  
910 peak change in fluorescence divided by the standard deviation of the baseline fluctuation of  
911 the fluorescence trace (Tada et al., 2014). We measured these values by running the model  
912 on a spike train consisting a long period of inactivity followed by one action potential. We  
913 ran the model on this spike train one hundred times. We then measured the mean change  
914 in fluorescence and standard deviation of baseline activity across the one hundred modelled  
915 fluorescence traces, and calculated the SNR.

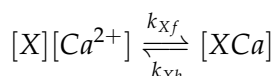
### 916 2.2.7 Data sources

917 All of the data used in this project was sourced from the ‘Spike Finder’ project ([spikefinder.codeneuro.org](http://spikefinder.codeneuro.org)).  
918 The data consisted of a collection of datasets with simultaneously measured fluorescence  
919 traces and action potentials (Berens et al., 2018).

## 920 2.3 Results

### 921 2.3.1 A biophysical computational model can generate accurate fluorescence 922 traces from spike trains

To study the relationship between action potential firing and calcium fluorescence, we built a computational model of calcium dynamics in a neuronal soma. The model consisted of four dynamic variables: the concentration of free calcium, two types of endogenous buffer, and the calcium-sensitive fluorescent indicator. Each of the buffers and the indicator could independently bind and unbind with calcium. These reactions were modelled as



923 where  $X$  is the buffer concentration and  $Ca^{2+}$  is the calcium concentration. Each species  
924 could therefore exist in two states: either bound with calcium or unbound. To model the

imaging process, we also added a third, excited state to the indicator. When in the calcium-bound state, the indicator could be converted to an excited state, corresponding to the absorption of a photon. The rate of this excitation process could be interpreted as the intensity of the light illuminating the sample. Once excited, the species decayed back to the unexcited state at a fixed rate, corresponding to the spontaneous emission of photons. The total emitted fluorescence signal was interpreted as proportional to this de-excitation flux. To represent experimental noise in the photon capture process, we drew a random number of captured photons at each time step from a binomial distribution, parameterised by a number  $p$  that corresponds to the mean fraction of released photons that are captured.

The model had 17 parameters in total describing the molecules' concentrations and reaction rates (Methods). We set 13 of these parameters to values from the literature. The remaining 4 parameter values we fit to publicly-available data (Berens et al., 2018), briefly explained as follows (see Methods for full details). Single neurons from acute rat cortical slices expressing GCaMP6f were imaged with two-photon microscopy while the membrane potentials of the somata of the same neurons were simultaneously recorded via whole-cell patch clamp electrophysiology. In this dataset, the electrical recordings give unambiguous information about neurons' spike times. To do the parameter fitting, we feed these spike trains as inputs to the computational model. After running, the model returns a simulated fluorescence trace. We aimed to find the model parameter values that give the best match between this simulated fluorescence trace and the real fluorescence time series recorded in the corresponding neuron. To do this we used a suite of optimisation procedures to jointly fit both the real neuron's fluorescence time series and power spectrum, which capture complementary information about the spikes-to-fluorescence mapping (Methods). We performed the fitting procedure independently for each of the 20 neurons in the spikefinder dataset (<http://spikefinder.org>). After fitting, the model produced realistic-looking fluorescence time series (Figure 2.1).

**2.3.2 Spike inference algorithms perform similarly on real data compared with time series simulated from the model**

Researchers often pass the fluorescence time series through a spike inference tool before performing further statistical analyses. These spike inference algorithms take the fluorescence trace as input and attempt to estimate the neuronal spike train that triggered them (Vogelstein et al., 2010; Pnevmatikakis et al., 2016; Friedrich and Paninski, 2016; Pnevmatikakis et al., 2013; Pnevmatikakis et al., 2014; Deneux et al., 2016). Part of our motivation for building

## 2.3. Results

958 this model was to allow us to ask the question on non-linearities properties of the cell and the cal-  
959 cium indicator affect the quality of spike inference? In order to trust the conclusions from  
960 our model, we should first be confident that spike inference from our simulated fluorescence  
961 traces is similar to that from the real data. To test this we passed each of the simulated fluores-  
962 cence traces through three previously published spike inference algorithms, quantified their  
963 performance against the ground-truth electrophysiology data, repeated the procedure for the  
964 real calcium fluorescence time series, and compared the accuracy of the inference processes  
965 in all cases. The *true positive rate*, also known as the *recall*, the *sensitivity*, or the *probabi-*  
966 *lity of detection* of spike inference varied across the three inference algorithms we tried (*p*  
967 value and statistical test here). The constrained non-negative matrix deconvolution algorithm  
968 (Pnevmatikakis et al., 2016) (CNMD algorithm) correctly detected approximately 45% of the  
969 true spikes, the OASIS algorithm (Friedrich and Paninski, 2016) correctly detected approx-  
970 imately 35% of the true spikes, and the ML spike algorithm (Deneux et al., 2016) correctly  
971 detected approximately 15% of the true spikes (see figure 2.2). Notably, for two of the three  
972 inference algorithms, the quality of inference was also fairly consistent for individual spike  
973 trains, not just the group means ( $p > 0.05$ , paired t-test). This demonstrates that the models  
974 were generating fluorescence time series that were similarly difficult to decode as the real  
975 data, in ways that were not specific to any one inference algorithm. This is evidence that the  
models captured real aspects of the spikes-to-fluorescence transform.

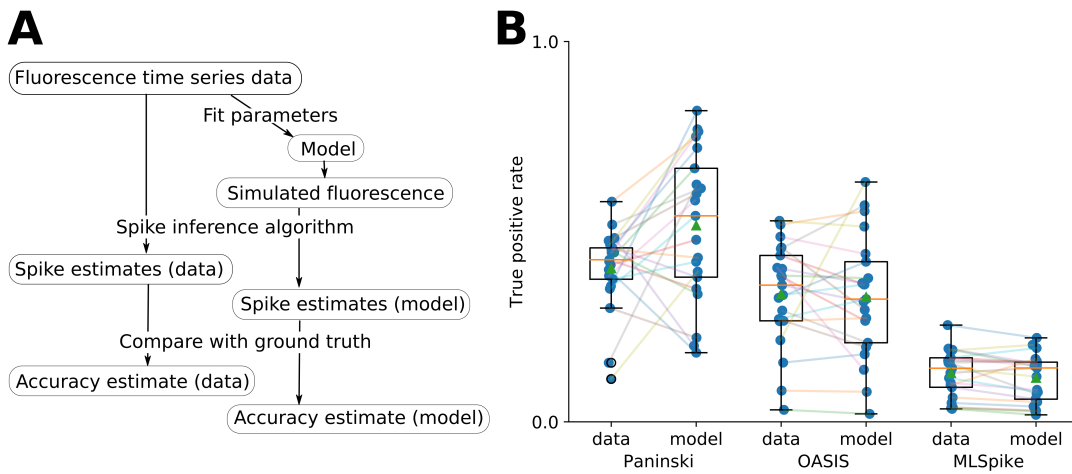


FIGURE 2.2:  
A: Workflow to compare spike inference for real versus simulated fluorescence data.  
B: True positive rates achieved by three different spike inference algorithms when applied to observed spike trains, and simulated spike trains. Data points overlaid as blue circles. The performance is similar from real and simulated data for each of the algorithms.  
quantities

### 976 2.3.3 Relative effects of various buffers to the fluorescence signal

977 One of the benefits of computational models over laboratory experiments is that we can  
978 observe all the variables in the simulation to gain insight into the system's dynamics, which  
979 can be difficult to do in the lab. We plotted the concentrations of the various species over  
980 time for a version of the model fit to one data set, in response to the same train of spikes used  
981 for fitting (figure 2.3). Figure 2.3a shows the absolute values of the species concentrations,  
982 summed. Consistent with experimental estimates (Maravall et al., 2000), only a small fraction  
983 ( $\sim 0.1\%$ ) of calcium is free and unbound to any buffer. Of the bound calcium, the vast  
984 majority, ( $\sim 96\%$ ) is bound to the GCaMP indicator. The two types of endogenous buffer  
985 are bound to the remaining calcium ( $\sim 4\%$ ). An influx of calcium from a single spike adds  
986 very little to the total calcium, in relative terms (red line in Figure 3a).

987 When calcium entered the model neuron it was rapidly buffered (Bartol et al., 2015).  
988 However the relative fractions of which buffer molecules bound to the influxed calcium was  
989 dynamic, and changed over time . Figure 2.3 (b-f) shows the time course of the various  
990 species over time in response to a calcium influx event from a single action potential. Cru-  
991 cially, the indicator  $[BCa]$  competed with the endogenous buffers  $[ImCa]$  and  $[ECa]$  – all  
992 three bind calcium on similar timescales. This implies that the timecourse and amplitude of  
993 the  $[BCa]$  variable will also depend on the binding rates and availabilities of the endogenous  
994 buffers. For example if we decreased the concentration of an endogenous buffer, we might  
995 expect both a faster rise time and greater peak amplitude of the  $[BCa]$  signal in response to  
996 a calcium influx event. The slowest component of the decay had a similar time constant for  
997  $[BCa]$ ,  $[ImCa]$  and  $[ECa]$ , which in turn matched the  $[Ca]$  extrusion time constant in our  
998 model ( $\sim 6.29 \times 10^{-22} \text{Ms}^{-1}$ ). This implies that the buffers and the indicator had reached  
999 a dynamic equilibrium and were jointly tracking the free calcium concentration as calcium  
1000 was slowly extruded from the cell.

1001 Interestingly the excited bound calcium species ( $[BCa^*]$ ) showed a qualitatively different  
1002 timecourse in response to a calcium influx event. This concentration is subject to the added  
1003 ‘excitation and release’ dynamic, where a certain proportion of the concentration absorbs the  
1004 energy from an incoming photon and goes into an ‘excited state’ at each time step. A certain  
1005 proportion of the concentration releases a photon and reverts to a ‘relaxed state’ at each  
1006 timestep also. This means that the excited bound calcium lags behind the bound calcium

### 2.3. Results

---

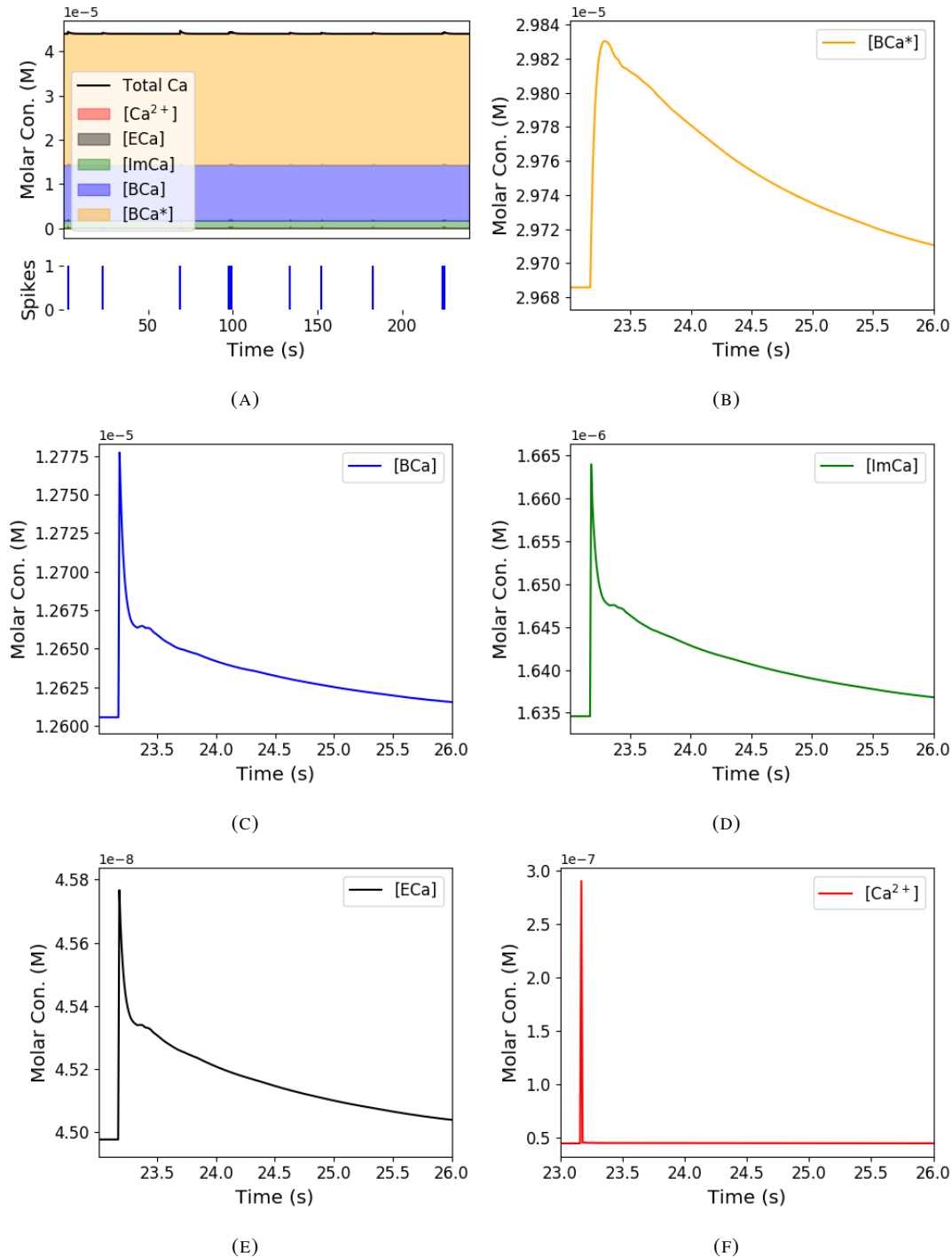


**FIGURE 2.3: Calcium Buffering Dynamics** (A) The proportions of bound and free calcium concentrations within a cell, with the associated spike train. (B)-(F) The dynamics of the concentration of (B) excited indicator bound calcium, (C) indicator bound calcium, (D) immobile endogenous buffer bound calcium, (E) mobile endogenous buffer bound calcium, and (F) free calcium in response to an action potential at  $\sim 23.2$ s.

trace. We could think of the excited bound calcium trace as a low pass filtered version of the bound calcium trace.

**2.3.4 Spike inference accuracy is sensitive to indicator properties, and likely varies within and between cells**

The above results imply that the fluorescence signal depends on the relative properties of both GCaMP and the endogenous buffers. We next used the model to directly ask how sensitive spike inference was to these components. We focused on three key parameters that likely vary from cell to cell and experiment to experiment: GCaMP binding kinetics, GCaMP concentration, and endogenous buffer concentration.

Several variants of GCaMP itself have been made that differ in calcium binding kinetics, baseline fluorescence, fluorescence efficiency, and other factors. For example, GCaMP6f has a decay time constant of  $\sim 1\text{s}$ , while GCaMP6s has a decay time constant of  $\sim 2\text{s}$  (Chen et al., 2013). Here we asked how these differences in binding kinetics affect spike inference. We jointly varied the calcium binding and unbinding rates of the indicator by the same factor over a range from 100-fold slower to 100-fold faster from the fitted values, and simulated the fluorescence response for each of the parameter settings in response to the same spike trains as before (figure 2.4). Notably this manipulation does not affect the indicators affinity, and therefore would not affect steady-state responses to prolonged changes in calcium. Instead it is likely to affect its sensitivity to the spike train dynamics. We computed two summary measures from the simulated fluorescence traces: the signal-to-noise ratio for a single spike (Methods, section 2.2.6), and the accuracy of spike inference for each of the spike trains. We observed a reduction in the signal-to-noise ratio and the spike inference quality when we set the binding and unbinding rates were set to one hundredth of their fitted values, and to one tenth of their fitted values. When we increased the value of both binding rates, we observed no change in these measurements. The reduction in both rates lead to smaller increases in fluorescence in response to an action potential and a longer decay time (figure 2.4a), this caused the reduction in signal-to-noise ratio. As both rates were increased, the change in  $\Delta F/F_0$  in response to an action potential increased and the decay time decreased slightly, but the fluorescence trace created by these values was very similar to the trace created by the fitted values.

Second, the overall concentrations of GCaMP often varies from cell to cell. For example different cells, even of the same type in the same tissue, can express different levels of GCaMP, due to proximity to the infection site, or the cell becoming ‘nuclear-filled’ (Tian et

### 2.3. Results

---

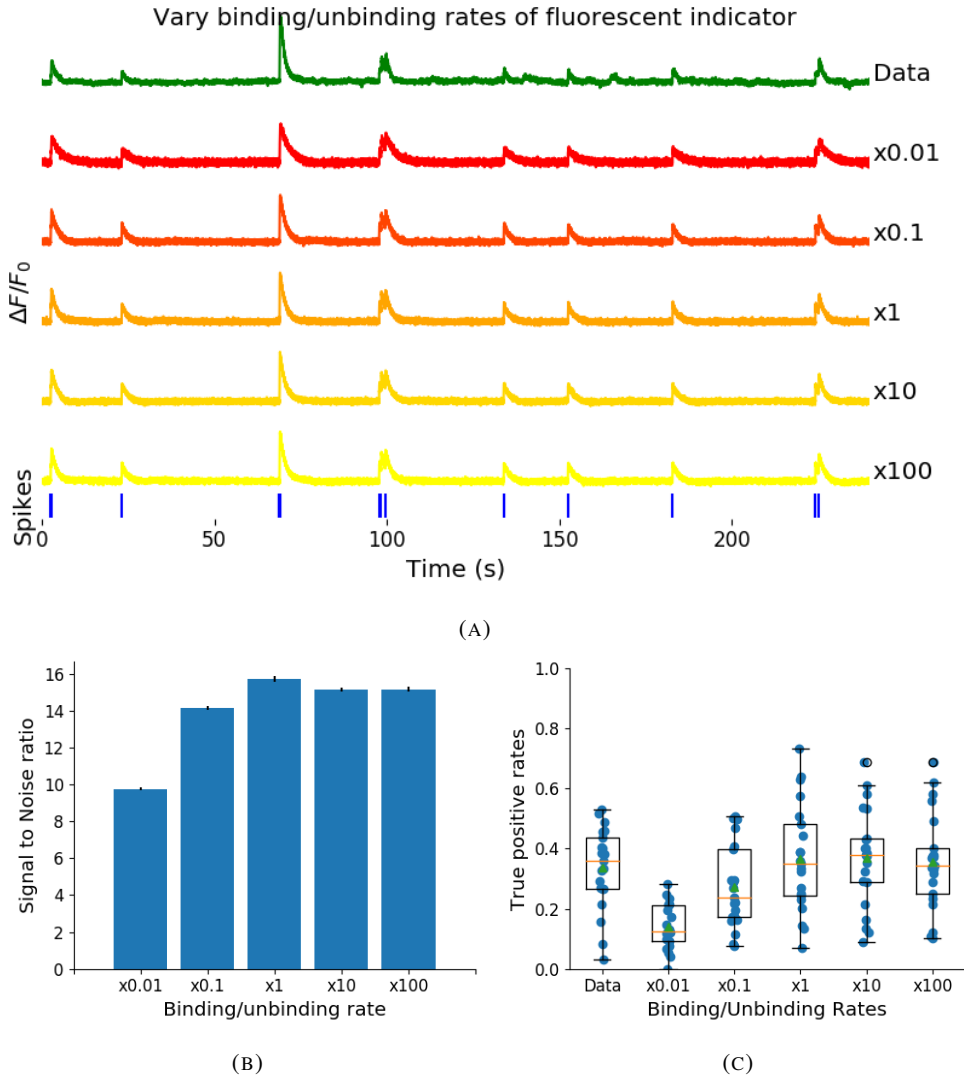


FIGURE 2.4: (A) An example trace for each of the five pairs of values used for the binding and unbinding rates of the fluorescent calcium indicator. (B) The signal-to-noise ratio of the modelled fluorescence traces using each of the four perturbed value pairs, and the experimental value. The SNRs for the value pairs perturbed downward are lower than that for the unperturbed value pair or the higher value pairs. (C) The true-positive rates of the deconvolution algorithm's predictions when inferring from the observed data, and inferring from modelled traces using the perturbed and experimental values.

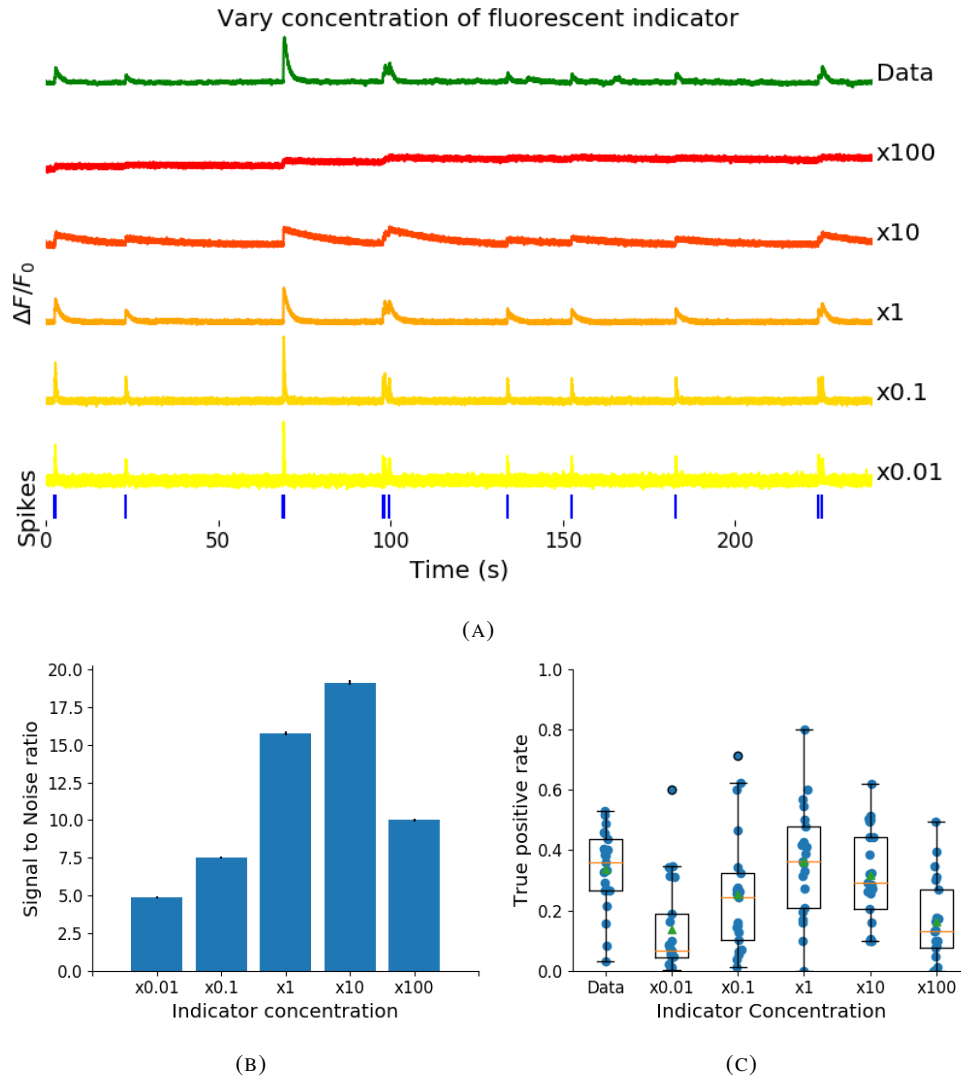


FIGURE 2.5: (A) An example trace for each of the five perturbed values for the concentration of fluorescent calcium indicator. The top two traces are produced by the lower perturbed values, the middle trace is produced by the experimental value, and the lowest two traces are produced when using the higher perturbed values. (B) The signal-to-noise ratio of the modelled fluorescence traces using each of the four perturbed values, and the experimental value. Extreme perturbations of the concentration either above or below the experimental level lowered the SNR. (C) The true-positive rates of the deconvolution algorithm's predictions when inferring from the observed data, and inferring from modelled traces using the perturbed and experimental values. We found that the algorithms performs equally badly on the two most extreme values, and performs equally well on the experimental value, and the next higher perturbed value.

## 2.3. Results

---

al., 2009; Chen et al., 2013). Also, GCaMP is often used for longitudinal experiments where the same cells are re-imaged across multiple days or weeks. However since GCaMP expression typically ramps up over time (Chen et al., 2013), the accuracy of spike inference may differ across multiple longitudinal recordings in the same cell. We addressed this by varying the concentration of calcium indicator in the model, simulating spike trains and measuring signal-to-noise ratio and spike inference accuracy on the resulting fluorescence traces. Both increasing and decreasing the concentration of the indicator had effects on the fluorescence trace, signal-to-noise ratio, and spike inference. The signal-to-noise ratio and spike inference quality decreased with decreased indicator concentration, and both showed a decrease when the indicator concentration was increased to 100 times its fitted value (figure 2.5). The signal-to-noise ratio showed an increase when the indicator concentration was increased to 10 times its fitted value, but there was no corresponding change in the spike inference quality. The decrease in indicator concentration caused a reduction in the increase in  $\Delta F/F_0$  in response to an action potential, and an increase in the decay time of this increase (figure 2.5a). The increase in indicator concentration had the opposite effect, it caused an increase in the change in  $\Delta F/F_0$  in response to an action potential, and a decrease in the decay time.

Third, the concentration and types of endogenous calcium buffers also vary from neuron to neuron, both within and between cell types (Bartol et al., 2015; Maravall et al., 2000; Neher and Augustine, 1992). Since the calcium buffer capacity of neurons is high, around 50-70 (Lee et al., 2000) in excitatory hippocampal pyramidal cells, around 100-250 (Lee et al., 2000) in inhibitory hippocampal pyramidal cells, and 900-200 in Purkinje cells (depending on the age of the subject), these endogenous buffers compete with GCaMP for binding to calcium, and variations in endogenous buffer concentration may affect GCaMP signal and therefore spike inference. To address this we varied the concentration of the endogenous buffer in the model neuron over five orders of magnitude from 0.8 to 8000  $\mu\text{M}$ , simulated calcium fluorescence traces in response to the same set of spike trains, and performed spike inference on the resulting fluorescence time series. Increasing the endogenous buffer concentration had a substantial effect on the GCaMP fluorescence signal, both decreasing its amplitude and slowing its kinetics (figure 2.6(a)). This corresponded with a decrease in both single-spike signal-to-noise ratio (figure 2.6(b)) and spike inference accuracy (figure 2.6(c)). In contrast, decreasing endogenous buffer capacity from the fitted value had little effect on either the GCaMP signal or spike inference (figure 2.6).

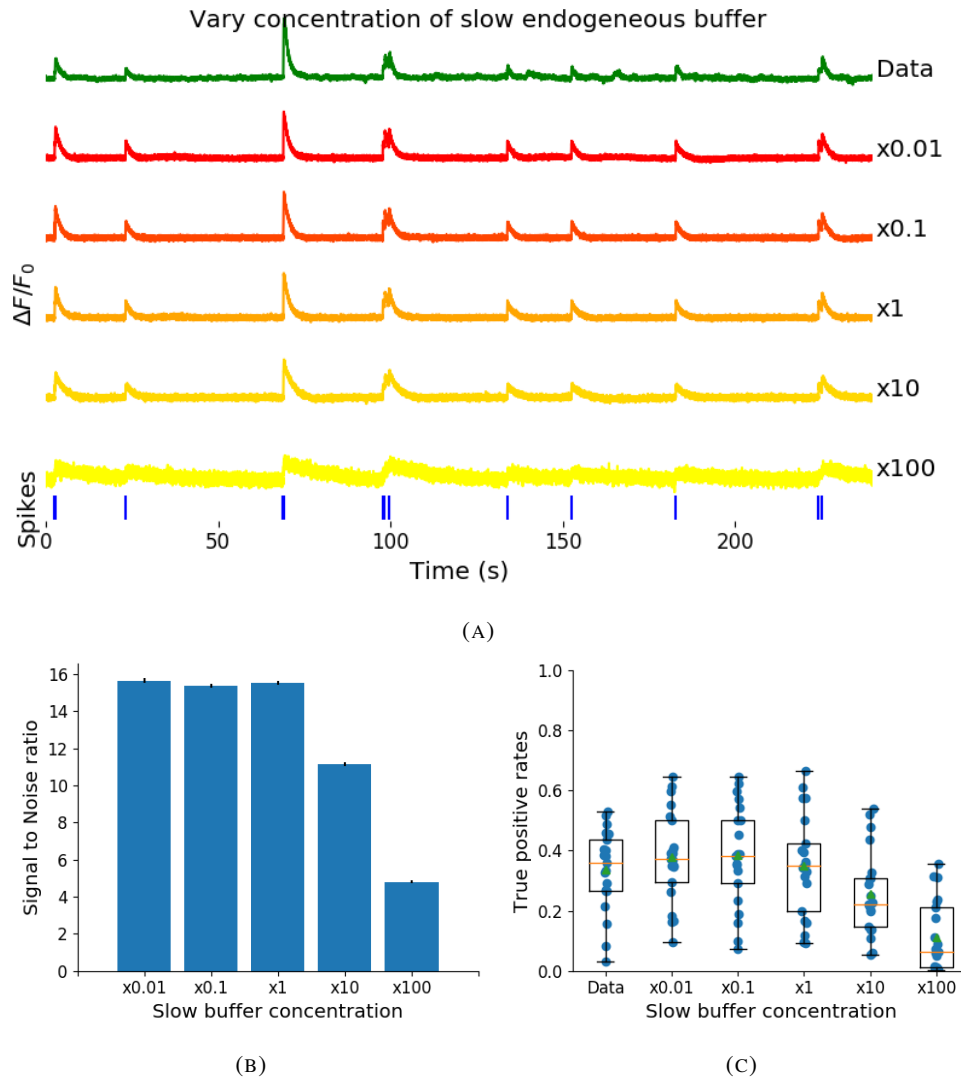


FIGURE 2.6: (A) An example trace for each of the five perturbed values for the concentration of immobile endogenous buffer. (B) The signal-to-noise ratio of the modelled fluorescence traces using each of the four perturbed values, and the experimental value. The lower values for the immobile buffer produce the same SNR as the experimental value. But the higher perturbed values produce fluorescence traces with a lower SNR. (C) The true-positive rates of the deconvolution algorithm's predictions when inferring from the observed data, and inferring from modelled traces using the perturbed and experimental values.

**2.3.5 Single spike inference accuracy drops for high firing rates, but firing rate itself can be estimated from mean fluorescence amplitude**

The fluorescence signal recorded from neurons using calcium indicators is typically much slower than changes in membrane potential for two reasons: first, because the calcium and the indicator have slow binding and unbinding kinetics, the signal is a low-pass filtered version of the membrane potential. Second, neuronal two-photon imaging experiments are often performed in scanning mode, which limits their frame rate to  $\sim 10\text{Hz}$  or slower. This implies that multiple spike events that occur close in time might be difficult to resolve from a calcium indicator time series. Many cells, especially several types of inhibitory interneurons, fire tonically at rates higher than  $10\text{Hz}$ . We used the model to test whether spike inference accuracy depended on the neuron's firing frequency by driving the cell with spike trains sampled from a Poisson processes of varying frequency. We simulated a variable firing rate using an Ornstein-Uhlenbeck process, and simulated the spike trains using a Poisson distribution with its rate taken from this process. Because of the high frequency firing rate of these spike trains, we used the accuracy as the measure of spike inference quality. We simulated 30 spike trains at average firing rate of 1, 5, and  $10\text{Hz}$ , and measured the spike inference quality of all these traces. Spike inference accuracy decreased with increasing firing rate, for up to  $10\text{Hz}$  Poisson spike trains (figure 2.8(left)). Although the accuracy remained above 90% for each of the three frequencies. We also plotted the average  $\Delta F / F_0$  as a function of stimulation firing rate. We found that it increased monotonically as a function of firing rate (figure 2.8(right)).

We expected lower spike inference quality as the average spiking frequency increased. Since the fluorescence trace, in some sense, is a low pass filtered version of the spike train, a tightly packed groups of spikes will be more difficult to infer than isolated spikes. However, the increasing amplitude of the fluorescence trace with increasing frequency suggests that some spike inference algorithm could be developed based on this amplitude.

**2.4 Discussion**

We designed a biophysical model for the changes in free calcium and bound calcium concentrations within a cell soma with a fluorescent calcium indicator. We used this model to model the fluorescence trace resulting from a spike train in this cell. We fit the free parameters of the model by matching the power spectrum and amplitude of fluorescence traces with simultaneously measured spike trains. We inferred spikes from real fluorescence traces and

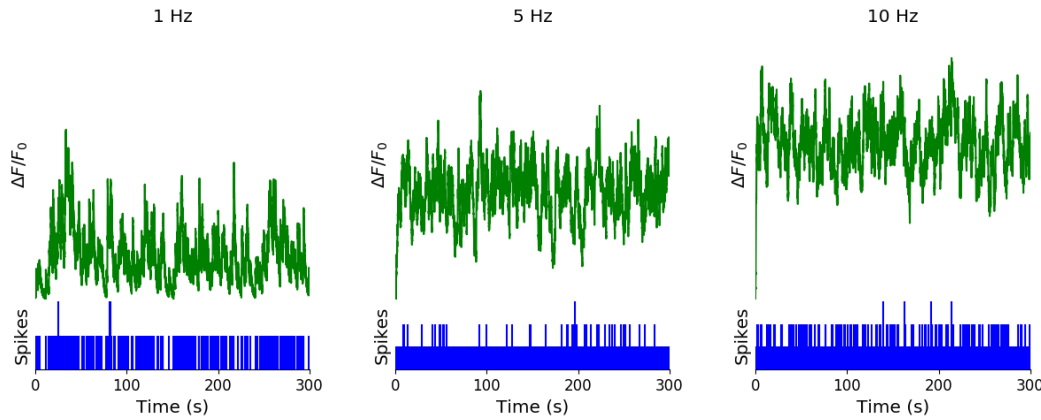


**FIGURE 2.7: Simulating fluorescence traces at different firing rates** Example modelled traces created using simulated spike trains with a mean firing rate of 1Hz (left column), 5Hz (middle column), and 10Hz (right column). Note the difference in amplitude with different mean firing rates.

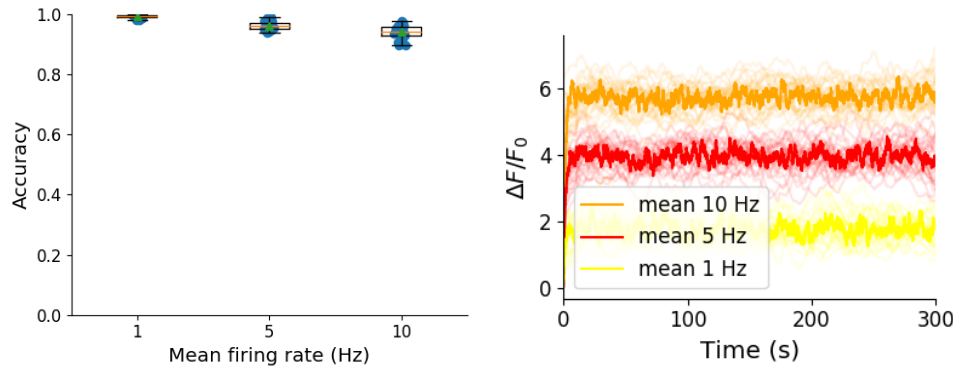


**FIGURE 2.8: Inference quality and  $\Delta F/F_0$  vs Firing rate** (left) The spike inference accuracy when applied to 30 traces created using simulated spike trains with mean firing rates of 1, 5, and 10 Hz. (right) The mean  $\Delta F/F_0$  across those 30 traces for each frequency.

1104 modelled fluorescence traces, and measured the quality of the spike inference in both cases.  
 1105 We found that the spike inference quality was similar in both cases. We perturbed the concen-  
 1106 tration of the calcium buffers in the model, and the binding/unbinding rates of those buffers  
 1107 in the model, and measured the effect on the signal-to-noise ratio (SNR) of the modelled  
 1108 fluorescence traces and the spike inference quality.

1109 For the fluorescent calcium indicator, we found that any large perturbation away from  
 1110 the taken from the literature led to a reduction in SNR, and spike inference quality. For the  
 1111 binding/unbinding rates, we kept the ratio of these rates constant, but altered their values in  
 1112 parallel. The lower values caused a reduction in SNR, and a reduction in spike inference  
 1113 quality. For the endogenous buffer concentration, an increase above the experimental value  
 1114 caused a reduction in SNR and spike inference quality.

## 2.4. Discussion

---

1115     Although the model produced visually similar time series to the real data, there were a  
1116     few aspects it did not capture. First, the real data featured some low-frequency components  
1117     that did not appear related to the spike events. These were not captured by the models we  
1118     used in this study, but could be added in future by adding a suitable low-frequency term to the  
1119     resulting time series. Second, the real data seemed to have some non-linearities not captured  
1120     in the model, for example the response to two nearby spikes was greater than expected from  
1121     the linear sum of two single spikes. This may be due to the co-operative binding of calmod-  
1122     ulin to calcium, which gives calmodulin a supra-linear sensitivity to calcium concentration  
1123     (Faas et al., 2011). The non-linear dynamics of this binding have been included in a recently  
1124     developed spike inference model (Greenberg et al., 2018). Our model, in contrast, behaved  
1125     much more linearly but could be extended in future to include such non-linearities. Third,  
1126     in the real data the fluorescence peak amplitude seemed to vary from spike to spike, even  
1127     for well-isolated spike events. Recent research has shown that calcium influx due to a single  
1128     action potential was quite variable in pyramidal cells, and that this variability had a effect on  
1129     spike inference (Éltes et al., 2019). However in our model we assumed each spike lead to the  
1130     same fixed-amplitude injection of calcium to the cell, leading to much greater regularity in  
1131     fluorescence peak amplitudes. This variability could be added in future versions of the model  
1132     by making the injected calcium peak a random variable. Fourth, we modelled the soma as  
1133     a single compartment, but in reality there is likely a non-uniform spatial profile of calcium  
1134     concentration. This may matter because some endogenous buffers might access calcium right  
1135     as it influxes from the extracellular space, whereas the majority of the fluorescence signal is  
1136     more likely coming from the bulk of the cytoplasm. Future models could attempt to model  
1137     these spatial dependencies to assess whether they affect the overall spike inference procedure.

1138     As well as the optimised parameters, the model has 14 fixed parameters than can be  
1139     changed to simulate different types of calcium indicators. This model could be used to test  
1140     the theoretical performance of proposed new types of calcium indicator. The model could  
1141     also be used by developers of spike inference algorithms to test the effects of changing cal-  
1142     cium indicator parameters on spike inference, or to test the affects of changing spiking char-  
1143     acteristics on spike inference. For example, high firing rate vs low firing rate, or bursting vs  
1144     no bursting. Given the increasing amplitude of the fluorescence trace with increasing mean  
1145     firing rate, it would be possible to build a spike inference algorithm on this principle at least  
1146     in part.

1147     Our model has already been used as a tool by our colleagues, for simulating fluorescence  
1148     traces in response to cells that can fire with a continuous rate between 10 and 20Hz, but do

1149 not always do so. Our colleagues found that a combination of the amplitude and the variance  
1150 of the simulated fluorescence trace was the best indicator of firing rate. For example, when  
1151 a cell was not firing, the amplitude and variance of the fluorescence trace was relatively low.  
1152 When the cell fired with a low firing rate  $\sim 1\text{Hz}$ , the mean amplitude was still low but  
1153 the variance of the fluorescence trace was high, and for high firing rate  $\sim 10 - 20\text{Hz}$ , the  
1154 fluorescence amplitude was high, and the variance was low. In this way, our model may be  
1155 useful for investigating firing rates underlying real fluorescence traces in response to cells  
1156 which can fire in these rage ranges.

1157 A recent paper by Greenberg et al (2018) described a biophysical model for spike train  
1158 inference called the ‘Sequential binding model’. Their model for spike inference was sim-  
1159 ilar to our model for fluorescence traces in that their model included parameters for two  
1160 types of endogenous buffer. But this model also included dynamics for calcium binding to  
1161 and unbinding from these endogenous buffers. Furthermore, this model included dynamics  
1162 for calcium binding to and unbinding from the four binding sites present on a GCaMPs6  
1163 molecule. In the accuracy measurements specified in that paper, this model performed better  
1164 than the MLspike algorithm, which is also partially a biophysically model, and it performed  
1165 better than the constrained non-negative deconvolution algorithm. The sequential binding  
1166 model also has biophysically interpretable parameters, and its fitted parameters for quantities  
1167 such as buffering capacity and calcium influx upon action potential firing fall in line with  
1168 experimental values (Greenberg et al., 2018). Biophysical models like this appear to be the  
1169 way forward for spike inference algorithms, and would make a good complimentary tool to  
1170 our fluorescence model.

1171 **Chapter 3**

1172 **Functional networks expand across  
1173 anatomical boundaries as correlation  
1174 time-scale increases**

1175 *Abstract*

1176 Decades of research has established that correlated spiking plays a crucial role in represent-  
1177 ing sensory information. One drawback associated with the recent improvement in recording  
1178 technology and consequent large datasets is the difficulty in analysing higher order correla-  
1179 tions in large neuronal ensembles. One benefit of these datasets that has not yet been explored  
1180 is the opportunity to compare correlations within anatomical regions to correlations across  
1181 anatomical regions. In this work, we measured correlations between neurons residing in  
1182 nine different brains regions in three awake and behaving mice. Using the these correlation  
1183 measurements, we created weighted undirected graph networks and applied network science  
1184 methods to detect functional communities in our neural ensembles. We compared these func-  
1185 tional communities to their anatomical distribution. We repeated the analysis, using different  
1186 timescales for our correlation measurements, and found that functional communities were  
1187 more likely to be dominated by neurons from a single brain region at shorter timescales  
1188 (< 100ms).

**1189 3.1 Introduction**

1190 Decades of research has established that correlations play a crucial role in representing sen-  
1191 sory information. For example, the onset of visual attention has been shown to have a greater  
1192 affect on the correlations in the macaque V4 region than on the firing rates in that region  
1193 (Cohen and Maunsell, 2009). Recent findings show that spontaneous behaviours explain cor-  
1194 relations in parts of the brain not associated with motor control (Stringer et al., 2019), that  
1195 satiety state appears to have a brain wide representation (Allen et al., 2019), and that subject  
1196 exploratory and non-exploratory states are represented in the amygdala (Gründemann et al.,  
1197 2019). So, behavioural states are likely represented across many regions of the brain, not just  
1198 motor related areas. In order to understand the brain, we must understand the interactions  
1199 between neurons and regions.

1200 Because of limitations in recording technology almost all research has explored corre-  
1201 lations between neurons within a given brain region, or within only two regions at most  
1202 (Wierzynski et al., 2009; Patterson et al., 2014; Girard, Hupé, and Bullier, 2001). Rela-  
1203 tively little is known about correlations between neurons in many different brain regions.  
1204 However, the recent development of ‘Neuropixels’ probes (Jun et al., 2017) has allowed  
1205 extracellular voltage measurements to be collected from multiple brain regions simultane-  
1206 ously routinely, and in much larger numbers than traditional methods. In this project we  
1207 used a publicly-available Neuropixels dataset to analyse correlations between different brain  
1208 regions (Stringer et al., 2019).

1209 A drawback associated with the improvement in recording technology is an increase in  
1210 the difficulty in analysing these data. For example, analysing the  $i$ th order interactions of  
1211  $N$  neurons generally requires estimation of  $N^i$  parameters. A number that becomes astro-  
1212 nomical for large  $N$ . New methods are required for analysing these new large datasets. We  
1213 attempted to address this requirement in this piece of research by applying a cutting-edge  
1214 network science community detection method to neural data.

1215 Another unexplored area of research is the changes in cell interactions at different timescales.  
1216 Studies have shown different timescales for fluctuations in spiking activity (Murray et al.,  
1217 2014), and different time scales for event representation (Baldassano et al., 2017) across dif-  
1218 ferent brain regions. Still most studies focus on quantifying interactions at a given timescale.  
1219 But neurons may interact differently, or may interact with different neurons at different  
1220 timescales. Here we explore correlated communities of neurons at different timescales.

1221 In this work, we measured correlations between binned spike counts from neurons from

### 3.2. Data

---

1222 nine different regions of the mouse brain. These measurements induced a weighted undi-  
1223 rected graph or network where each neuron is represented by a node, and the strength of  
1224 the connection between these nodes/neurons is the strength of the correlation between their  
1225 spike counts. We then applied newly invented network methods (Humphries et al., 2019)  
1226 to this network to find any community structure, and place the neurons in these correlation  
1227 based communities. Finally, we compared these functional communities to the anatomical  
1228 membership of the neurons.

1229 To investigate the functional communities and their relationship with anatomy at different  
1230 time scales, we repeated these analyses using different length bin widths when binning spike  
1231 times.

1232 To find and analyse functional networks while controlling for the subject’s behaviour, we  
1233 conditioned the binned spike counts on data from a video of the subject’s face, and repeated  
1234 our analysis for spike count correlations (or noise correlations) and signal correlations.

## 1235 3.2 Data

1236 The data that we used in this project were collected by Nick Steinmetz and his lab members  
1237 (Stringer et al., 2019; Steinmetz et al., 2019).

### 1238 3.2.1 Brain regions

1239 Neuropixels probes were used to collect extracellular recordings (Jun et al., 2017) from three  
1240 different mice. The mice were awake, headfixed, and engaging in spontaneous behaviour.  
1241 The mice were of different sexes and different ages. One mouse was ‘wild-type’, the others  
1242 were mutants. Details as follows:

- 1243 1. male, wild type, P73.
- 1244 2. female, TetO-GCaMP6s, Camk2a-tTa, P113
- 1245 3. male, Ai32, Pvalb-Cre, P99

1246 Eight probes were used to collect readings from 2296, 2668, and 1462 cells respectively.  
1247 Data were collected from nine brain regions in each mouse:

- 1248 • Caudate Putamen (CP)
- 1249 • Frontal Motor Cortex (Frmocxt)
- 1250 • Hippocampal formation (Hpf)

- 1251     ● Lateral Septum (Ls)
- 1252     ● Midbrain (Mb)
- 1253     ● Superior Colliculus (Sc)
- 1254     ● Somatomotor cortex (Sommotcx)
- 1255     ● Thalamus (Th)
- 1256     ● Primary visual cortex (V1)

1257   Readings were continuous and lasted for about 1 hour (Stringer et al., 2019; Steinmetz et al.,  
1258 2019). Locations of each of the probes can be seen in figure 3.1.

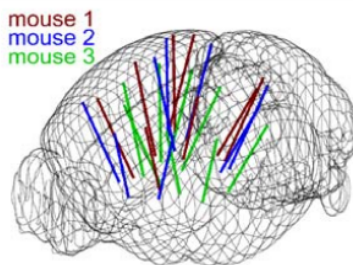


FIGURE 3.1: **Probe Locations:** The locations of the probes in each of the three mouse brains (Stringer et al., 2019).

### 1259 3.2.2 Video recordings

1260 Video recordings of the mouse's face were taken during the spontaneous behaviour. We  
1261 had access to the top 500 principal components and top 500 eigenvectors of the processed  
1262 videos. The frequency of recording was slightly less than 40Hz. Each frame contained  
1263  $327 \times 561$  pixels (Stringer et al., 2019; Steinmetz, Carandini, and Harris, 2019). These  
1264 principal components were used as behavioural data. We controlled for these components  
1265 when taking measurements conditioned on behaviour.

## 1266 3.3 Methods

### 1267 3.3.1 Binning data

1268 We transformed the spike timing data into binned spike count data by dividing the experi-  
1269 mental period into time bins and counting the spikes fired by each cell within the time period  
1270 covered by each of those bins. The data were divided into time bins of various widths ranging  
1271 from 0.005s to 4s.

### 3.3. Methods

---

If the total length of the recording period was not an integer multiple of the time bin width, we cut off the remaining time at the end of the recording period. This period was at most 3.99s. This is far less than the total recording time of around 1 hour. So, this detail would not affect our results.

#### 3.3.2 Correlation coefficients

We calculated Pearson's correlation coefficient for pairs of spike counts from pairs of neurons. For jointly distributed random variables  $X$  and  $Y$ , Pearson's correlation coefficient is defined as:

$$\rho_{XY} = \frac{\text{cov}(X, Y)}{\sigma_X \sigma_Y} \quad (3.1)$$

$$= \frac{E[(X - \mu_X)(Y - \mu_Y)]}{\sigma_X \sigma_Y} \quad (3.2)$$

where  $E$  denotes the expected value,  $\mu$  denotes the mean, and  $\sigma$  denotes the standard deviation. The correlation coefficient is a normalised measure of the covariance. It can take values between 1 (completely correlated) and  $-1$  (completely anti-correlated). Two independent variables will have a correlation coefficient of 0. But, having 0 correlation does not imply independence.

If we do not know the means and standard deviations required for equation 3.1, but we have samples from  $X$  and  $Y$ , Pearson's sample correlation coefficient is defined as:

$$r_{XY} = \frac{\sum_{i=1}^n (x_i - \bar{x})(y_i - \bar{y})}{\sqrt{\sum_{i=1}^n (x_i - \bar{x})^2} \sqrt{\sum_{i=1}^n (y_i - \bar{y})^2}} \quad (3.3)$$

where  $\{(x_i, y_i)\}$  for  $i \in \{1, \dots, n\}$  are the paired samples from  $X$  and  $Y$ , and  $\bar{x} = \frac{1}{n} \sum_{i=1}^n x_i$ , and  $\bar{y} = \frac{1}{n} \sum_{i=1}^n y_i$  are the sample means.

In practice we used the python function `scipy.stats.pearsonr` to calculate the correlation coefficients.

#### 1286 Total correlations, $r_{SC}$

In this context, we defined the total correlation ( $r_{SC}$ ) of two cells to be the correlation between the spike counts of those cells across the entire period of spontaneous behaviour.

1289 **Shuffled total correlations**

1290 We measured the shuffled total correlations between two neurons by randomly permuting one  
 1291 of the neuron's spike counts and measuring the total correlations. These shuffled correlations  
 1292 were useful when measuring the effect of time bin width on correlations, and when decid-  
 1293 ing which correlations should be preserved when creating correlation networks (see section  
 1294 3.3.5).

1295 **Separating Correlations & Anti-correlations**

1296 In order to compare the effect of bin width on measures of negative  $r_{SC}$  (anti-correlation) and  
 1297 positive  $r_{SC}$  separately, we had to separate correlated and anti-correlated pairs. To do this, we  
 1298 simply measured the mean  $r_{SC}$ , taking the mean across all the bin widths. If this quantity was  
 1299 positive or zero we regarded the pair as positively correlated. If this quantity was negative  
 1300 we regarded the pair as anti-correlated.

1301 **3.3.3 Conditioning on behavioural data**

Our behavioural data consisted of the top 500 principal components (PCs) of a processed video recording of the mouse's face (see section 3.2.2). Denoting the spike count of a given cell by  $X$ , and the PCs by  $Z_1, \dots, Z_{500}$ , we wanted to model  $X$  as a function of  $Z_1, \dots, Z_{500}$  in order to estimate

$$E[X|Z_1, \dots, Z_{500}] = \int_{x \in X} x P(X = x|Z_1, \dots, Z_{500}) dx \quad (3.4)$$

$$= \int_{x \in X} x \frac{P(X = x, Z_1, \dots, Z_{500})}{P(Z_1, \dots, Z_{500})} dx \quad (3.5)$$

1302 Given the 500 components, a naïve estimation of  $P(Z_1, \dots, Z_{500})$  or  $P(X, Z_1, \dots, Z_{500})$  by  
 1303 histogramming was impossible. Therefore we modelled  $X$  as a linear combination of the  
 1304 PCs.

1305 **Linear regression**

1306 We modelled the spike count of a given cell,  $X$ , as a linear combination of the PCs of the  
 1307 video of the mouse's face,  $\mathbf{Z} = Z_1, \dots, Z_{500}$ . We tried three different types of regularization

1308 • L1 or 'Lasso'

1309 • L2 or 'Ridge regression'

### 3.3. Methods

---

- 1310 • ‘Elastic net’ regularisation (a linear combination of both  $L1$  and  $L2$  regularisation  
1311 penalties)

1312 The elastic net regularisation performed the best, so we stuck with that.

#### 1313 **Elastic net regularisation**

Suppose we wish to model  $n$  observations of a random variable  $X$ ,  $\mathbf{x} = (x_1, \dots, x_n)$  using  $n$  instances of  $m$  predictors  $\mathbf{Z} = (Z_1, \dots, Z_m)$ . The naïve elastic net criterion is

$$L(\lambda_1, \lambda_2, \boldsymbol{\beta}) = |\mathbf{x} - \mathbf{Z}\boldsymbol{\beta}|^2 + \lambda_2|\boldsymbol{\beta}|_2 + \lambda_1|\boldsymbol{\beta}|_1 \quad (3.6)$$

where

$$|\boldsymbol{\beta}|_2 = \sum_{j=1}^m \beta_j^2 \quad (3.7)$$

$$|\boldsymbol{\beta}|_1 = \sum_{j=1}^m |\beta_j| \quad (3.8)$$

The naïve elastic net estimator  $\hat{\boldsymbol{\beta}}$  is the minimiser of the system of equations 3.3.3 (Zou and Hastie, 2005)

$$\hat{\boldsymbol{\beta}} = \arg \min_{\boldsymbol{\beta}} L(\lambda_1, \lambda_2, \boldsymbol{\beta}) \quad (3.9)$$

1314 We implemented the model using the `ElasticNetCV` method of Python’s  
1315 `sklearn.linear_models` package. We chose to put equal weighting on the  $L1$  and  $L2$   
1316 regression parts of equation . We used 10-fold cross validation to set an optimised value for  
1317  $\lambda_1 = \lambda_2$ .

1318 As well as using the PCs, we also tried fitting the models using the raw video data recon-  
1319 structed from the PCs and eigenvectors. These models performed worse than those using the  
1320 PCs. We expected this because each representation contains the same amount of information,  
1321 but the raw video representation spreads this information across many more components.  
1322 This requires more parameter fitting, but given the same information.

1323 **Conditional covariance**

We calculated the expected value of the conditional covariance using the law of total covariance.

$$\text{cov}(X, Y) = E[\text{cov}(X, Y|Z)] + \text{cov}(E[X|Z], E[Y|Z]) \quad (3.10)$$

1324 where these expected values are calculated with respect to the distribution of  $Z$  as a random  
1325 variable.

1326 The law of total covariance breaks the covariance into two components. The first com-  
1327 ponent  $E[\text{cov}(X, Y|Z)]$  is the expected value, under the distribution of  $Z$ , of the conditional  
1328 covariance  $\text{cov}(X, Y|Z)$ . This covariance could be interpreted as the unnormalised version  
1329 of what Cohen et al. (2011) call the spike count correlation (Cohen and Kohn, 2011), aka.  
1330 the noise correlation. In particular, this is the covariance of the spike counts in response to  
1331 repeated presentation of identical stimuli.

1322 The second component is analogous to what Cohn et al. (2011) call the *signal correlation*  
1323 (Cohen and Kohn, 2011). In particular,  $\text{cov}(E[X|Z], E[Y|Z])$  is the covariance between  
1334 spike counts in response to different stimuli.

1335 Using our linear model, we calculated  $E[X|Z_1, \dots, Z_{500}]$  for each cell  $X$ . Then we pro-  
1336 ceeded to calculate

$$E[\text{cov}(X, Y|Z_1, \dots, Z_{500})] = \text{cov}(X, Y) - \text{cov}(E[X|Z_1, \dots, Z_{500}], E[Y|Z_1, \dots, Z_{500}]) \quad (3.11)$$

1337 **Measures of conditional correlation**

As a measure of expected correlation, we measured the ‘event conditional correlation’ (Maugis,  
2014)

$$\rho_{XY|Z} = \frac{E[\text{cov}(X, Y|Z)]}{\sqrt{E[\text{var}(X|Z)]E[\text{var}(Y|Z)]}} \quad (3.12)$$

1338 Although this is not an actual correlation, it is an intuitive analogue to the correlation as a  
1339 normalised version of the covariance.

For comparison, we also measured the ‘signal correlation’

$$\rho_{\text{signal}} = \frac{\text{cov}(E[X|Z], E[Y|Z])}{\sqrt{\text{var}(E[X|Z])\text{var}(E[Y|Z])}} \quad (3.13)$$

### 3.3. Methods

---

1340 this is an actual correlation.

#### 3.3.4 Information Theory

##### 1342 Entropy $H(X)$

The entropy of a random variable  $X$ , with outcomes  $x_1, \dots, x_N$ , and corresponding probabilities  $p_1, \dots, p_N$  is defined as

$$H(X) = - \sum_{n=1}^N p_n \log_2 p_n \quad (3.14)$$

1343 This quantity is also known as the information entropy or the ‘surprise’. It measures the  
 1344 amount of uncertainty in a random variable. For example, a variable with a probability of 1  
 1345 for one outcome, and 0 for all other outcomes will have 0 bits entropy, because it contains no  
 1346 uncertainty. But a variable with a uniform distribution will have maximal entropy as it is the  
 1347 least predictable. This quantity is analogous to the entropy of a physical system (Shannon,  
 1348 1948). Note that any base may be used for the logarithm in equation 3.14, but using base 2  
 1349 means that the quantity will be measured in ‘bits’.

The joint entropy of two jointly distributed random variables  $X$  and  $Y$ , where  $Y$  has outcomes  $y_1, \dots, y_M$ , is defined as

$$H(X, Y) = - \sum_{n=1}^N \sum_{m=1}^M P(X = x_n, Y = y_m) \log_2 P(X = x_n, Y = y_m) \quad (3.15)$$

1350 If  $X$  and  $Y$  are independent then  $H(X, Y) = H(X) + H(Y)$ . Otherwise  $H(X, Y) <$   
 1351  $H(X) + H(Y)$ . When  $X$  and  $Y$  are completely dependent and the mapping from  $X$  to  $Y$   
 1352 is on-to-one,  $H(X, Y) = H(X) = H(Y)$ .

The conditional entropy of  $Y$  conditioned on  $X$  is defined as

$$H(Y|X) = - \sum_{n=1}^N \sum_{m=1}^M P(X = x_n, Y = y_m) \log_2 \frac{P(X = x_n, Y = y_m)}{P(X = x_n)} \quad (3.16)$$

1353 When  $X$  and  $Y$  are independent  $H(Y|X) = H(Y)$ . Intuitively, we learn nothing of  $Y$  by  
 1354 knowing  $X$ , so  $Y$  is equally uncertain whether we know  $X$  or not. If  $Y$  is totally dependent  
 1355 on  $X$ , then the fraction in the logarithm is 1, which gives  $H(Y|X) = 0$ .

1356 These entropy measures are the basis of the mutual information measure.

1357 **Maximum entropy limit**

When spiking data is binned into spike counts there is an upper limit on the entropy of these data. The maximum entropy discrete distribution is the discrete uniform distribution. A random variable with this distribution will take values from some finite set with equal probabilities. Binned spike count data will take values between 0 and some maximum observed spike count  $n_{\max}$ . A neuron with responses that maximises entropy will take these values with equal probability, i.e. if  $i \in \{0, \dots, n_{\max}\}$  then  $P(X = i) = \frac{1}{n_{\max} + 1}$ . The entropy of this neuron will be

$$\begin{aligned} H(X) &= - \sum_{i=0}^{n_{\max}} P(X = i) \log_2 P(X = i) \\ &= - \sum_{i=0}^{n_{\max}} \frac{1}{n_{\max} + 1} \log_2 \left( \frac{1}{n_{\max} + 1} \right) \\ &= - \log_2 \left( \frac{1}{n_{\max} + 1} \right) \\ &= \log_2 (n_{\max} + 1) \end{aligned}$$

1358 Therefore, the maximum entropy of the binned spike counts of a neuron is  $\log_2 (n_{\max} + 1)$ .  
 1359 Of course, it would be very unusual for a neuron to fire in accordance with the discrete  
 1360 uniform distribution. Most measurements of entropy taken on binned spiking data will be  
 1361 much lower than the maximum. See figure 3.2 to see the maximum entropy as a function of  
 1362 the maximum observed spike count.

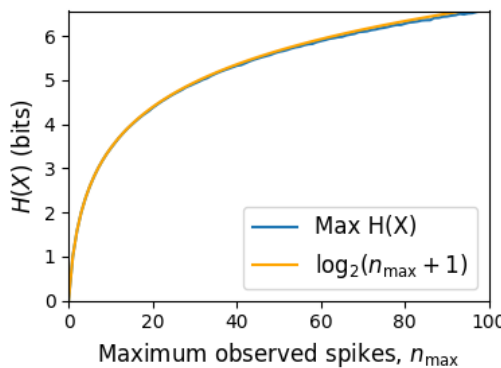


FIGURE 3.2: **Entropy Limit:** The upper limit on entropy of binned spike count data as a function of the maximum observed spike count. The orange line is the analytical maximum. The blue line is the entropy of samples with  $N = 1000$  data points taken from the discrete uniform distribution.

### 3.3. Methods

---

#### 1363 Mutual Information $I(X;Y)$

1364 The mutual information can be defined mathematically in a number of ways, all of which are  
1365 equivalent. These definitions illustrate the different ways of interpreting the mutual informa-  
1366 tion.

For two jointly distributed random variables  $X$  and  $Y$ , the mutual information  $I(X;Y)$  is defined as

$$I(X;Y) = H(Y) - H(Y|X) \quad (3.17)$$

$$= H(X) - H(X|Y) \quad (3.18)$$

1367 Equation 3.17 fits with the following intuition: The mutual information between  $X$  and  $Y$  is  
1368 the reduction in uncertainty about  $X$  gained by knowing  $Y$ , or vice versa. We could also say  
1369 the mutual information is the amount of information gained about  $X$  by knowing  $Y$ , or vice  
1370 versa.

Another useful entropy based definition for the mutual information is

$$I(X;Y) = H(X) + H(Y) - H(X,Y) \quad (3.19)$$

1371 This definition is useful because it does not require the calculation of conditional probabili-  
1372 ties.

The mutual information can also be defined in terms of marginal, joint, and conditional distributions. For example,

$$I(X;Y) = - \sum_{n=1}^N \sum_{m=1}^M P(X = x_n, Y = y_m) \log_2 \frac{P(X = x_n, Y = y_m)}{P(X = x_n)P(Y = y_m)} \quad (3.20)$$

Notice that this can be rewritten as a Kullback–Leibler divergence.

$$I(X;Y) = D_{KL}(P(X,Y) || P(X)P(Y)) \quad (3.21)$$

1373 So, we can also think of the mutual information as a measure of the difference between  
1374 the joint distribution of  $X$  and  $Y$ , and the product of their marginal distributions. Since the  
1375 product of the marginal distributions is the joint distribution for independent variables, we  
1376 can think of the mutual information as a measure of the variables' dependence on one another.

1377 The minimum value that  $I(X;Y)$  can take is 0. This occurs when the random variables  
1378  $X$  and  $Y$  are independent. Then we have  $H(X|Y) = H(X)$ , and  $H(Y|X) = H(Y)$ , which

according to equation 3.17, gives  $I(X;Y) = 0$ . We also have that  $H(X,Y) = H(X) + H(Y)$  in this case, which according equation 3.19, gives  $I(X;Y) = 0$ . Finally, we also have  $P(X,Y) = P(X)P(Y)$ , which leaves us with 1 in the argument for the logarithm in equation 3.20, which again gives  $I(X;Y) = 0$ .

The mutual information reaches its maximum value when one of the variables  $X$  and  $Y$  is completely determined by knowing the value of the other. In that case  $I(X;Y) = \min\{H(X),H(Y)\}$ .

### 1386 Variation of Information $VI(X,Y)$

The variation of information is another information theoretical quantity based on the mutual information. It is defined as

$$VI(X;Y) = H(X) + H(Y) - 2I(X;Y) \quad (3.22)$$

We can rewrite this as the summation of two positive quantities

$$VI(X;Y) = [H(X) - I(X;Y)] + [H(Y) - I(X;Y)] \quad (3.23)$$

In English, the variation of information is the summation of the uncertainty in the random variables  $X$  and  $Y$  excluding the uncertainty shared by those variables.

This measure will become more relevant when we go on to talk about clusterings because  $VI(X;Y)$  forms a metric on the space of clusterings.

### 1391 Measuring entropies & mutual information

In practice, we measured the mutual information between spike counts using Python and the python package `pyitlib`. We used the PT-bias correction technique to estimate the bias of our measurements when measuring the mutual information between the spike counts of two cells (Treves and Panzeri, 1995).

When measuring the mutual information between clusterings we used Python, but we used the `mutual_info_score`, `adjusted_mutual_info_score`, and `normalized_mutual_info_score` functions from the `sklearn.metrics` part of the `sklearn` package.

### 3.3. Methods

---

#### 3.3.5 Network analysis

##### Correlation networks

In order to analyse functional networks created by the neurons in our ensemble, we measured the total correlation between each pair of neurons. These measurements induced an undirected weighted graph/network between the neurons. The weight of each connection was equal to the total correlation between each pair of neurons.

We followed the same procedure for total correlations 3.3.2, spike count correlations, and signal correlations 3.3.3.

##### Rectified correlations

At the time of writing, the community detection method outlined in (Humphries et al., 2019) could only be applied to networks with positively weighted connections. But many neuron pairs were negatively correlated. To apply the community detection method, we *rectified* the network, by setting all the negative weights to zero.

We also looked for structure in the network created by negative correlations by reversing the signs of the correlations, and rectifying these correlations before applying our network analysis.

Finally, we used the absolute value of the correlations as the weights for the graph/network. By doing this, we hoped to identify both correlated and anti-correlated functional communities of neurons.

##### Sparsifying data networks

When creating our correlation networks, we wanted to exclude any correlations that could be judged to exist ‘by chance’. To do this, we measured the 5th and 95th percentile of the shuffled correlations (see section 3.3.2) for the given mouse and time bin width. We then set all the data correlations between these two values to 0. This excluded any ‘chance’ correlations from our network, and created a sparser network. This allowed us to make use of the ‘sparse weighted configuration model’ as described in section 3.3.5.

##### Communities

Given some network represented by an adjacency matrix  $\mathbf{A}$ , a community within that network is defined as a collection of nodes where the number of connections within these nodes

is higher than the expected number of connections between these nodes. In order to quantify the ‘expected’ number of connections, we need a model of expected networks. This is analogous to a ‘null model’ in traditional hypothesis testing. We test the hypothesis that our data network departs from the null network model to a statistically significant degree. For undirected unweighted networks, the canonical model of a null network is the configuration model (Fosdick et al., 2016). Since we are working with weighted sparse networks, we used more suitable null models, described below.

**Weighted configuration model**

The *weighted configuration model* is a canonical null network model for weighted networks. Given some data network, the weighted configuration model null network will preserve the degree sequence and weight sequence of each node in the data network. But the edges will be distributed randomly (Fosdick et al., 2016). Any structure in the data network beyond its degree sequence and weight sequence will not be captured in the weighted configuration model. So, this model can be used in testing the hypothesis that this extra structure exists.

**Sparse weighted configuration model**

The *sparse weighted configuration model* is another null network model. Similar in nature to the weighted configuration model (see section 3.3.5), but the sparsity of the data network is preserved in the null network. This is achieved by sampling from a probability distribution for the creation or non-creation of each possible connection, then distributing the weight of the data network randomly in this sparse network (Humphries et al., 2019). This is the null network that we used when searching for additional structure in our data networks.

**Spectral rejection**

We made use of the spectral rejection algorithm as outlined in (Humphries et al., 2019). The spectral rejection algorithm is a method for finding structure in a network not captured by a supposed null model, if such structure exists.

To describe the method, we denote our data network matrix  $\mathbf{W}$ , we denote the expected network of our null network model as  $\langle \mathbf{P} \rangle$ . Then the departure of our data network from the null network can be described by the matrix

$$\mathbf{B} = \mathbf{W} - \langle \mathbf{P} \rangle \quad (3.24)$$

### 3.3. Methods

---

1454 a common choice for  $\langle \mathbf{P} \rangle$  in community detection is the ‘configuration model’ (Fosdick et  
1455 al., 2016; Humphries, 2011). The matrix  $\mathbf{B}$  is often called the configuration matrix, in this  
1456 context we will use the term ‘deviation matrix’ as it captures the deviation of  $\mathbf{W}$  from the  
1457 null model.

1458 To test for structure in the network represented by  $\mathbf{W}$ , we examine the eigenspectrum of  $\mathbf{B}$   
1459 and compare it to the eigenspectrum of our null model. Firstly, note that since our data model  
1460 doesn’t allow self loops, and is not directed, the matrix representing the network will be  
1461 symmetric and positive semi-definite, and will therefore be invertible with real eigenvalues.  
1462 We selected a null model with the same characteristics.

1463 To find the eigenspectrum of the null model, we generated  $N$  samples from our null  
1464 model  $P_1, \dots, P_N$ , and we measured their deviation matrices  $B_1, \dots, B_N$ . We then calculated  
1465 the eigenspectrum of each of those samples. We calculated the upper bound of the null model  
1466 eigenspectrum by taking the mean of the largest eigenvalues of  $B_1, \dots, B_N$ . We calculated a  
1467 lower bound on the null model eigenspectrum by taking the mean of the smallest eigenvalues  
1468 of  $B_1, \dots, B_N$ .

1469 We then calculated the eigenspectrum of  $\mathbf{B}$ , our data network deviation matrix. If any of  
1470 those eigenvalues lay outside of the upper or lower bounds of the null model eigenspectrum,  
1471 this is evidence of additional structure not captured by the null model. If we chose the sparse  
1472 weighted configuration model (see section 3.3.5) as our null network model, then eigenvalues  
1473 lying below the lower bound indicate  $k$ -partite structure in the network. For example, if one  
1474 eigenvalue lay below the lower bound, this would indicate some bipartite structure in the data  
1475 network. If any eigenvalues lay above the upper bound of the null model eigenspectrum, this  
1476 is evidence of community structure in the data network. For example, one eigenvalue of  $\mathbf{B}$   
1477 lying above the upper bound of the null model eigenspectrum indicates the presence of two  
1478 communities in the network (Humphries, 2011).

#### 1479 Node rejection

1480 If there are  $d$  data eigenvalues lying outside of the null network eigenspectrum, the  $d$  eigen-  
1481 vectors corresponding to these eigenvalues will form a vector space. If we project the nodes  
1482 of our network into this vector space, by projecting either rows or columns of the data ma-  
1483 trix, we can see how strongly each node contributes to the vector space. Nodes that contribute  
1484 strongly to the additional structure will project far away from the origin, nodes that do not  
1485 contribute to the additional structure will project close to the origin. We want to use this  
1486 information to discard those nodes that do not contribute.

1487 We can test whether a node projects *far* away from the origin or *close* to the origin  
 1488 using the eigenvalues and eigenvectors of  $B_1, \dots, B_N$ . The  $j$ th eigenvector and eigenvalue  
 1489 of  $B_i$  gives a value for a null network's projection into the  $j$ th dimension of the additional  
 1490 structure vector space. The matrices  $B_1, \dots, B_N$  give  $N$  projections into that dimension.  
 1491 These projections are a distribution of the null networks' projections. If the data node's  
 1492 projection exceeds that of the null network projections this node is judged to project *far* from  
 1493 the origin, and therefore contribute to the additional structure. Otherwise, the node is judged  
 1494 to project *close* to the origin, and is therefore rejected (Humphries et al., 2019).

1495 **Community detection**

1496 Another application for this  $d$  dimensional space is community detection. We first project  
 1497 all of the nodes into this  $d$ -dimensional space, then perform the clustering in this space. The  
 1498 clustering and community detection procedure is described in (Humphries, 2011).

1499 In practice, the procedure is carried out  $n$  times (we chose  $n = 100$  times), this returns  $n$   
 1500 clusterings. We resolve these  $n$  clusterings to one final clustering using *consensus clustering*.  
 1501 We used the consensus clustering method that uses an explicit null model for the consensus  
 1502 matrix, as outlined in (Humphries et al., 2019).

1503 **3.3.6 Clustering Comparison**

A clustering  $\mathcal{C}$  is a partition of a set  $D$  into sets  $C_1, C_2, \dots, C_K$ , called clusters, that satisfy the following for all  $k, l \in \{1, \dots, K\}$ :

$$C_k \cap C_l = \emptyset \quad (3.25)$$

$$\bigcup_{k=1}^K C_k = D \quad (3.26)$$

1504 If we consider two clusterings,  $\mathcal{C}$  with clusters  $C_1, C_2, \dots, C_K$  and  $\mathcal{C}'$  with clusters  
 1505  $C'_1, C'_2, \dots, C'_K$ . There are a number of measurements we can use to compare  $\mathcal{C}$  and  $\mathcal{C}'$ . In  
 1506 the following, the number of elements in  $D$  is denoted by  $n$ , and the number of elements in  
 1507 cluster  $C_k$  is  $n_k$ .

1508 **Adjusted Rand Index**

1509 The *adjusted Rand Index* is a normalised similarity measure for clusterings based on pair  
 1510 counting.

### 3.3. Methods

---

If we consider the clusterings  $\mathcal{C}$  and  $\mathcal{C}'$ , and denote

- the number of pairs in the same cluster in  $\mathcal{C}$  and  $\mathcal{C}'$  by  $N_{11}$

- the number of pairs in different clusters in  $\mathcal{C}$  and  $\mathcal{C}'$  by  $N_{00}$

- the number of pairs in the same cluster in  $\mathcal{C}$  and different clusters in  $\mathcal{C}'$  by  $N_{10}$

- the number of pairs in different clusters in  $\mathcal{C}$  and the same cluster in  $\mathcal{C}'$  by  $N_{01}$

then the *Rand Index* is defined as

$$RI = \frac{N_{11} + N_{00}}{N_{11} + N_{00} + N_{10} + N_{01}} = \frac{N_{11} + N_{00}}{\binom{n}{2}} \quad (3.27)$$

The Rand Index is 1 when the clusterings are identical, and 0 when the clusterings are com-

pletely different.

The *adjusted Rand Index* intends on correcting the Rand Index for chance matching pairs.

This is defined as

$$ARI = \frac{2(N_{00}N_{11} - N_{01}N_{10})}{(N_{00} + N_{01})(N_{01} + N_{11}) + (N_{00} + N_{10})(N_{10} + N_{11})} \quad (3.28)$$

The adjusted Rand Index is 1 when the clusterings are identical, and 0 when the Rand Index

is equal to its expected value.

#### 1520 Clusterings as random variables

If we take any random element of  $D$ , the probability that this element is in cluster  $C_k$  of clustering  $\mathcal{C}$  is

$$P(K = k) = \frac{n_k}{n} \quad (3.29)$$

this defines a probability distribution, which makes the clustering a random variable. Any

clustering can be considered as a random variable this way.

This means that we can measure any of the information theoretic quantities defined in section 3.3.4 with respect to clusterings. For example, the entropy of a clustering is

$$H(\mathcal{C}) = - \sum_{k=1}^K \frac{n_k}{n} \log \frac{n_k}{n} \quad (3.30)$$

If we have two clusterings, the joint probability distribution of these clusterings is defined as

$$P(K = k, K' = k') = \frac{|C_k \cap C'_{k'}|}{n} \quad (3.31)$$

- 1523 The joint distribution allows us to define the mutual information between two clusterings,  
1524  $I(\mathcal{C}; \mathcal{C}')$  (Meilă, 2007).

1525 **Information based similarity measures**

The mutual information between two clusterings is a similarity measure, with  $I(\mathcal{C}; \mathcal{C}') = 0$  if  $\mathcal{C}$  and  $\mathcal{C}'$  are completely different, and  $I(\mathcal{C}; \mathcal{C}') = H(\mathcal{C}) = H(\mathcal{C}')$  if  $\mathcal{C}$  and  $\mathcal{C}'$  are identical. This can be normalised in a number of different ways to make more similarity measures (Vinh, Epps, and Bailey, 2010)

$$NMI_{joint} = \frac{I(\mathcal{C}; \mathcal{C}')}{H(\mathcal{C}, \mathcal{C}')} \quad (3.32)$$

$$NMI_{max} = \frac{I(\mathcal{C}; \mathcal{C}')}{\max\{H(\mathcal{C}), H(\mathcal{C}')\}} \quad (3.33)$$

$$NMI_{sum} = \frac{2I(\mathcal{C}; \mathcal{C}')}{H(\mathcal{C}) + H(\mathcal{C}')} \quad (3.34)$$

$$NMI_{sqrt} = \frac{I(\mathcal{C}; \mathcal{C}')}{\sqrt{H(\mathcal{C})H(\mathcal{C}')}} \quad (3.35)$$

$$NMI_{min} = \frac{I(\mathcal{C}; \mathcal{C}')}{\min\{H(\mathcal{C}), H(\mathcal{C}')\}} \quad (3.36)$$

We can control for chance similarities between the two clusterings by measuring the *adjusted mutual information* between the clusterings. This is defined as

$$AMI_{sum} = \frac{I(\mathcal{C}; \mathcal{C}') - E\{I(\mathcal{C}; \mathcal{C}')\}}{\frac{1}{2}[H(\mathcal{C}) + H(\mathcal{C}')] - E\{I(\mathcal{C}; \mathcal{C}')\}} \quad (3.37)$$

- 1526 The first term in the denominator, taking the average of the marginal entropies, can be re-  
1527 placed by taking the maximum, minimum, or the geometric mean (Vinh, Epps, and Bailey,  
1528 2010).

### 3.3. Methods

---

#### 1529 Information based metrics

The variation of information between two clusterings  $VI(\mathcal{C}; \mathcal{C}')$  (see section 3.3.4) is a metric on the space of clusterings (Meilă, 2007). That is,

$$VI(\mathcal{C}; \mathcal{C}') \geq 0 \quad (3.38)$$

$$VI(\mathcal{C}; \mathcal{C}') = 0 \iff \mathcal{C} = \mathcal{C}' \quad (3.39)$$

$$VI(\mathcal{C}; \mathcal{C}') = VI(\mathcal{C}'; \mathcal{C}) \quad (3.40)$$

$$VI(\mathcal{C}; \mathcal{C}'') \leq VI(\mathcal{C}; \mathcal{C}') + VI(\mathcal{C}'; \mathcal{C}'') \quad (3.41)$$

Another metric is the *information distance* (Vinh, Epps, and Bailey, 2010)

$$D_{max} = \max\{H(\mathcal{C}), H(\mathcal{C}')\} - I(\mathcal{C}; \mathcal{C}') \quad (3.42)$$

Both of these can be normalised

$$NVI(\mathcal{C}; \mathcal{C}') = 1 - \frac{I(\mathcal{C}; \mathcal{C}')}{H(\mathcal{C}, \mathcal{C}')} \quad (3.43)$$

$$d_{max} = 1 - \frac{I(\mathcal{C}; \mathcal{C}')}{\max\{H(\mathcal{C}), H(\mathcal{C}')\}} \quad (3.44)$$

#### 1530 Comparing detected communities and anatomical divisions

In order to quantify the difference or similarity between the communities detected in our correlation network and the anatomical classification of the cells in that network, we considered the communities and the anatomical regions as clusters in two different clusterings,  $\mathcal{C}_{comm}$  and  $\mathcal{C}_{anat}$ , respectively. We then measured the similarity between the clusterings using the mutual information, the adjusted mutual information, and the normalised mutual information. We measured the difference between, or the distance between, the clusterings using the variation of information, the normalised variation of information, and the normalised information distance. We also measured the difference between the clusterings using the adjusted Rand Index, just to use a non-information based measure.

We took all of these measures for communities detected using different time bin widths.

This gave us an idea of the effect of time bin width on correlation networks in neural ensembles relative to anatomical regions within those ensembles.

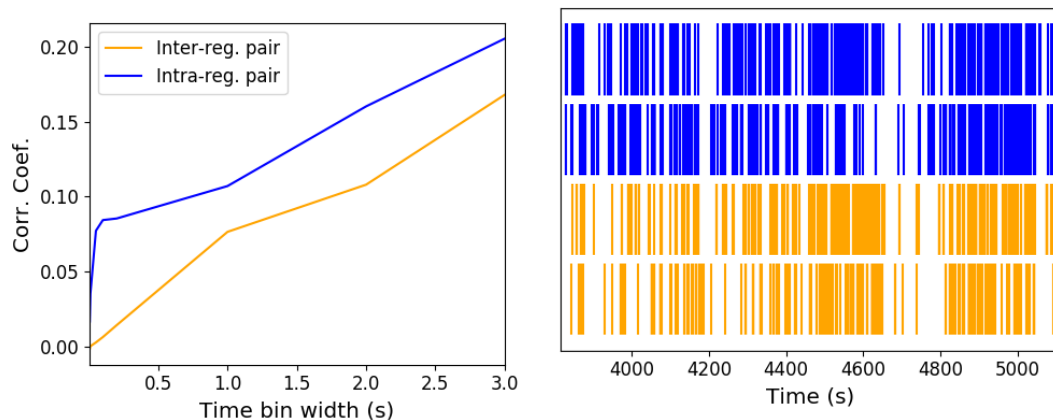
1543 **3.4 Results**

1544 Note that in the following text, we refer to the correlation coefficient between two sequences  
 1545 of spike counts from two different cells as the *total correlation*. We refer to the correlation  
 1546 between spike counts in response to a certain stimulus as the *spike count correlation* aka  
 1547 *noise correlation*, and we refer to the correlation between mean or expected responses to  
 1548 different stimuli as the *signal correlation* (Cohen and Kohn, 2011).

1549 The nine different brain regions from which we had data were the caudate putamen (CP),  
 1550 frontal motor cortex (FrMoCtx), hippocampus (HPF), lateral septum (LS), midbrain (MB),  
 1551 primary visual cortex (V1), superior colliculus (SC), somatomotor cortex (SomMoCtx), and  
 1552 thalamus (TH).

1553 **3.4.1 Average correlation size increases with increasing time bin width**

1554 First we inspected the affect of time bin width on total correlations. We know that using short  
 1555 time bins results in artificially small correlation measurements (Cohen and Kohn, 2011), so  
 1556 we expected to see an increase in correlation amplitude with increasing time bin width. That  
 1557 is exactly what we observed. Taking 50 cells at random, we calculated the total correla-  
 1558 tion between every possible pair of these cells, using different time bin widths ranging from  
 1559 0.005s to 3s. We found that the longer the time bin width, the greater the correlations (see  
 1560 figure 3.4a).



(A) Correlation coefficient as a function of bin width. (B) Raster plots for the four cells making up our example pairs.

FIGURE 3.3: (A) An example of the correlation coefficients between two different pairs of cells, one where both cells are in the same brain region (intra-regional pair), and one where both cells are in different brain regions (inter-regional pair). The correlation coefficients have been measured using different time bin widths, ranging from 5ms to 3s. Note the increasing amplitude of the correlations with increasing bin width. (B) A raster plot showing the spike times of each pair of cells.

### 3.4. Results

---

1561 We also separated the positively correlated pairs from the negatively correlated pairs  
1562 using the mean correlation of each pair across all bin widths (see section 3.3.2). We found  
1563 that the positively correlated pairs become more positively correlated with increasing time bin  
1564 width, and the negatively correlated pairs become more negatively correlated with increasing  
1565 time bin width (see figures 3.4b and 3.4c).

1566 In figure 3.3a we plot correlations from two example pairs, one pair from within a region,  
1567 and one pair between regions. It can be seen that the correlation coefficient increases with  
1568 bin width. The correlations can be observed by eye in the raster plot for these cells in figure  
1569 3.3b.

1570 When taking the mean across all pairs, the positively correlated pairs dominate in terms  
1571 of both number of pairs, and amplitude of correlations. Therefore the mean across all pairs  
1572 is positive.

1573 These results were observed in each of the three mouse subjects from which we had data.

#### 1574 3.4.2 Goodness-of-fit for Poisson and Gaussian distributions across increasing 1575 time bin widths

1576 We wanted to investigate if the width of the time bin used to bin spike times into spike counts  
1577 had an effect on the distribution of spike counts. We used the  $\chi^2$  statistic as a goodness-of-fit  
1578 measure for Poisson and Gaussian (normal) distributions to the spike count of 100 randomly  
1579 chosen neurons for a number of bin widths ranging from 0.01s to 4s. For the  $\chi^2$  statistic, the  
1580 higher the value, the worse the fit.

1581 We expected a Poisson distribution to be a better fit for shorter time bin widths because  
1582 spike counts must be non-negative, therefore any distribution of spike counts with mass dis-  
1583 tributed at or close to 0 will be skewed. The distribution of spike counts is more likely to be  
1584 distributed close to 0 when the time bin widths used to bin spike times into spike counts are  
1585 small relative to the amount of time it takes for a neuron to fire an action potential ( $\sim 1\text{ms}$  in  
1586 the case of non-burst firing neurons).

1587 We expected a Gaussian distribution to be a better fit for longer time bin widths, because  
1588 a Poisson distribution with a large rate is well approximated by a Gaussian distribution with  
1589 mean and variance equal to the Poisson rate. Therefore, a Gaussian distribution would ap-  
1590 proximate the mean of a collection of large spike counts, and have more flexibility than a  
1591 Poisson distribution to fit the variance.

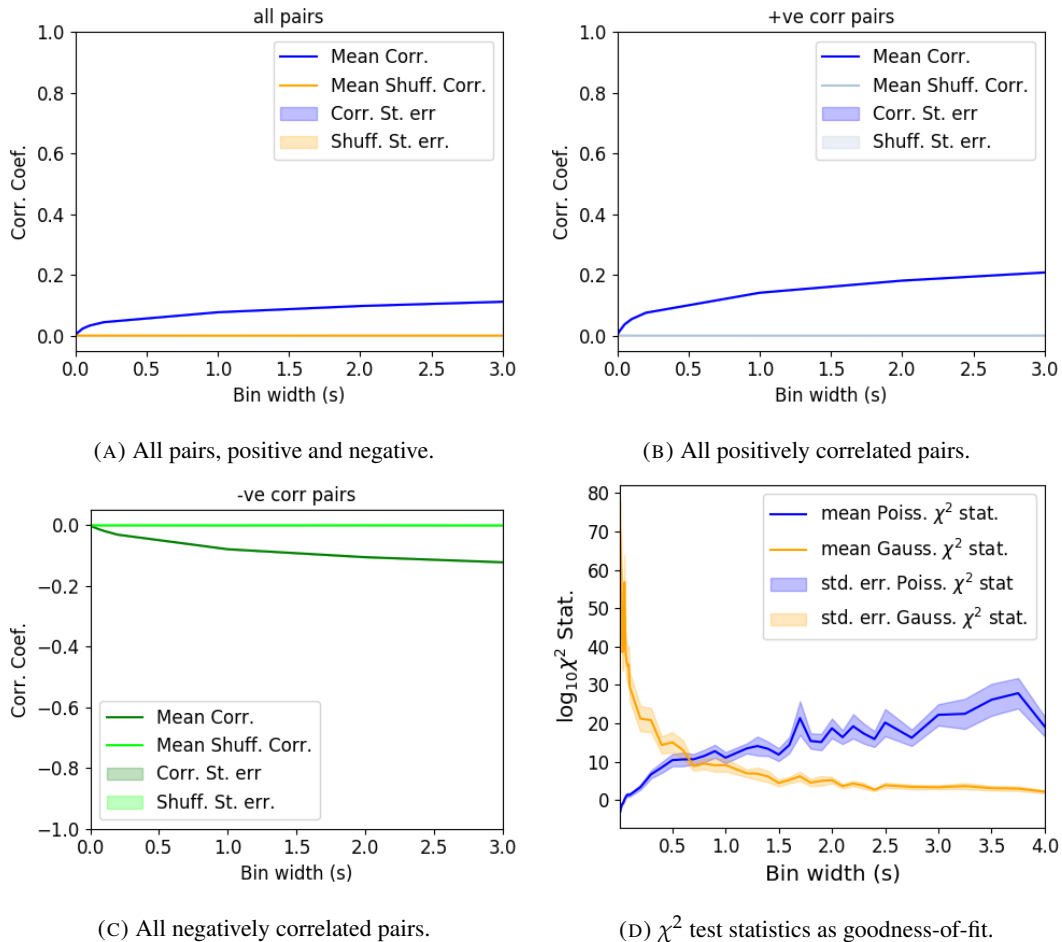


FIGURE 3.4: Mean correlation coefficients measured from pairs of 50 randomly chosen neurons. (A) All possible pairs, (B) positively correlated pairs, and (C) negatively correlated pairs. (D) Mean and standard error of  $\chi^2$  test statistics for Poisson and Gaussian distributions fitted to neuron spike counts.

### 3.4. Results

---

1592 We found that that a Poisson distribution is the best fit for shorter time bins less than 0.7s  
1593 in length. Then a Gaussian distribution is a better fit for time bins greater than 0.7s in length  
1594 (see figure 3.4d).

#### 1595 3.4.3 Differences between and inter- and intra- regional correlations decrease 1596 with increasing bin width

1597 We investigated the differences in distribution between inter-regional correlations, i.e. corre-  
1598 lations between neurons in different brain regions, and intra-regional correlations, i.e. corre-  
1599 lations between neurons in the same brain region.

1600 Firstly, we investigated these quantities for all possible pairs of  $\sim 500$  neurons taken  
1601 from across all the 9 brain regions from which we had data. We distributed these neurons as  
1602 evenly as possible across all of the regions, so that cells from one region would not dominate  
1603 our data. We observed that the mean intra-regional correlations were always higher than the  
1604 mean inter-regional correlations for every value of time bin width used. We also observed  
1605 that as the time bin width increased these mean correlations increased and the difference  
1606 between the mean inter-regional and intra-regional correlations grew (see figure 3.5 (Left)).

1607 Stringer et al. (2019) had a similar finding using the same data. They used only one value  
1608 for the time bin width, 1.2s. Using this time bin width to bin spike times and measure total  
1609 correlations, they found that the mean ‘within-region’ correlations were always greater than  
1610 the ‘out-of-region’ correlations (Stringer et al., 2019). The figure from their paper showing  
1611 this result can be seen in figure 3.5 (Right).

1612 Examples of the correlations of one intra-regional pair and one inter-regional pair can be  
1613 seen in figure 3.3.

1614 Secondly, we separated those pairs into intra-regional and inter-regional groups. We  
1615 noted that the mean intra-regional correlations (coloured dots in figures 3.6a and 3.6b) for  
1616 a given region tended to be higher than the mean inter-regional correlations (black dots in  
1617 figures 3.6a and 3.6b) involving cells from that region. However, in contrast with our previous  
1618 result, we noted that the difference between the mean intra-regional correlations and most  
1619 highly correlated inter-regional correlations reduced as we increased the time bin width (see  
1620 figures 3.6a and 3.6b). This shows that the mean correlations showin in figure 3.5 are not  
1621 distributed evenly across all region pair combinations.

1622 Finally, to see these regional mean correlations in a bit more detail, to examine the indi-  
1623 vidual pair combinations in particular, we displayed these data in a matrix of mean corre-  
1624 lations (see figure 3.7), showing the mean intra-regional correlations on the main diagonal, and

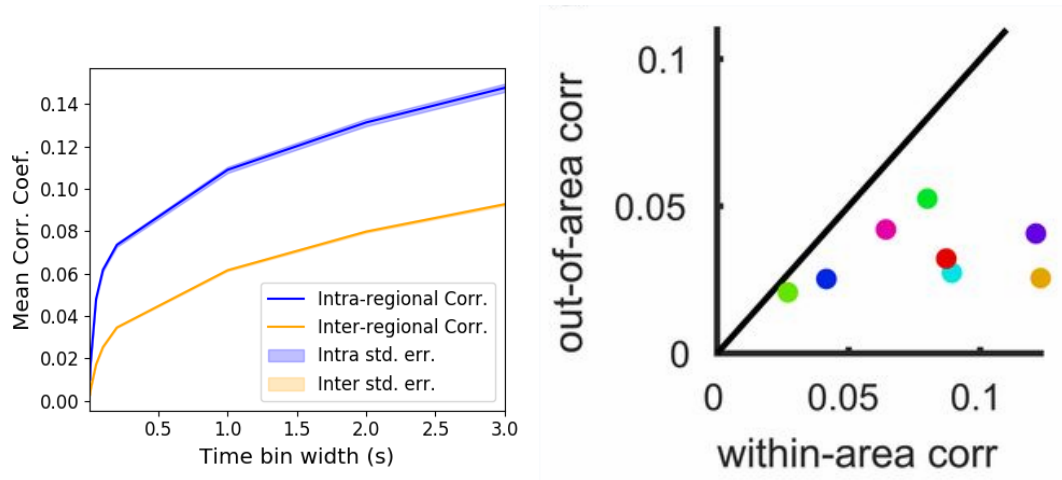


FIGURE 3.5: (Left)The mean intra-region and inter-region correlations using all possible pairs of  $\sim 500$  neurons, spread across 9 different brain regions. (Right) Courtesy of Stringer et al. (2019), mean inter-regional (out-of-area) correlation coefficients vs mean intra-regional (within-area) correlation coefficients for a bin width of 1.2s. Note that the intra-regional coefficients are higher in each case.

1625 the mean inter-regional correlations off diagonal. Comparing a version of this figure created  
 1626 using a short time bin width of 5ms (figure 3.7a) and a version using a longer time bin width  
 1627 of 1s (figure 3.7b) we observed that the mean intra-regional correlations are always relatively  
 1628 high in comparison to the mean inter-regional correlations, but the mean correlations in some  
 1629 inter-regional pairs are relatively much higher when using the longer time bin width.

1630 This could indicate information being processed quickly at a local or within-region level,  
 1631 and the local representations of this information spreading between regions at longer timescales.

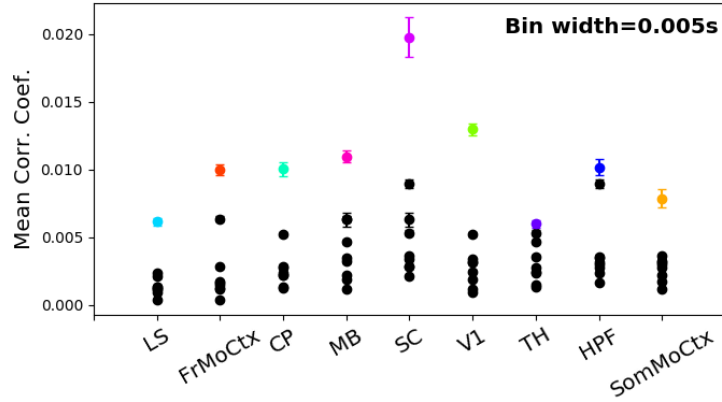
1632 These results were consistent across the three mouse subjects. But, the relative magni-  
 1633 tudes of the mean intra-regional and inter-regional correlations were not consistent. For ex-  
 1634 ample, the region with the highest mean intra-regional correlations when using 1s bin widths  
 1635 for subject one is the superior colliculus (SC), but for subject two it is the midbrain (MB).

### 1636 3.4.4 Connected and divided structure in correlation based networks reduces 1637 in dimension with increasing bin width

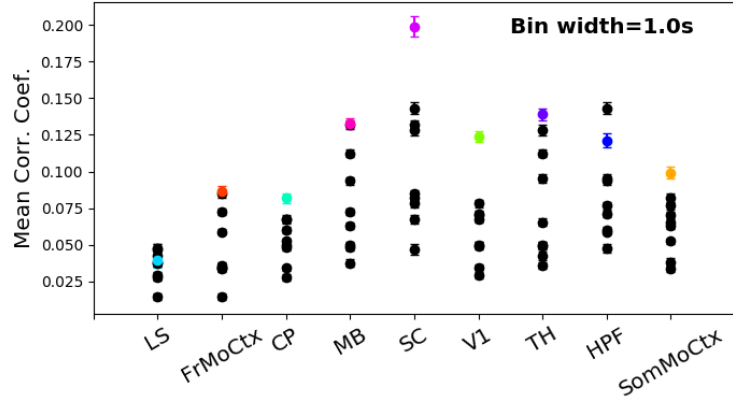
1638 We used the correlation measurements to create weighted undirected graphs/networks where  
 1639 each node represents a neuron, and the weight of each edge is the pairwise correlation be-  
 1640 tween those neurons represented by the nodes at either end of that edge. We aimed to find  
 1641 communities of neurons within these networks, and compare the structure of these commu-  
 1642 nities to the anatomical division of those neurons. The first step of this process involved  
 1643 applying the ‘spectral rejection’ technique developed by Humphries et al (2019) (Humphries

### 3.4. Results

---

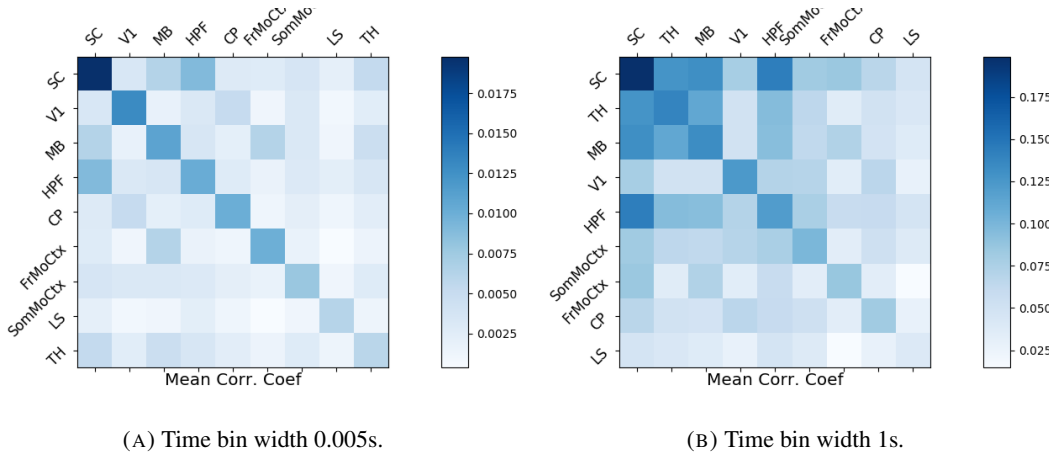


(A) Mean inter-regional and intra-regional correlations using a time bin width of 5ms.



(B) Mean inter-regional and intra-regional correlations using a time bin width of 1s.

FIGURE 3.6: The mean intra-regional correlations (coloured dots) and mean inter-regional correlations (black dots) for a given region, indicated on the x-axis, for different time bin widths. Each black dot represents the mean inter-regional correlations between the region indicated on the x-axis and one other region. (A) shows these measurements when we used a time bin width of 5ms. (B) shows these measurements when we used a time bin width of 1s. Note that the difference between the mean inter-regional correlations and mean intra-regional correlations is smaller for 1s bins.



(A) Time bin width 0.005s.

(B) Time bin width 1s.

FIGURE 3.7: Mean inter-regional (main diagonal) and intra-regional (off diagonal) correlation coefficients. (A) Shows these measurements when spike times were binned using 5ms time bins. (B) Shows the same, using 1s time bins. Note that the matrices are ordered according to the main diagonal values, therefore the ordering is different in each subfigure.

et al., 2019). This technique compares our data network to a chosen null network model, and finds any additional structure in the data network beyond that which is captured in the null network model (if there is any such structure).

By comparing the eigenspectrum of the data network to the eigenspectrum of many samples from the null network model, this technique allows us to estimate the dimensionality of the additional structure in the data network, and gives us a basis for that vector space. It also divides the additional structure into connected structure, and  $k$ -partite (or divided) structure. For example, if our algorithm found two dimensions of additional connected structure, and one dimension of additional divided structure. We might expect to find three communities, that is groups more strongly connected within group than without, and we might expect to find bi-partite structure, that is two sets that are more strongly connected between groups than within groups.

The technique also finds which nodes contribute to this additional structure, and divides our data network into signal and noise networks. The details of spectral rejection and node rejection can be found in sections 3.3.5 and 3.3.5 respectively, and a full overview can be found in (Humphries et al., 2019).

We chose the sparse weighted configuration model (see section 3.3.5) as our null network model. This model matches the sparsity and the total weight of the original network but distributes the weight at random across the sparse network.

We applied the spectral rejection method to our networks based on total correlations using different values for the time bin width. We observed that for smaller time bin widths, our data

### 3.4. Results

---

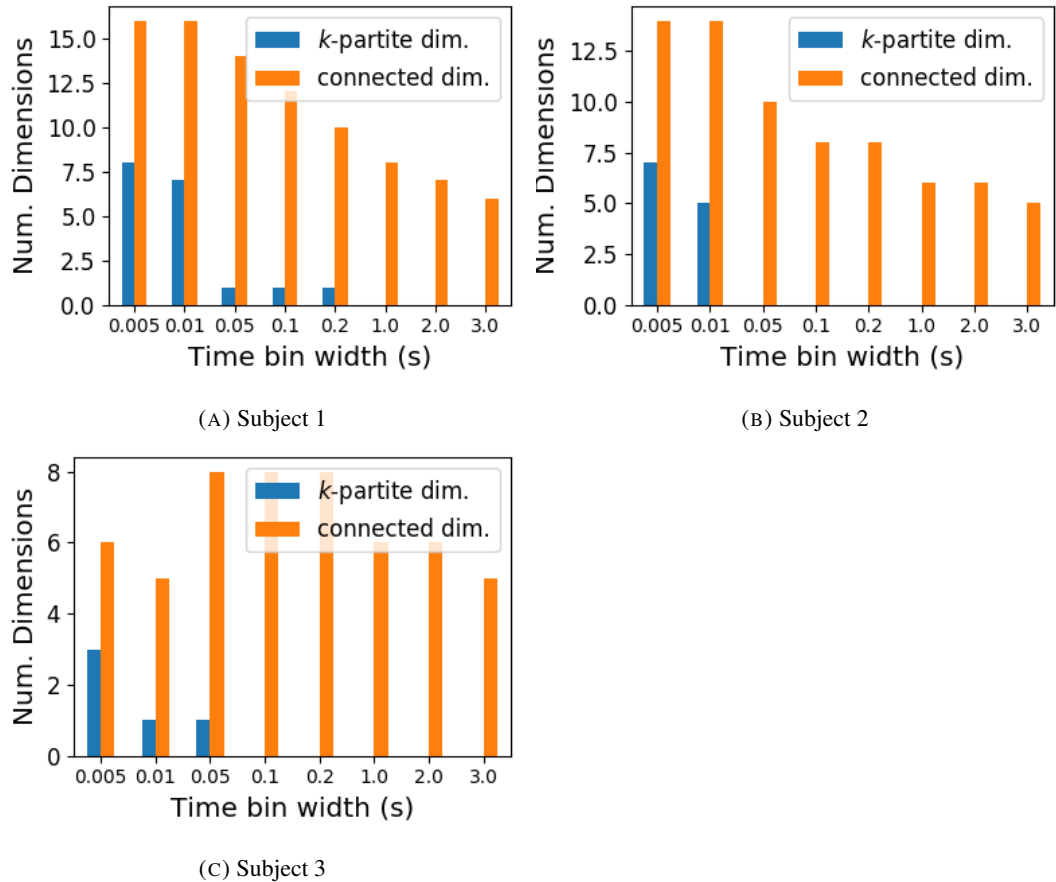


FIGURE 3.8: The number of dimensions in the *k*-partite and connected structure in the correlation based networks beyond the structure captured by a sparse weighted configuration null network model (see section 3.3.5), shown for different time bin widths. Note that the *k*-partite structure disappears for time bin width greater than 200ms for all three subjects. The dimension of the connected structure reduces with increasing bin width for 2 of the 3 subjects (top row).

networks had both  $k$ -partite structure, and community structure. As the width of the time bin increased, we found that the  $k$ -partite structure disappeared from our data networks, and the dimension of the community structure reduced in two of the three mice from which we had data (see figure 3.8).

### 3.4.5 Detecting communities in correlation based networks

We applied the community detection procedure described in section 3.3.5 to our signal networks for our various time bin widths. We detected a greater number of smaller communities at shorter time bin widths, and a smaller number of larger communities for longer time bin widths (see figure 3.9). This was expected after the results found in section 3.4.4. We found more dimensions of additional structure at shorter time bin widths, therefore we found more communities at shorter time bin widths.

We also noticed that at short time bin widths the communities detected tended to be dominated by cells from one region. Whereas communities existing in networks created using wider time bin widths tended to contain cells from many different brain regions. More on this in the next section.

### 3.4.6 Functional communities resemble anatomical division at short timescales

In order to quantify the similarity of the communities detected to the anatomical division of the cells. We treated both the anatomical division and the communities as clusterings of these cells. We then used measures for quantifying the difference or similarity between clusterings to quantify the difference or similarity between the detected communities and the anatomical division. Details of these measures can be found in section 3.3.6 or in (Vinh, Epps, and Bailey, 2010).

We used two different types of measures for clustering comparison; information based measures (see section 3.3.6) and pair counting based measures (see section 3.3.6). We include one example of each in figure 3.10.

The variation of information is the information based measure included in figure 3.10a. This measure forms a metric on the space of clusterings. The larger the value for the variation of information, the more different the clusterings.

The adjusted Rand index is the pair counting based measure included in figure 3.10b. In contrast with the variation of information, the adjusted Rand index is a normalised similarity measure. The adjusted Rand index takes value 1 when the clusterings are identical, and takes value 0 when the clusterings are no more similar than chance.

### 3.4. Results

---

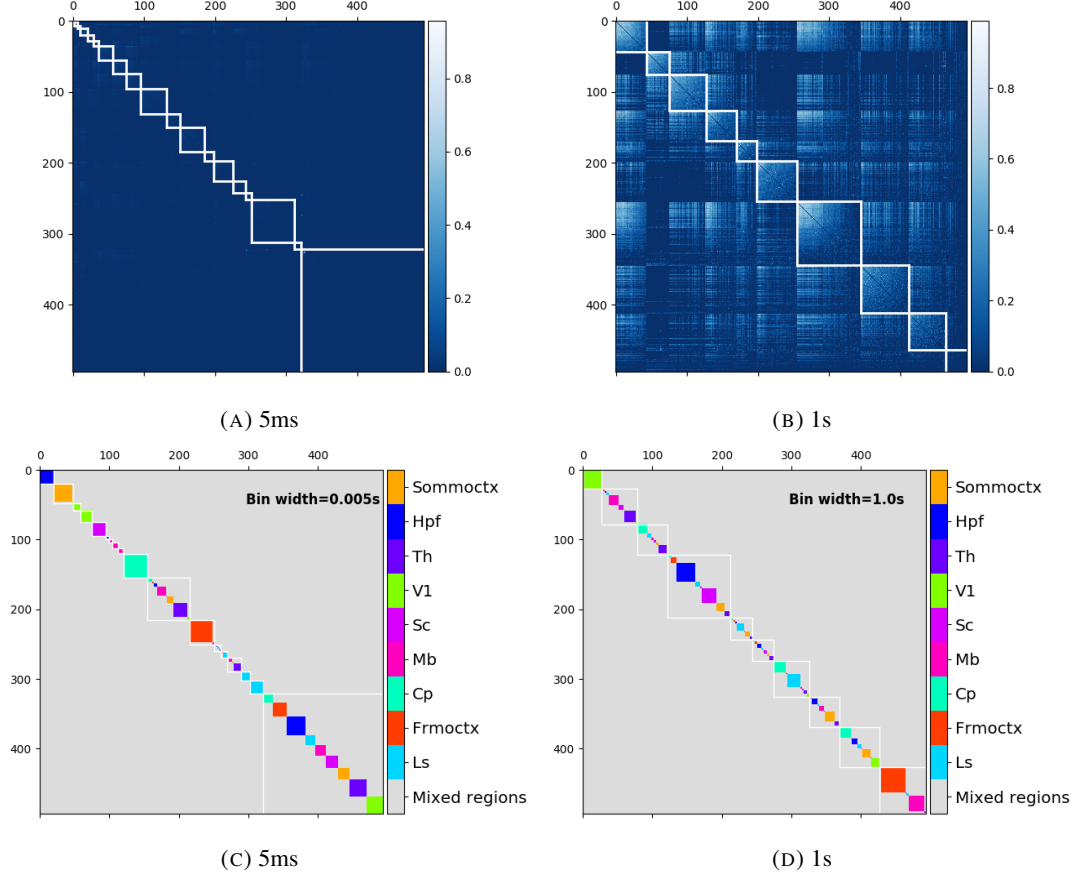
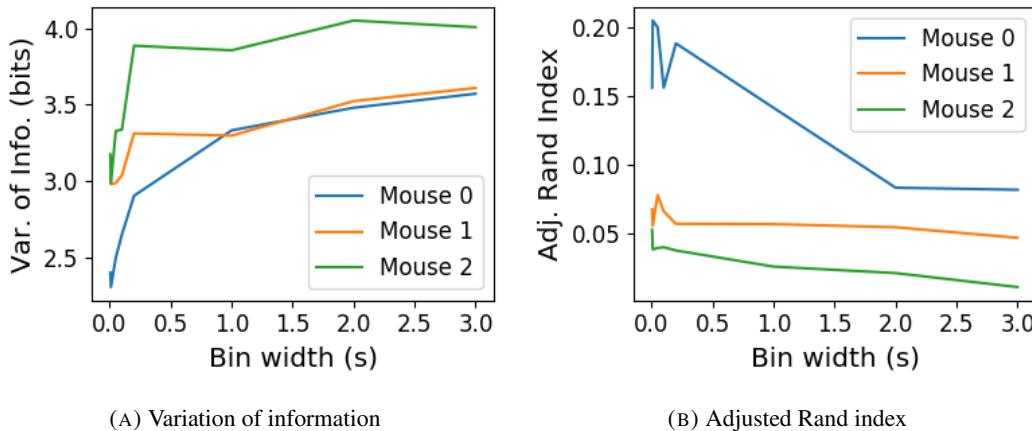


FIGURE 3.9: (A-B) Correlation matrices with detected communities indicated by white lines. Each off main diagonal entry in the matrix represents a pair of neurons. Those entries within a white square indicate that both of those neurons are in the same community as detected by our community detection procedure. Matrices shown are for 5ms and 1s time bin widths respectively. Main diagonal entries were set to 0. (C-D) Matrices showing the anatomical distribution of pairs along with their community membership. Entries where both cells are in the same region are given a colour indicated by the colour bar. Entries where cells are in different regions are given the grey colour also indicated by the colour bar.



(A) Variation of information

(B) Adjusted Rand index

FIGURE 3.10: (A) The variation of information is a measure of distance between clusterings. The distance between the anatomical ‘clustering’ and community detection ‘clustering’ increases with increasing time bin width. (B) The adjusted Rand index is a normalised similarity measure between clusterings. The anatomical and community detection clusterings become less similar as the time bin width increases.

1697 Both measures indicated that the detected communities and the anatomical division of  
 1698 the cells were more similar when we used shorter time bins widths (see figure 3.10). This  
 1699 indicates that correlated behaviour in neuronal ensembles is more restricted to individual  
 1700 brain regions at short timescales (< 250ms), and the correlated activity spreads out across  
 1701 brain regions over longer time scales.

### 1702 3.4.7 Conditional correlations & signal correlations

1703 In light of the excellent research of Stringer et al (2019) showing that spontaneous behaviours  
 1704 can drive activity in neuronal ensembles across the visual cortex and midbrain (Stringer et  
 1705 al., 2019), we decided to control for the mouse’s behaviour when performing our analyses.  
 1706 It is possible that our community detection process may be detecting communities across  
 1707 multiple brain regions at longer time scales due to aggregating neuronal activity driven by  
 1708 several spontaneous behaviours occurring during the time interval covered by a given time  
 1709 bin. A time bin of 1s, for example, could contain a spike count where those spikes were driven  
 1710 by different spontaneous behaviours. We aimed to investigate this possibility by applying our  
 1711 community detection analysis to conditional correlation measures.

1712 We used the top 500 principal components of a video of the mouse’s face as a measure of  
 1713 the mouse’s behaviour (see section 3.2.2). We modelled the spike counts as a linear combi-  
 1714 nation of the principal components using linear regression with ElasticNet regularisation (see  
 1715 section 3.3.3). Using this model, we quantified the expected spike count given the mouse’s  
 1716 behaviour  $E[X|Z_1, \dots, Z_{500}]$ .

### 3.4. Results

---

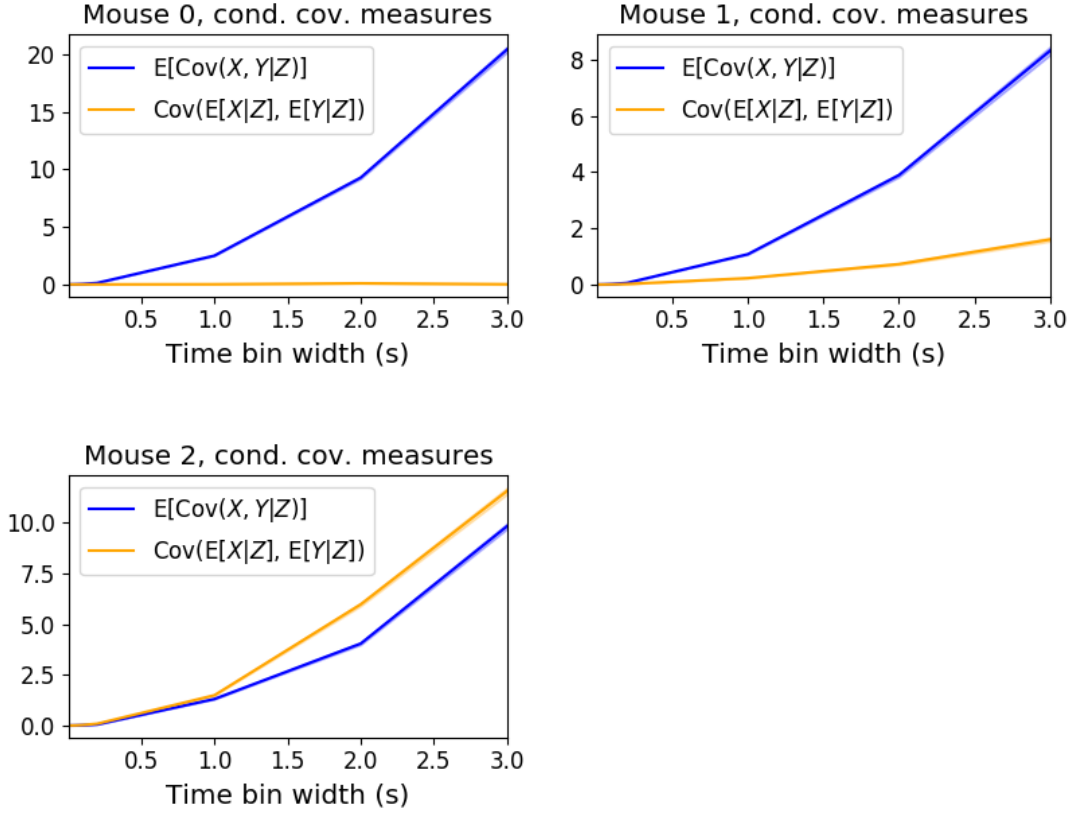


FIGURE 3.11: Comparing the components of the total covariance across different values for the time bin width. We observed a consistent increase in  $E[\text{cov}(X, Y|Z)]$  as the time bin width increased. But we saw different trends for  $\text{cov}(E[X|Z], E[Y|Z])$  for each mouse.

1717        We used these expected values to measure  $\text{cov}(E[X|Z], E[Y|Z])$ , and we used that value,  
 1718        the covariance  $\text{cov}(X, Y)$ , and the *law of total covariance* (see section 3.3.3) to measure  
 1719         $E[\text{cov}(X, Y|Z)]$ . Here  $X$  and  $Y$  represent spike counts from individual cells, and  $Z$  is short-  
 1720        hand for the 500 principal components mentioned above. The two components of the co-  
 1721        variance,  $\text{cov}(E[X|Z], E[Y|Z])$  and  $E[\text{cov}(X, Y|Z)]$ , represent a ‘signal covariance’ and ex-  
 1722        pected value of a ‘spike count covariance’ respectively, analogous to the signal correlation  
 1723        and spike count correlation (Cohen and Kohn, 2011).

1724        We examined the means of these components for different values of the time bin width  
 1725        (see figure 3.11). We observed a consistent increase in  $E[\text{cov}(X, Y|Z)]$  as the time bin width  
 1726        increased. But we saw different trends for  $\text{cov}(E[X|Z], E[Y|Z])$  for each mouse.

1727        Using  $\text{cov}(E[X|Z], E[Y|Z])$  we measured the signal correlation,  $\rho_{\text{signal}}$ , and using  $E[\text{cov}(X, Y|Z)]$   
 1728        we measured the event conditional correlation,  $\rho_{X,Y|Z}$  (see section 3.3.3 for more details).  
 1729        We saw a consistent increase in  $\rho_{X,Y|Z}$  as the time bin width increased, this corresponds to  
 1730        the result for  $E[\text{cov}(X, Y|Z)]$ . We observed different trends for  $\rho_{\text{signal}}$  for each mouse, this

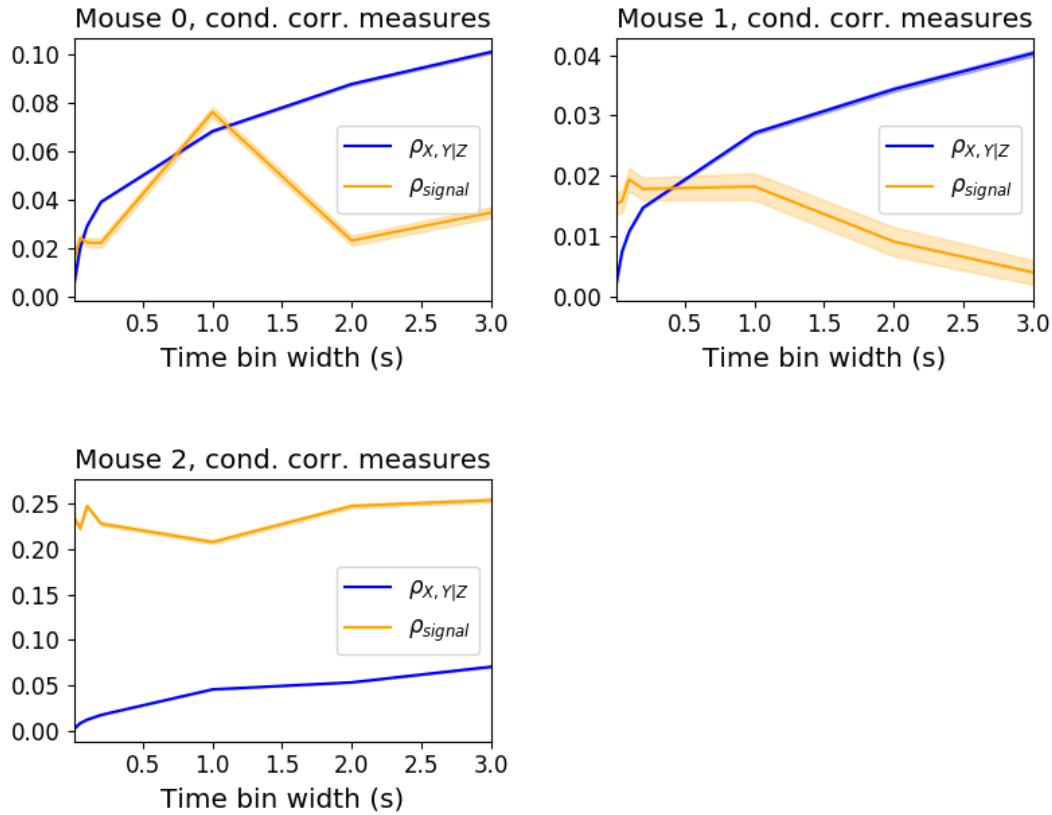


FIGURE 3.12: Comparing the components of the total covariance across different values for the time bin width. We saw a consistent increase in  $\rho_{X,Y|Z}$  as the time bin width increased in all three subjects. But we saw different trends in  $\rho_{\text{signal}}$  for each of the subjects.

1731 corresponds to the result for  $\text{cov}(E[X|Z], E[Y|Z])$ .

1732 We applied our network noise rejection and community detection process to networks  
 1733 based on the spike count correlations  $\rho_{X,Y|Z}$  and the signal correlations  $\rho_{\text{signal}}$ . We noted that  
 1734 the community detection on  $\rho_{X,Y|Z}$  behaved similarly to the community detection on the total  
 1735 correlation. We can see this in figures 3.13a and 3.13b. At very short time bin widths, we  
 1736 detect more communities, and those communities often contain cells from one brain region  
 1737 only. At longer time bin widths, we detect fewer communities, and those communities tend  
 1738 to contain cells from multiple brain regions. When we examine the distance between (or  
 1739 similarity between) the anatomical division of the cells, and the detected communities we  
 1740 notice that the two clusterings are more similar at shorter time bin widths (see figure 3.14).

1741 When we applied the network noise rejection and community detection process to the  
 1742 networks based on the signal correlations  $\rho_{\text{signal}}$  we found the number of communities we  
 1743 detected reduced with increasing time bin width. But the number of communities detected

### 3.4. Results

---

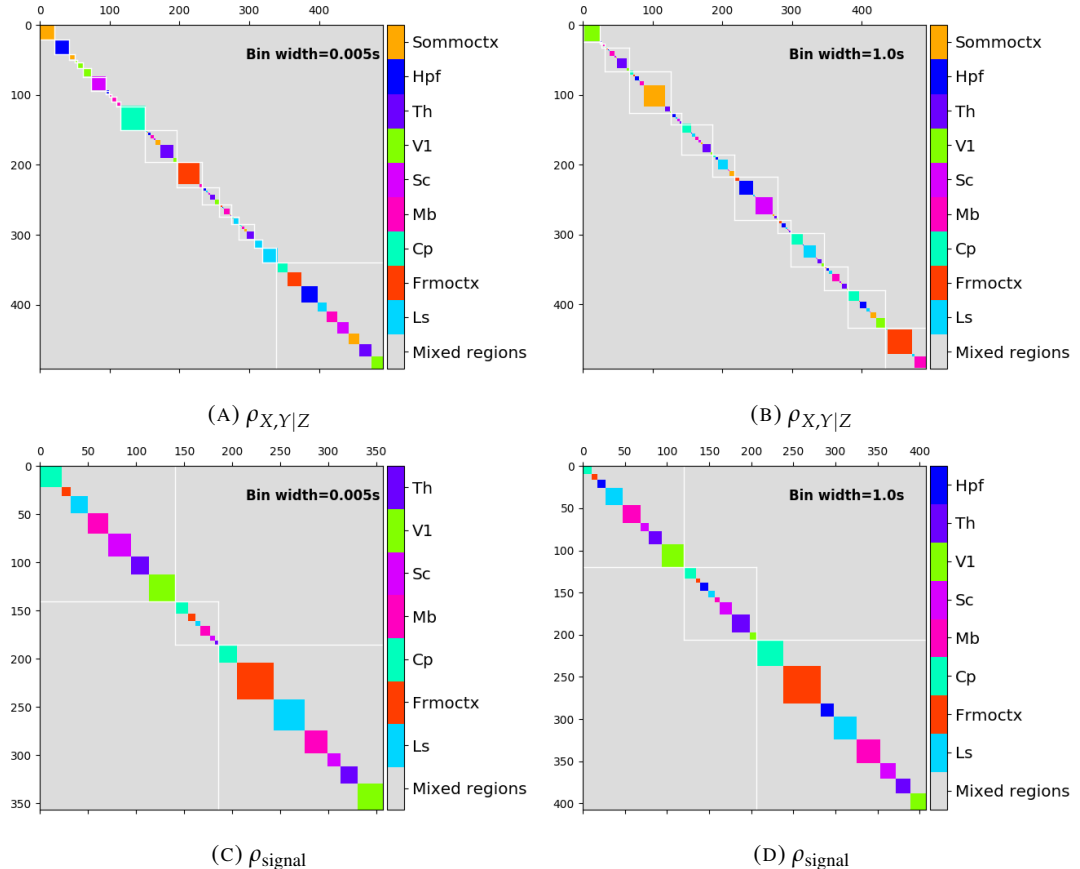


FIGURE 3.13: Matrices showing the regional membership of pairs by colour, and the communities in which those pairs lie. (A-B) Detected communities and regional membership matrix for network based on rectified spike count correlation  $\rho_{X,Y|Z}$ , using time bin widths of 0.005s and 1s respectively. (C-D) Detected communities and regional membership matrix for network based on rectified signal correlation  $\rho_{\text{signal}}$ , using time bin widths of 0.005s and 1s respectively.

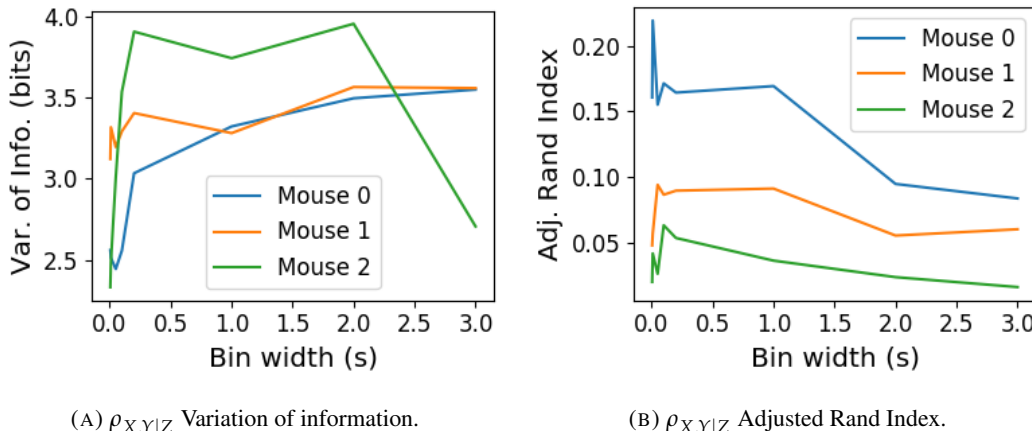
(A)  $\rho_{X,Y|Z}$  Variation of information.(B)  $\rho_{X,Y|Z}$  Adjusted Rand Index.

FIGURE 3.14: Distance and similarity measures between the anatomical division of the neurons, and the communities detected in the network based on the spike count correlations  $\rho_{X,Y|Z}$ . (A) The variation of information is a ‘distance’ measure between clusterings. The distance between the anatomical ‘clustering’ and the community clustering increases as the time bin width increases. (B) The adjusted Rand index is a similarity measure between clusterings. The detected communities become less similar to the anatomical division of the cells as the time bin width increases.

1744 was less than that for the total correlations or the spike count correlations. The commu-  
 1745 nities detected always tended to contain cells from multiple regions at both short and long  
 1746 timescales (see figures 3.13c and 3.13d). The communities detected bore very little relation  
 1747 to the anatomical division of the cells. The adjusted Rand index between the community  
 1748 clustering and the anatomical ‘clustering’ is close to zero for every time bin width (see figure  
 1749 3.15b). This indicates that the similarity between the clusterings is close to chance. We did  
 1750 observe a slight downward trend in the variation of information with increasing bin width  
 1751 (see figure 3.15a), but this is more likely due to a decrease in the number of communities  
 1752 detected rather than any relationship with anatomy.

1753 We also observed that the network noise rejection process rejected some of the cells  
 1754 when applied to the network based on the signal correlations. This means that those cells  
 1755 did not contribute to the additional structure of the network beyond that captured by the  
 1756 sparse weighted configuration model. This is why the matrices in figures 3.13c and 3.13d are  
 1757 smaller than their analogues in figures 3.13a and 3.13b.

### 1758 3.4.8 Absolute correlations and negative rectified correlations

1759 At the moment, the network noise rejection protocol can only be applied to weighted undi-  
 1760 rected graphs with non-negative weights. This meant that we had to rectify our correlated  
 1761 networks before applying the network noise rejection and community detection process. We

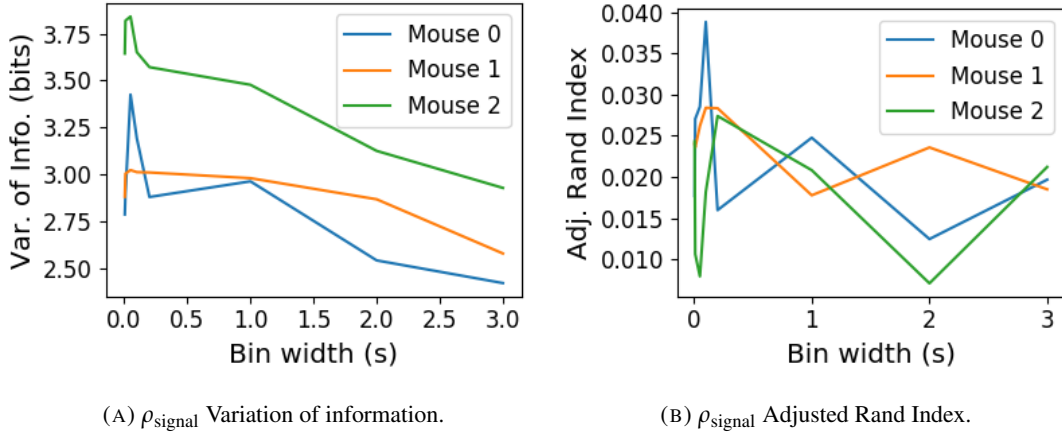


FIGURE 3.15: Distance and similarity measures between the anatomical division of the neurons, and the communities detected in the network based on the signal correlations  $\rho_{\text{signal}}$ . (A) The variation of information is a ‘distance’ measure between clusterings. The distance between the anatomical ‘clustering’ and the community clustering increases as the time bin width increases. (B) The adjusted Rand index is a similarity measure between clusterings. The detected communities become less similar to the anatomical division of the cells as the time bin width increases.

wanted to investigate what would happen if instead of rectifying the correlations, we used the absolute value, or reversed the signs of the correlations and then rectified.

When we used the absolute value of the correlations, we found very similar results to those shown above for the rectified total correlations and the rectified spike count correlations. We detected more communities using shorter bin widths, and these communities were more similar to the brain’s anatomy than those communities detected using a longer bin width (see figure 3.16). The only exception being that we detected more communities. This could indicate that we detected both positively and negatively correlated communities, but we haven’t done any further investigation so we cannot say for sure.

When we used the sign reversed rectified correlated networks, we tended to find fewer communities. Each community contained cells from many different anatomical regions, at both long and short bin widths (see figures 3.17a, 3.17b, 3.17c, 3.17d). The communities bore little relation to the anatomical distribution of the cells, this can be seen in figure 3.17f, the values close to zero indicate that the similarity between the two clusterings are around chance level. This indicates that there was not much structure in the negatively correlated networks beyond that captured by the sparse weighted configuration model.

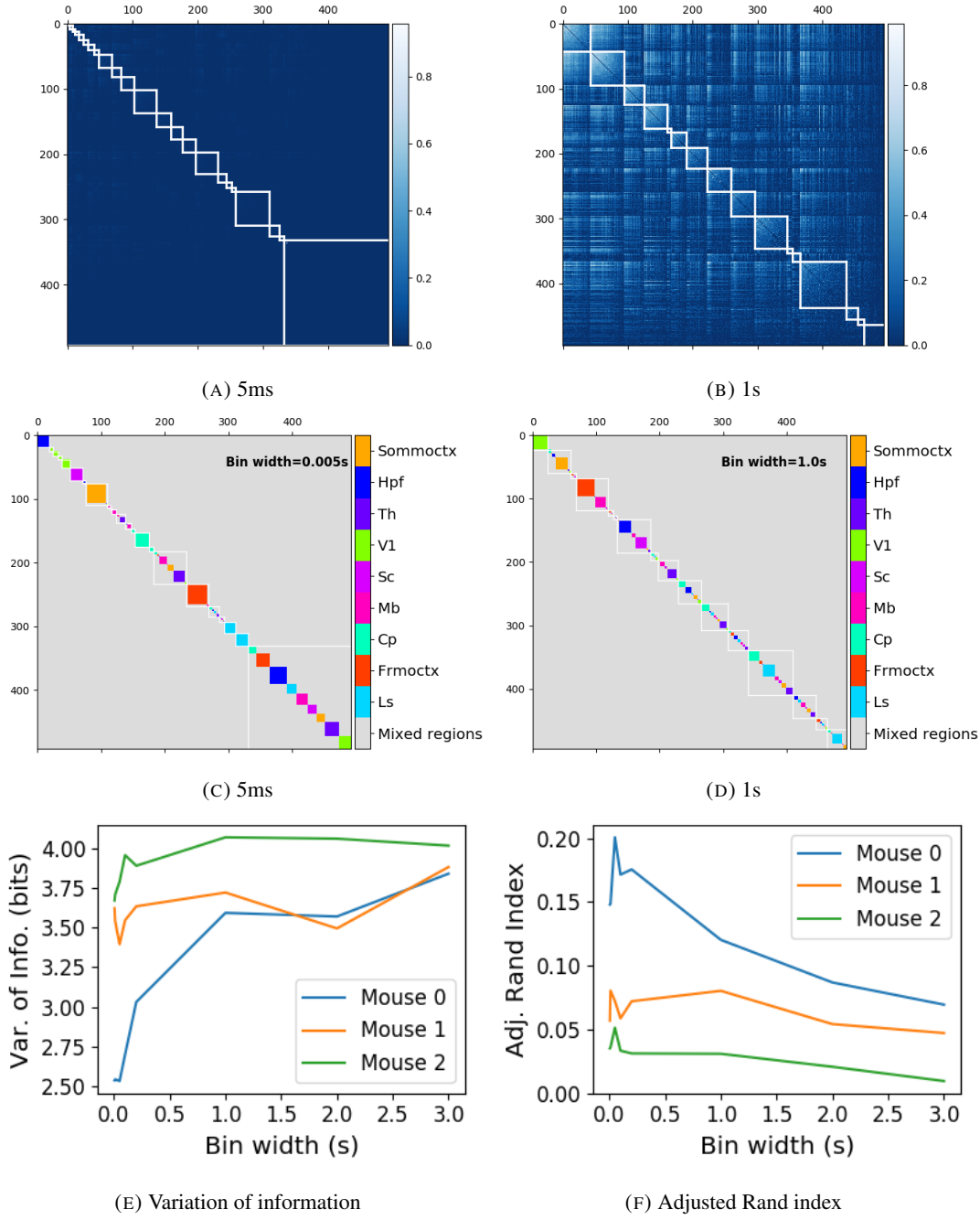


FIGURE 3.16: (A-B) Absolute correlation matrices with detected communities indicated by white lines. These communities are based on the absolute value of the total correlation between each pair of cells. Those entries within a white square indicate that both of those neurons are in the same community. Matrices shown are for 5ms and 1s time bin widths respectively. Main diagonal entries were set to 0. (C-D) Matrices showing the anatomical distribution of pairs along with their community membership. Regional membership is indicated by the colour bar. (E) Variation of information between the anatomical division of the cells, and the detected communities. (F) Adjusted Rand index between the anatomical division, and the detected communities.

### 3.5. Discussion

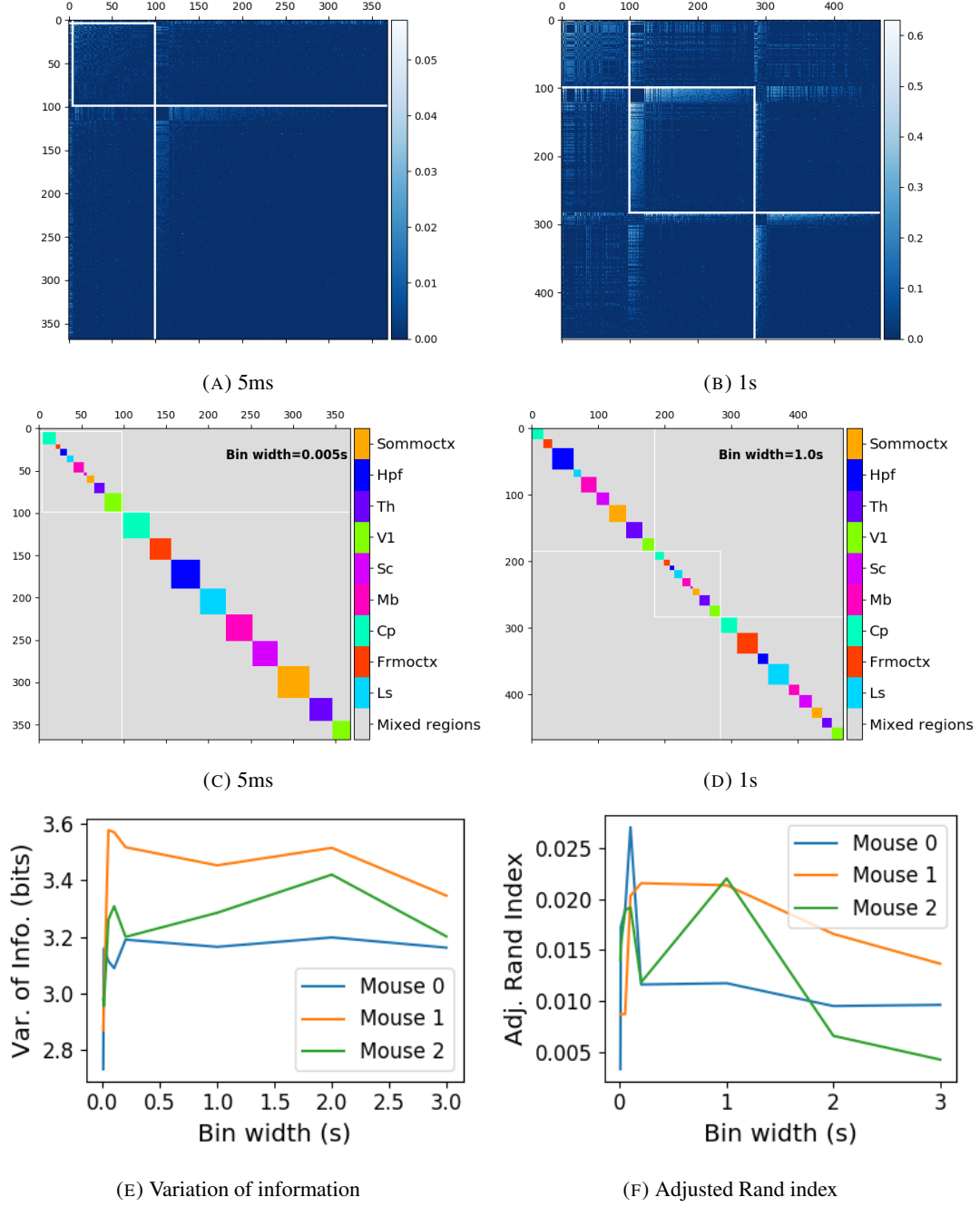


FIGURE 3.17: (A-B) Sign reversed rectified correlation matrices with detected communities indicated by white lines. Those entries within a white square indicate that both of those neurons are in the same community. Matrices shown are for 5ms and 1s time bin widths respectively. Main diagonal entries were set to 0. (C-D) Matrices showing the anatomical distribution of pairs along with their community membership. Regional membership is indicated by the colour bar. (E) Variation of information between the anatomical division of the cells, and the detected communities. (F) Adjusted Rand index between the anatomical division, and the detected communities.

1778 **3.5 Discussion**

1779 It is well established that the brain uses correlated behaviour in neuronal ensembles to repre-  
1780 sent the information taken in through sensation (Cohen and Maunsell, 2009; Litwin-Kumar,  
1781 Chacron, and Doiron, 2012; deCharms and Merzenich, 1996). However, most studies that  
1782 examine the nature of these correlations in-vivo, study an ensemble of cells from only one  
1783 or two brain regions (Cohen and Kohn, 2011; Wierzynski et al., 2009; Patterson et al., 2014;  
1784 Girard, Hupé, and Bullier, 2001). Furthermore, recent results have shown that behaviour can  
1785 drive correlated activity in multiple brain regions, including those not normally associated  
1786 with motor control (Stringer et al., 2019; Gründemann et al., 2019; Allen et al., 2019). In this  
1787 study, we utilised one of the newly recorded large datasets containing electrophysiological  
1788 recordings from multiple brain regions simultaneously. We investigated correlated behaviour  
1789 in these different brain regions and we investigated correlated behaviour between neurons in  
1790 different regions, during spontaneous behaviour.

1791 A number of studies have found that the timescale of correlated behaviour induced by a  
1792 stimulus can be modulated by the stimulus structure and behavioural context. For example,  
1793 the spike train correlations between cells in weakly electric fish are modulated by the spa-  
1794 tial extent of the stimulus (Litwin-Kumar, Chacron, and Doiron, 2012), and neurons in the  
1795 marmoset primary auditory cortex modulate their spike timing (and therefore correlation) in  
1796 response to stimulus features without modulating their firing rate (deCharms and Merzenich,  
1797 1996). Furthermore, the width of the time bins over which spike counts are measured has  
1798 been shown to have an effect on the magnitude of those correlations (Cohen and Kohn, 2011).  
1799 Despite this, very little research has been done comparing correlation measures from the same  
1800 dataset at different timescales. We investigated this by varying the time bin width used to bin  
1801 spike times into spike counts from as short as 5ms up to 3s.

1802 In order to further investigate the effect of these correlations at different timescales, we  
1803 regarded our neuronal ensemble as a weighted undirected graph, where each neuron is rep-  
1804 resented by a node, and the weight on each edge is the correlation between the neurons  
1805 connected by that edge. We then applied a novel clustering method from network science  
1806 (Humphries et al., 2019) to identify communities in these networks. Communities in a net-  
1807 work graph refer to sets of nodes that are more strongly connected to each other than the  
1808 nodes outside of their set. Another way to put this is to say that the nodes in a community  
1809 are more strongly connected than *expected*. What connection strength might be expected is  
1810 defined by a null network model. We chose a null network model that matched the sparsity

### 3.5. Discussion

---

1811 and total strength of our correlation based data networks. So, if two cells were in the same  
1812 community, those cells were more correlated than would be expected given the correlation  
1813 strength of their ensemble.

1814 These networks, and the community detection process, were completely agnostic of the  
1815 anatomical division of the cells in our ensemble. When we compared the detected commu-  
1816 nities with the anatomical division of the cells using distance and similarity measures for  
1817 clusterings, we found that the detected communities were more similar to the anatomical  
1818 division at shorter timescales. That is, when we used a wider time bin to count spikes, and  
1819 computed pairwise correlations with these spike counts, the correlated communities tended to  
1820 exist within anatomical regions at shorter timescales, and tended to span anatomical regions  
1821 at longer timescales. This could reflect localised functional correlations at short time scales  
1822 rippling outwards across brain regions at longer timescales. The brain may be processing  
1823 some information quickly locally, and carrying out further, perhaps more detailed, represen-  
1824 tation over a longer timescale across many regions using the representations that were just  
1825 built locally.

1826 These changes in communities across timescales could also be driven by the anatomy  
1827 of the individual cells. For example, it may simply take longer to transmit action potentials  
1828 over longer distances, hence correlated activity over longer timescales will exist between  
1829 anatomical regions, rather than within. However, the switch to almost exclusively multi-  
1830 regional functional networks at 1s bin widths, rather than a mixture of multi-region, and  
1831 single-region suggests that the inter-regional correlations either overpower, or inhibit the  
1832 local correlations. So there may be more at play than just timescales.

1833 We acknowledged that the region spanning correlated communities that we detected at  
1834 longer time scales could exist due to collating activity driven by distinct spontaneous activ-  
1835 ities. In order to account for this, we modelled the spike counts as a linear function of the  
1836 top 500 principal components of a video of the mouse's face filmed simultaneously with the  
1837 electrophysiological readings. We applied our network noise rejection and community de-  
1838 tection process to the weighted undirected networks formed by the spike count correlations  
1839 (or noise correlations) and the signal correlations that we calculated using our model. For the  
1840 spike count correlation networks, we found much the same results as for the total correlations  
1841 as described above. For the signal correlations, the communities detected in these networks  
1842 bore little relation to the anatomical division of the cells. Recent findings have shown that  
1843 behavioural data accounts for correlations in many brain regions that would otherwise be  
1844 dismissed as noise (Stringer et al., 2019), our finding to shows that these correlations are still

1845 governed by the timescale division between local communication and across-region commu-  
1846 nication.

1847 There is a lot of room for further investigation based on this research. For a start, the  
1848 data that we used here were collected from nine different regions in the mouse brain, but  
1849 none of these regions were part of the somatosensory cortex. Given that a mouse experiences  
1850 so much of its environment through its sense of smell, some data from this region would be  
1851 interesting to investigate. On the same theme, the mice in the experiment from which the  
1852 data were collected were headfixed and placed on a rotating ball, but were otherwise behav-  
1853 ing spontaneously. Had these mice been exposed to a visual, aural, or olfactory stimulus,  
1854 we could have examined the responses of the cells in the brain regions corresponding to vi-  
1855 sion, hearing, and olfaction, and compared these responses to the responses from the other  
1856 brain regions. Furthermore, we could have investigated the interaction between the sets of  
1857 responses.

1858 Another space for further investigation is the community detection. The algorithm that we  
1859 used here never detects overlapping communities. But functional communities could indeed  
1860 have overlaps. Clustering methods that detect overlapping clusters do exist (Baadel, Thabtah,  
1861 and Lu, 2016). Applying one of those algorithms could yield some interesting results. Also,  
1862 the community detection algorithm that we used here cannot process graphs with negative  
1863 weights, this forced us to separate positive and negative correlations before applying our  
1864 network noise rejection and community detections process, or use the absolute value of our  
1865 correlations. A community detection algorithm that can work on weighted undirected graphs  
1866 with negative weights could yield some interesting results here.

1867 **Chapter 4**

1868 **A simple two parameter distribution  
1869 for modelling neuronal activity and  
1870 capturing neuronal association**

1871 *Abstract*

1872 Recent developments in electrophysiological technology have lead to an increase in the size  
1873 of electrophysiology datasets. Consequently, there is a requirement for new analysis tech-  
1874 niques that can make use of these new datasets, while remaining easy to use in practice. In  
1875 this work, we fit some one or two parameter probability distributions to spiking data collected  
1876 from a mouse exposed to visual stimuli. We show that the Conway-Maxwell-binomial dis-  
1877 tribution is a suitable model for the number of active neurons in a neuronal ensemble at any  
1878 given moment. This distribution fits these data better than binomial or beta-binomial distribu-  
1879 tions. It also captures the correlated activity in the primary visual cortex induced by stimulus  
1880 onset more effectively than simply measuring the correlations, at short timescales (< 10ms).  
1881 We also replicate the finding of Churchland et al (2010) relating to stimulus onset quenching  
1882 neural variability in cortical areas, and we show a correspondence between this quenching  
1883 and changes in one of the parameters of the fitted Conway-Maxwell-binomial distributions.

1884 **4.1 Introduction**

1885 Recent advances in electrophysiological technology, such as ‘Neuropixels’ probes (Jun et al.,  
1886 2017) have allowed extracellular voltage measurements to be collected from larger numbers  
1887 of cells than traditional methods, in multiple brain regions simultaneously, and routinely.  
1888 These larger datasets require innovative methods to extract information from the data in a  
1889 reasonable amount of time, ‘reasonable’ being subjective in this case.

1890 Theoretically, all the information at any given moment in an electrophysiological dataset  
1891 with  $n$  neurons could be captured by calculating the probability distribution for every possi-  
1892 ble spiking pattern. This would require defining a random variable with  $2^n$  possible values, a  
1893 task that quickly becomes impossible as  $n$  increases. Attempts at approximating this random  
1894 variable often involve measuring pairwise or higher order correlations (Schneidman et al.,  
1895 2006; Flach, 2013; Ganmor, Segev, and Schneidman, 2011). But pairwise correlations may  
1896 not be enough to characterise instantaneous neural activity (Tkačik et al., 2014). Further-  
1897 more, these kinds of models tend to ignore the temporal structure of neuronal data, in favour  
1898 of smaller model size, and scalability.

1899 Higher order correlations would be helpful here, but defining and quantifying these cor-  
1900 relations can be tricky (Staude, Grün, and Rotter, 2010). If we use the interaction parameters  
1901 arising from the exponential family model as measures of higher order correlations, mea-  
1902 suring these correlations becomes computationally impractical quite quickly (the number  
1903 of ‘three neuron correlations’ to measure scales with  $\binom{n}{3}$ ). In this work, we dispense with  
1904 measuring correlations directly, and we attempt to characterise correlated behaviour using a  
1905 parameter in statistical model.

1906 In this work, we examined the ability of simple distributions to model the number of  
1907 active (spiking) neurons in a neuronal ensemble at any given timepoint. We compared a  
1908 little-known distribution named the Conway-Maxwell-binomial distribution to the binomial  
1909 distribution and the beta-binomial distribution. The binomial distribution is a probability dis-  
1910 tribution over the number of successes in a sequence of independent and identical Bernoulli  
1911 trials. The beta-binomial distribution is similar, but allows for a bit more flexibility while still  
1912 being a model for heterogeneity. Similar to the binomial and beta-binomial, the Conway-  
1913 Maxwell-binomial distribution is a probability distribution over the number of successes in a  
1914 series of Bernoulli trials, but allows over- and under-dispersion relative to the binomial dis-  
1915 tribution. This distribution should therefore be a good candidate for our purposes. We found  
1916 that Conway-Maxwell-binomial distribution was usually the best candidate of the three that

## 4.2. Data

---

1917 we examined.

1918 We also observed some interesting changes in the number of active neurons in the primary  
1919 visual cortex and hippocampus at stimulus onset and some changes in this activity in the  
1920 thalamus which were sustained for the full duration of the stimulus presentation. This let us  
1921 know that there were some responses to model.

1922 We found that fitting a Conway-Maxwell-binomial distribution was a better method of  
1923 capturing association between neurons than measuring the spike count correlation for the  
1924 short time bins that we used (< 10ms).

1925 Finally, we also wanted to investigate parallels between the parameters of the Conway-  
1926 Maxwell-binomial distribution and quantities that have been established as relevant to sen-  
1927 sory processing. So, we replicated the findings made by Churchland et al. (2010) relating  
1928 to a reduction in neural variability at stimulus onset in the macaque cortical regions, but for  
1929 data taken from the mouse primary visual cortex. We compared these findings to the values  
1930 of the fitted Conway-Maxwell-binomial distribution parameters.

## 1931 4.2 Data

1932 We used data collected by Nick Steinmetz and his lab ‘CortexLab at UCL’ (Steinmetz, Caran-  
1933 dini, and Harris, 2019). The data can be found online <sup>1</sup> and are free to use for research  
1934 purposes.

1935 Two ‘Phase3’ Neuropixels (Jun et al., 2017) electrode arrays were inserted into the brain  
1936 of an awake, head-fixed mouse for about an hour and a half. These electrode arrays recorded  
1937 384 channels of neural data each at 30kHz and less than  $7\mu\text{V}$  RMS noise levels. The sites  
1938 are densely spaced in a ‘continuous tetrode’-like arrangement, and a whole array records  
1939 from a 3.8mm span of the brain. One array recorded from visual cortex, hippocampus, and  
1940 thalamus, the other array recorded from motor cortex and striatum. The data were spike-  
1941 sorted automatically by Kilosort and manually by Nick Steinmetz using Phy. In total 831  
1942 well-isolated individual neurons were identified.

### 1943 4.2.1 Experimental protocol

1944 The mouse was shown a visual stimulus on three monitors placed around the mouse at right  
1945 angles to each other, covering about  $\pm 135$  degrees azimuth and  $\pm 35$  degrees elevation.

---

<sup>1</sup><http://data.cortexlab.net/dualPhase3/>

1946 The stimulus consisted of sine-wave modulated full-field drifting gratings of 16 drift di-  
1947 rections ( $0^\circ, 22.5^\circ, \dots, 337.5^\circ$ ) with 2Hz temporal frequency and 0.08 cycles/degree spatial  
1948 frequency displayed for 2 seconds plus a blank condition. Each of these 17 conditions were  
1949 presented 10 times in a random order across 170 different trials. There were therefore 160  
1950 trials with a drifting-grating visual stimulus present, and 10 trials with a blank stimulus.

1951 **4.3 Methods**

1952 **4.3.1 Binning data**

1953 We converted the spike times for each cell into spike counts by putting the spike times into  
1954 time bins of a given ‘width’ (in milliseconds). We used time bins of 1ms, 5ms, and 10ms.  
1955 We used different time bin widths to assess the impact of choosing a bin width.

1956 **4.3.2 Number of *active* neurons**

1957 To count the number of active neurons in each neuronal ensemble, we split the time interval  
1958 for each trial into bins of a given width. We counted the number of spikes fired by each cell  
1959 in each bin. If a cell fired *at least* one spike in a given bin, we regarded that cell as active in  
1960 that bin. We recorded the number of active cells in every bin, and for the purposes of further  
1961 analysis, we recorded each cell’s individual spike counts.

1962 It should be noted that when we used a bin width of 1ms, the maximum number of  
1963 spikes in any bin was 1. For the wider time bins, some bins had spike counts greater than  
1964 1. Consequently when using a bin width of 1ms, the number of active neurons and the total  
1965 spike count of a given bin were identical. But for wider bin widths, the total spike count was  
1966 greater than the number of active neurons.

1967 So for the 1ms bin width, the activity of a neuron and the number of spikes fired by that  
1968 neuron in any bin can be modelled as a Bernoulli variable. But for wider time bins, only the  
1969 activity can be modelled in this way.

1970 **4.3.3 Moving windows for measurements**

1971 When taking measurements (e.g. moving average over the number of active neurons) or  
1972 fitting distributions (eg. the beta binomial distribution) we slid a window containing a certain  
1973 number of bins across the data, and made our measurements at each window position. For  
1974 example, when analysing 1ms bin data, we used a window containing 100 bins, and we slid

### 4.3. Methods

---

Bin width (ms)	Window size (bins)	Window size (ms)	Windows per trial
1ms	100	100ms	296
5ms	40	200ms	286
10ms	40	400ms	266

TABLE 4.1: Details of the different bin width and analysis window sizes used when binning spike times, and analysing those data.

1975 the window across the time interval for each trial moving 10 bins at a time. So that for  
 1976 3060ms of data, we made 296 measurements.

1977 For the 5ms bin width data, we used windows containing 40 bins, and slid the window 2  
 1978 bins at a time when taking measurements.

1979 For the 10ms bin width data, we used windows containing 40 bins, and slid the window  
 1980 1 bin at a time when taking measurements (see table 4.1 for concise details).

1981 By continuing to use windows containing 40 bins, we retained statistical power but sac-  
 1982 rificed the number of measurements taken.

1983 There was an interval between each trial with a grey image in place of the moving bar  
 1984 stimulus. This interval varied in time. But we included some of this interval when recording  
 1985 the data for each trial. We started recording the number of active neurons, and the number  
 1986 of spikes from each neuron from 530ms before each trial until 1030ms after each trial. This  
 1987 way, we could see the change in our measurements at the onset of a stimulus and the end of  
 1988 stimulus presentation.

1989 As mentioned in section 4.3.2, we recorded the number of active neurons in each bin, and  
 1990 the spike count for each neuron in each bin. The measurements we took using these data in  
 1991 each window were as follows:

1992 **Moving average** The average number of active cells in each window.

1993 **Moving variance** The variance of the number of active cells in each window.

1994 **Average correlation** We measured the correlation between the spike counts of each pair of  
 1995 cells in the ensemble, and took the average of these measurements.

1996 **Binomial  $p$**  We fitted a binomial distribution to the data in each window and recorded the  
 1997 fitted probability of success,  $p$  in each case.

1998 **Beta-binomial  $\alpha, \beta$**  We fitted a beta-binomial distribution to the data in each window, and  
 1999 recorded the values of the fitted shape parameters,  $\alpha$  and  $\beta$ , of each distribution.

2000 **Conway-Maxwell-binomial distribution  $p, \nu$**  We fitted a Conway-Maxwell-binomial dis-  
2001 tribution to the data in each window, and recorded the fitted values of  $p$  and  $\nu$  for each  
2002 distribution.

2003 **Log-likelihoods** We also recorded the log-likelihood of each of the fitted distributions for  
2004 each window.

2005 **4.3.4 Fano factor**

The *Fano factor* of a random variable is defined as the ratio of the variable's variance to its mean.

$$F = \frac{\sigma^2}{\mu} \quad (4.1)$$

2006 We measured the Fano factor of the spike count of a given cell by measuring the mean and  
2007 variance of the spike count across trials, and taking the ratio of those two quantities. When  
2008 calculated in this way the Fano factor can be used as a measure of neural variability that  
2009 controls for changes in the firing rate. This is similar to the calculation used in (Churchland  
2010 et al., 2010).

2011 **4.3.5 Probability Distributions suitable for modelling ensemble activity**

2012 We present here three different probability distributions that could be suitable to model the  
2013 number of active neurons in an ensemble. Each distribution has the set  $\{0, \dots, n\}$  as its sup-  
2014 port, where  $n$  is the number of neurons in the ensemble. These are simple distributions with  
2015 either two or three parameters each. However, we regard  $n$  as known when using these dis-  
2016 tributions for modelling, so in effect each distribution has either one or two free parameters.

2017 **Association**

2018 *Association* between random variables is similar to the correlation between random variables  
2019 but is more general in concept. The correlation coefficient is a measure of association; and  
2020 association doesn't necessarily have a mathematical definition like correlation does. Essen-  
2021 tially, an association between two random variables is a dependency of any kind. Positively  
2022 associated variables tend to take the same value, and negatively associated variables tend to  
2023 take different values. In this research, we work with probability distributions of the num-  
2024 ber of successes in a set of Bernoulli trials. These Bernoulli variables may or may not be  
2025 associated.

### 4.3. Methods

---

2026 A probability distribution over the number of successes in  $n$  Bernoulli trials, where the  
2027 Bernoulli variables may be associated, could constitute a good model for the number of active  
2028 neurons in an ensemble of  $n$  neurons. As long as the observation period is divided into time  
2029 bins short enough so that any neuron is unlikely to fire more than spike in any time bin.

2030 **Binomial distribution**

The binomial distribution is a two parameter discrete probability distribution that can be thought of as a probability distribution the number of successes from  $n$  independent Bernoulli trials, each with the same probability of success. The parameters of the binomial distribution are  $n$  the number of trials, and  $0 \leq p \leq 1$ , the probability of success for each of these trials. A random variable with the binomial distribution can take values from  $\{0, \dots, n\}$ .

The probability mass function of the distribution is

$$P(k; n, p) = \binom{n}{k} p^k (1-p)^{n-k} \quad (4.2)$$

2031 As a model for the activity of a neuronal ensemble, the main problem with the binomial  
2032 distribution is that it treats each neuron, represented as a Bernoulli trial, as independent. It is  
2033 well known that neurons are not independent, and that correlated behaviour between neurons  
2034 is vital for representing sensory information (Cohen and Maunsell, 2009). The binomial dis-  
2035 tribution falls short in this regard, but it is useful as performance benchmark when assessing  
2036 the performance of other models.

2037 **Beta-binomial distribution**

2038 The beta distribution is the conjugate distribution of the binomial distribution. The beta-  
2039 binomial distribution is the combination of the beta distribution and the binomial distribution,  
2040 in that the probability of success for the binomial distribution is sampled from the beta dis-  
2041 tribution. This allows the beta-binomial distribution to capture some over dispersion relative  
2042 to the binomial distribution.

The beta-binomial distribution is a three parameter distribution,  $n$  the number of Bernoulli trials, and  $\alpha \in \mathbb{R}_{>0}$  and  $\beta \in \mathbb{R}_{>0}$  the shape parameters of the beta distribution. The probability mass function for the beta-binomial distribution is

$$P(k; n, \alpha, \beta) = \binom{n}{k} \frac{B(k + \alpha, n - k + \beta)}{B(\alpha, \beta)} \quad (4.3)$$

2043 where  $B(\alpha, \beta)$  is the beta function.

This probability distribution can be reparametrised in a number of ways. One of which defines new parameters  $\pi$  and  $\rho$  by

$$\pi = \frac{\alpha}{\alpha + \beta} \quad (4.4)$$

$$\rho = \frac{1}{\alpha + \beta + 1} \quad (4.5)$$

2044 This reparametrisation is useful because  $\pi$  acts as a location parameter analogous to the  $p$   
2045 parameter of a binomial distribution. A value of  $\rho > 0$  indicates over-dispersion relative to a  
2046 binomial distribution.

2047 As a model for the activity of a neuronal ensemble, the beta-binomial distribution is  
2048 more suitable than a binomial distribution because the over-dispersion of the beta-binomial  
2049 distribution can be used to model positive association between the neurons. An extreme  
2050 example of this over-dispersion/positive association can be seen in figure 4.1b. In this figure,  
2051 the neurons are positively associated and so tend to take the same value, consequently the  
2052 probability mass of the beta-binomial distribution builds up close to  $k = 0$  and  $k = n$ . It is  
2053 worth noting that the location parameter for each distribution has the same value,  $p = \pi =$   
2054 0.5.

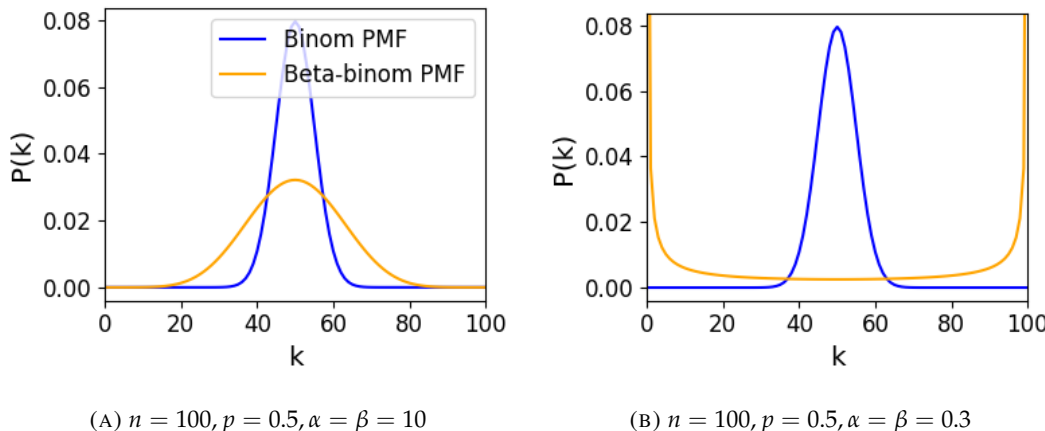


FIGURE 4.1: Figures showing the over-dispersion possible for a beta-binomial distribution relative to a binomial distribution. Parameters are shown in the captions.

2055 **Conway-Maxwell-binomial distribution**

2056 The Conway-Maxwell-binomial distribution (COMb distribution) is a three parameter generalisation of the binomial distribution that allows for over dispersion and under dispersion

### 4.3. Methods

---

relative to the binomial distribution. The parameters of the distribution are  $n$  the number of Bernoulli trials, and two shape parameters  $0 \leq p \leq 1$ , and  $\nu \in \mathbb{R}$ .

The probability mass function of the COMb distribution is

$$P(k; n, p, \nu) = \frac{1}{S(n, p, \nu)} \binom{n}{k}^{\nu} p^k (1-p)^{n-k} \quad (4.6)$$

where

$$S(n, p, \nu) = \sum_{j=0}^n \binom{n}{j}^{\nu} p^j (1-p)^{n-j} \quad (4.7)$$

The only difference between this PMF and the PMF for the standard binomial is the introduction of  $\nu$  and the consequent introduction of the normalising function  $S(n, p, \nu)$ .

Indeed, if  $\nu = 1$  the COMb distribution is identical to the binomial distribution with the same values for  $n$  and  $p$ . We can see in figure 4.2d that the KL-divergence  $D_{KL}(P_{COMb}(n, p, \nu) || P_{Bin}(n, p)) = 0$  along the line where  $\nu = 1$ . The analytical expression for the divergence is

$$D_{KL}(P_{COMb}(k; n, p, \nu) || P_{Bin}(k; n, p)) = (\nu - 1) E_{P_{COMb}(k; n, p, \nu)} \left[ \log \binom{n}{k} \right] \quad (4.8)$$

$$- \log S(n, p, \nu) \quad (4.9)$$

At  $\nu = 1$ , we have  $S(n, p, 1)$  which is just the sum over the binomial PMF, so  $S(n, p, 1) = 1$  and therefore  $D_{KL}(P_{COMb}(n, p, \nu) || P_{Bin}(n, p)) = 0$ .

If  $\nu < 1$  the COMb distribution will exhibit over-dispersion relative to the binomial distribution. If  $p = 0.5$  and  $\nu = 0$  the COMb distribution is the discrete uniform distribution, and if  $\nu < 0$  the mass of the COMb distribution will tend to build up near  $k = 0$  and  $k = n$ . This over-dispersion represents positive association in the Bernoulli variables. An example of this over-dispersion can be seen in figure 4.2b.

If  $\nu > 1$  the COMb distribution will exhibit under-dispersion relative to the binomial distribution. The larger the value of  $\nu$  the more probability mass will build up at  $n/2$  for even  $n$ , or at  $\lfloor n/2 \rfloor$  and  $\lceil n/2 \rceil$  for odd  $n$ . This under-dispersion represents negative association in the Bernoulli variables. An example of this under-dispersion can be seen in figure 4.2a.

It should be noted that the  $p$  parameter of the COMb distribution does not correspond to the mean of the distribution, as is the case for the binomial  $p$  parameter, and beta-binomial  $\pi$  parameter. That is, the COMb  $p$  parameter is not a location parameter. An illustration of this can be seen in figure 4.2c. This is because an interaction between the  $p$  and  $\nu$  parameters skews the mean. There is no analytical expression for the mean of the COMb distribution.

$\nu$	Relative dispersion	Association between neurons/variables
< 1	over	positive
1	none	none
> 1	under	negative

TABLE 4.2: Relative dispersion of the COMb distribution, and association between Bernoulli variables as represented by the value of the  $\nu$  parameter.

2078 Since the COMb distribution has the potential to capture positive and negative associa-  
2079 tions between the neurons/Bernoulli variables, it should be an excellent candidate for mod-  
2080 elling the number of active neurons in a neuronal ensemble.

2081 We wrote a dedicated Python package to enable easy creation and fitting of COMb dis-  
2082 tribution objects. The format of the package imitates the format of other distribution objects  
2083 from the `scipy.stats` Python package. The COMb package can be found here:  
2084 [https://github.com/thomasjdelaney/Conway\\_Maxwell\\_Binomial\\_Distribution](https://github.com/thomasjdelaney/Conway_Maxwell_Binomial_Distribution)

2085 **4.3.6 Fitting**

2086 We fitted binomial, beta-binomial, and Conway-Maxwell-binomial (COMb) distributions to  
2087 the neural activity in each of the overlapping windows covering each trial. To fit the distribu-  
2088 tions we minimised the appropriate negative log likelihood function using the data from the  
2089 window.

There is an analytical solution for maximum likelihood estimate of the binomial distribution's  $p$  parameter.

$$\hat{p} = \frac{1}{n} \sum_{i=1}^N k_i \quad (4.10)$$

2090 We minimised the negative log likelihood function of the beta-binomial distribution nu-  
2091 merically. We calculated the negative log likelihood for a sample directly, by taking the sum  
2092 of the log of the probability mass function for each value in the sample. We minimised the  
2093 negation of that function using the `minimise` function of the `scipy.optimize` Python  
2094 package.

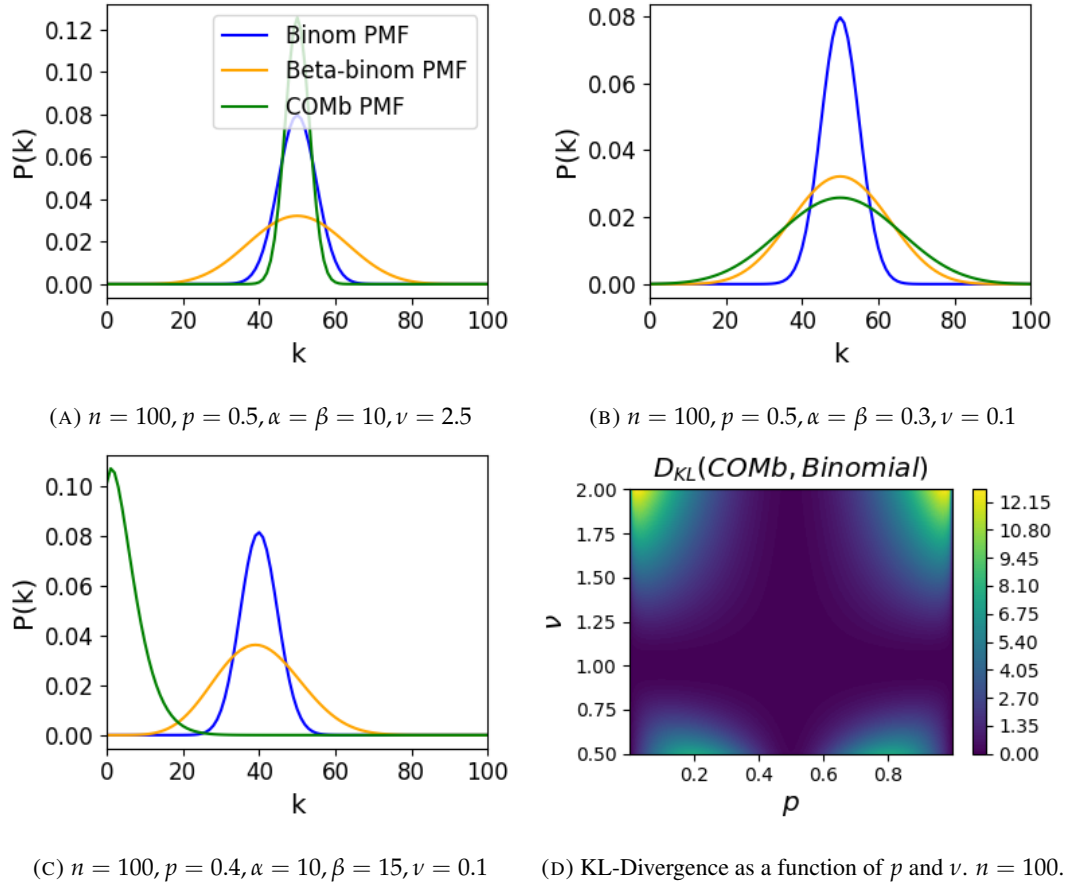


FIGURE 4.2: Figures showing (A) the under-dispersion and (B) over-dispersion permitted by the COMb distribution relative to a binomial distribution. (C) illustrates that the  $p$  parameter of the COMb distribution does not correspond to the mean of the distribution, as it does for the binomial and beta-binomial distributions. (D) shows a heatmap for the value of the Kullback-Liebler divergence between the COMb distribution and the standard binomial distribution with same value for  $n$ , as a function of  $p$  and  $\nu$ . Parameters are shown in the captions.

The log likelihood function of the COMb distribution given some sample  $\{k_1, \dots, k_N\}$  is

$$\ell(p, \nu | k_1, \dots, k_N) = N [n \log(1 - p) - \log S(n, p, \nu)] \quad (4.11)$$

$$+ \log \frac{p}{1 - p} \sum_{i=1}^N k_i \quad (4.12)$$

$$+ \nu \sum_{i=1}^N \log \binom{n}{k_i} \quad (4.13)$$

2095 We minimised the negation of this function using numerical methods. More specifically, we  
2096 used the `minimise` function of the `scipy.optimize` Python package.

2097 **4.3.7 Goodness-of-fit**

2098 After fitting, we measured the goodness-of-fit of each model/distribution with their log like-  
2099 lihood. We calculated this directly using the `logpmf` functions of the distribution objects in  
2100 Python.

2101 **4.4 Results**

2102 We defined a neuron as *active* in a time bin if it fires at least one spike during the time interval  
2103 covered by that bin. We measured the number of active neurons in the primary visual cortex  
2104 of a mouse in 1ms bins across 160 trials of a moving bar visual stimulus. We then slid a  
2105 100ms window across these 1ms bins taking measurements, and fitting distributions along  
2106 the way. We did the same for neurons in the thalamus, hippocampus, striatum, and motor  
2107 cortex. We repeated the analysis for 5ms time bins with 40 bin windows, and 10ms time bins  
2108 with 40 bin windows.

2109 **4.4.1 Increases in mean number of active neurons and variance in number of  
2110 active neurons at stimulus onset in some regions**

2111 We measured the average number of active neurons, and the variance of the number of active  
2112 neurons in a 100ms sliding window starting 500ms before stimulus onset until 1000ms after  
2113 stimulus onset. We found differences in the response across regions. There were no observed  
2114 changes in response to the stimulus in the motor cortex or the striatum. The changes in the  
2115 other regions are detailed below.

## 4.4. Results

---

### 2116 Primary visual cortex

2117 We found a transient increase in both the average and variance of the number of active neu-  
2118 rons at stimulus onset, followed by a fall to pre-stimulus levels, followed by another transient  
2119 increase (see figure 4.3). The oscillation in both of these measurements appear to reflect the  
2120 frequency of the stimulus (see Data section 4.2.1), and it is known that stimulus structure can  
2121 influence response structure(Litwin-Kumar, Chacron, and Doiron, 2012). We see a similar  
2122 but lower amplitude oscillation at the end of the stimulus presentation.

### 2123 Hippocampus

2124 In the hippocampus we observed a transient increase in the average number of active neurons  
2125 and in the variance of the number of active neurons at stimulus onset (see figure 4.4). The  
2126 increase lasted about 125ms, and the subsequent fall to baseline took the a similar amount of  
2127 time.

### 2128 Thalamus

2129 In the thalamus we observed a transient increase in the both the average and variance of  
2130 the number of active neurons on stimulus onset, followed by a fall to pre-stimulus levels,  
2131 followed by a sustained increase until the stimulus presentation ends.

2132 As one you might expect for a visual stimulus, the change in the average number of active  
2133 neurons was greatest in the primary visual cortex. In this region, this quantity doubled on  
2134 stimulus onset. In contrast, in the hippocampus and the thalamus, the average number of  
2135 active neurons only increased by a fraction of the unstimulated baseline value. The duration  
2136 of the response in V1 and the hippocampus at stimulus onset was 300 – 400ms, but the  
2137 response in the thalamus appeared to last for the duration of stimulus presentation. The V1  
2138 also showed a change in the average number of active neurons at stimulus end. The change  
2139 was similar to that observed at stimulus onset, but smaller in magnitude (see figures 4.3, 4.4,  
2140 and 4.5)

### 2141 4.4.2 Conway-Maxwell-binomial distribution is usually a better fit than bino- 2142 mial or beta-binomial

2143 Since the Conway-Maxwell-binomial distribution has not been fitted to neuronal data before,  
2144 it is not clear that it would be a better fit than the binomial or beta-binomial distributions.  
2145 In order to find out which parametric distribution was the best fit for the largest proportion

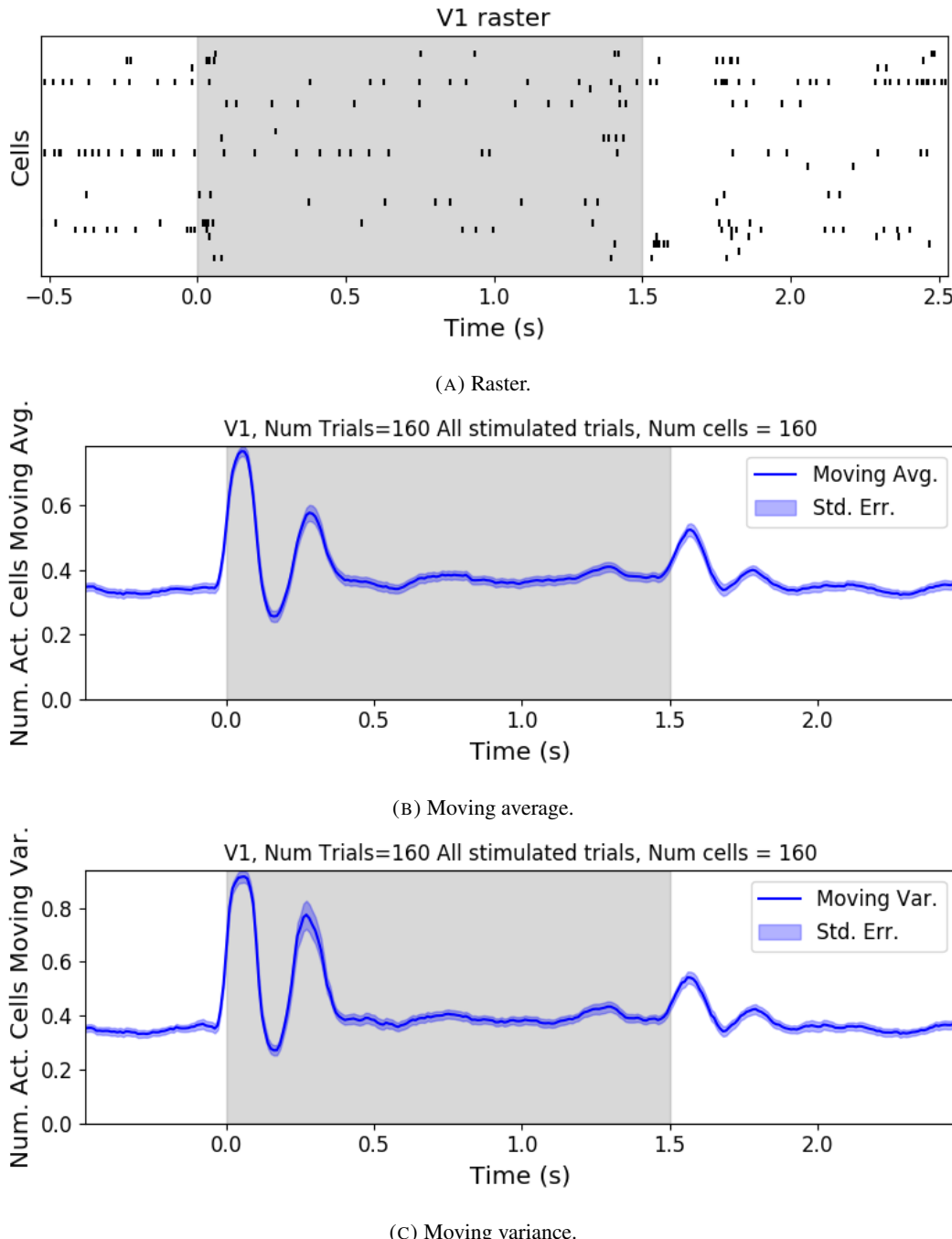


FIGURE 4.3: (A) Raster plot showing the spikes fired by 33 randomly chosen neurons in the primary visual cortex. (B-C) (B) average and (C) variance of the number of active neurons, measured using a sliding window 100ms wide, split into 100 bins. The midpoint of the time interval for each window is used as the timepoint (x-axis point) for the measurements using that window. The grey shaded area indicates the presence of a visual stimulus. The opaque line is an average across the 160 trials that included a visual stimulus of any kind. We can see a transient increase in the average number of active neurons and the variance of this number, followed by a fluctuation and another increase.

#### 4.4. Results

---

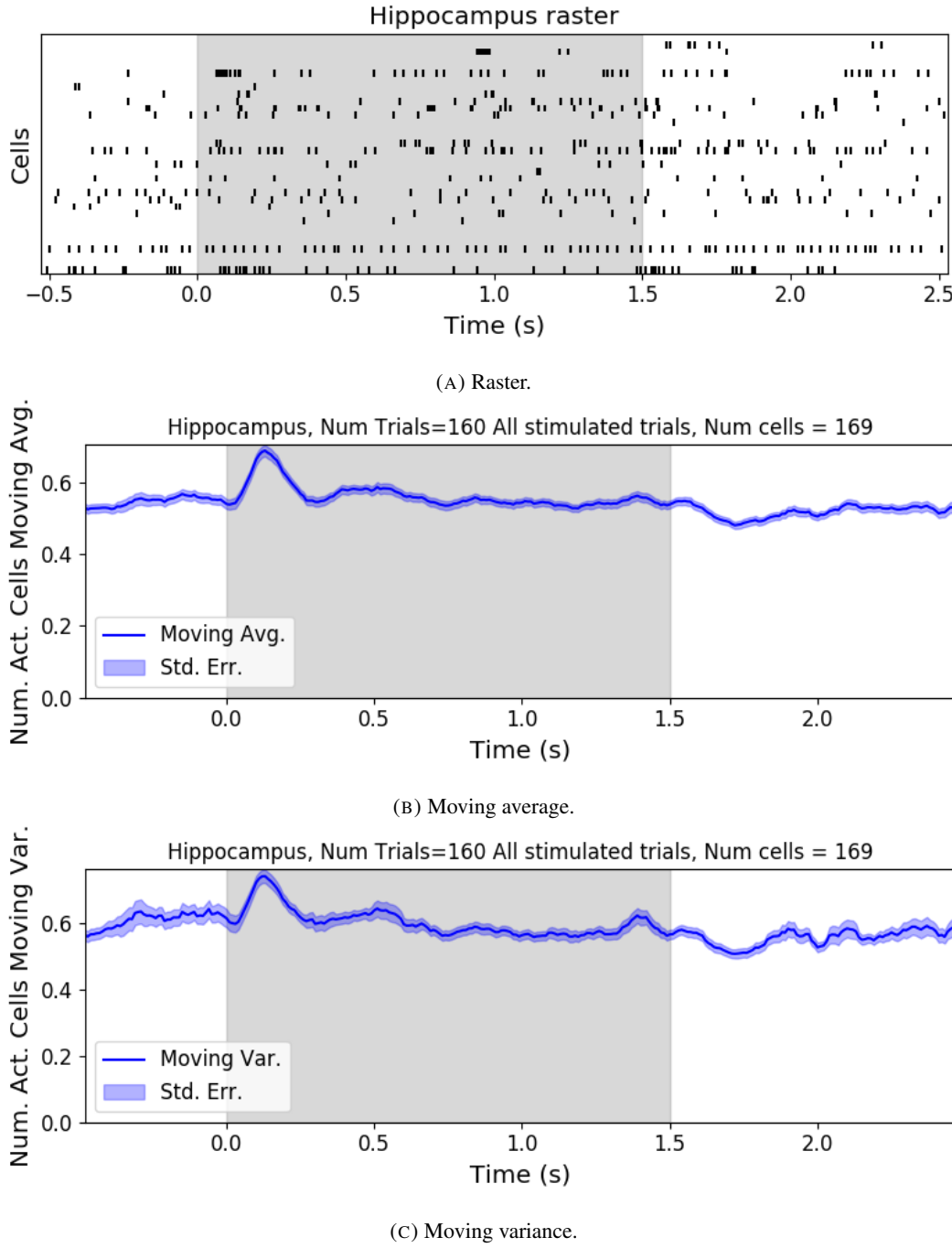


FIGURE 4.4: (A) Raster plot showing the spikes fired by 33 randomly chosen neurons in the hippocampus. (B-C) (B) average and (C) variance of the number of active neurons, measured using a sliding window 100ms wide, split into 100 bins. The midpoint of the time interval for each window is used as the timepoint (x-axis point) for the measurements using that window. The grey shaded area indicates the presence of a visual stimulus. The opaque line is an average across the 160 trials that included a visual stimulus of any kind. We can see a transient increase in the average number of active neurons and the variance of this number at stimulus onset.

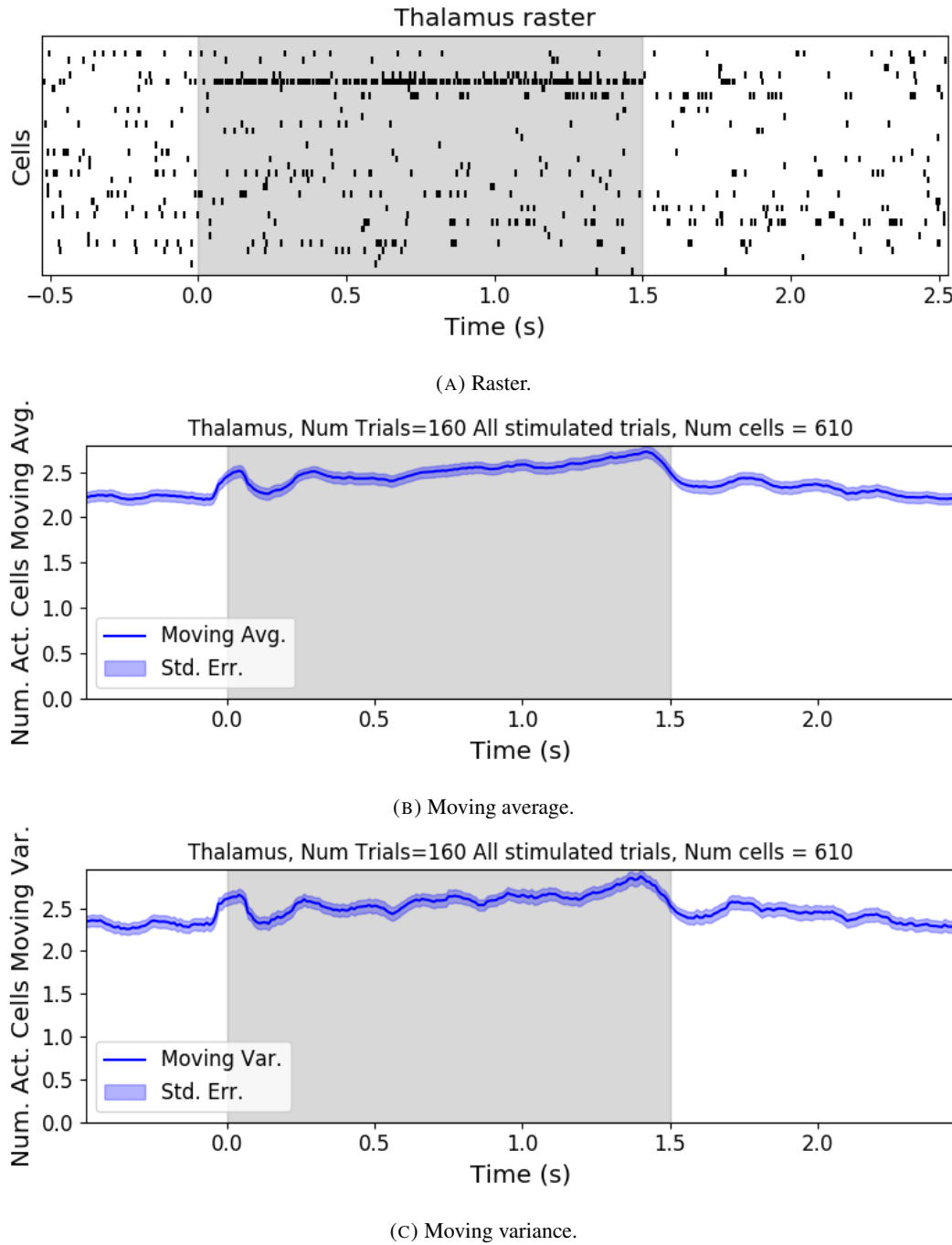


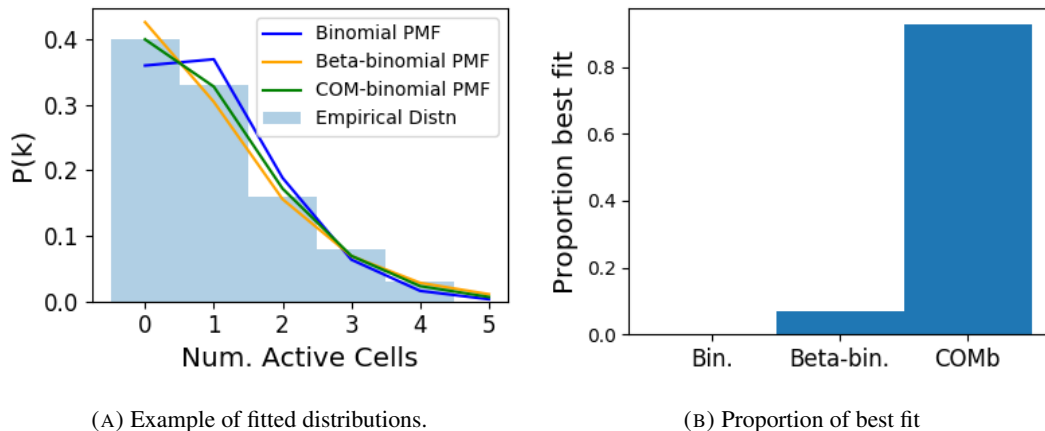
FIGURE 4.5: (A) Raster plot showing the spikes fired by 33 randomly chosen neurons in the thalamus. (B-C) (B) average and (C) variance of the number of active neurons, measured using a sliding window 100ms wide, split into 100 bins. The midpoint of the time interval for each window is used as the timepoint (x-axis point) for the measurements using that window. The grey shaded area indicates the presence of a visual stimulus. The opaque line is an average across the 160 trials that included a visual stimulus of any kind. We can see an immediate increase at stimulus onset, a subsequent fall, and another sustained increased until the stimulus presentation ends.

#### 4.4. Results

---

of our data, we fit a binomial, a beta-binomial, and a Conway-Maxwell-binomial (COMb) distribution to each window for each bin width, and each region. Then we assessed the goodness-of-fit of each distribution by calculating the log-likelihood of each fitted distribution using the associated sample. We measured the proportion of samples for which each distribution was the best fit, for each bin width value and each region.

We found that the COMb distribution was the best fit for most of the samples regardless of bin width or region. The bin width had an effect on the number of samples for which the COMb distribution was the best fit. The results are summarised in table 4.3. For a bin width of 1ms, the COMb distribution was the best fit for over 90% of samples, the beta-binomial distribution was the best fit for less than 10% of samples, and the binomial distribution was the best fit for less than 1% of samples, across regions. For 5ms bins, the COMb distribution was the best fit for 70 – 80% of samples, the beta-binomial distribution was the best fit for 20 – 30% of the samples, and again the binomial distribution was the best fit for less than 1% of samples, across regions. Finally, for 10ms bins, the COMb distribution was the best fit for 53 – 80% of samples, the beta-binomial distribution was the best fit for 20 – 47% of the samples, and the binomial distribution was the best fit for less than 0.1% of samples, across regions.



(A) Example of fitted distributions. (B) Proportion of best fit

FIGURE 4.6: (A) An example of the binomial, beta-binomial, and Conway-Maxwell-binomial distributions fitted to a sample of neural activity. The Conway-Maxwell-binomial distribution is the best fit in this case. The histogram shows the empirical distribution of the sample. The probability mass function of each distribution is indicated by a different coloured line. (B) Across all samples in all trials, the proportion of samples for which each fitted distribution was the best fit. The Conway-Maxwell-binomial distribution was the best fit for 93% of the samples taken from V1 using a bin width of 1ms.

Bin Width (ms)	Binomial	Beta-binomial	COMb
1ms	< 1%	< 10%	> 90%
5ms	< 0.1%	20 – 30%	70 – 80%
10ms	< 0.1%	20 – 47%	53 – 80%

TABLE 4.3: Proportion of samples for which each distribution was the best fit, grouped by bin width. The COMb distribution is the best fit most of the time.

2163 **4.4.3 Conway-Maxwell-binomial distribution captures changes in association  
2164 at stimulus onset**

2165 We fit a Conway-Maxwell-binomial (COMb) distribution to the number of active neurons in  
2166 the 1ms time bins in a 100ms sliding window. We also measured the correlation coefficient  
2167 between the spike counts of all possible pairs of neurons, and took the average of these  
2168 coefficients. We did this for all the trials with a visual stimulus. We observed a reduction in  
2169 the COMb distribution's  $\nu$  parameter at stimulus onset from around 1 to between 0 and 1 (see  
2170 figure 4.7a). A value of  $\nu$  less than 1 indicates positive association between the neurons (see  
2171 section 4.3.5). We might expect to see this positive association reflected in the correlation  
2172 coefficients, but this is not the case. We see no change in the time series of average correlation  
2173 measures at stimulus onset.

2174 This may be due to the very short time bin we used in this case. We know that using small  
2175 time bins can artificially reduce correlation measurements (Cohen and Kohn, 2011). In this  
2176 case, fitting the COMb distribution may be a useful way to measure association in a neuronal  
2177 ensemble over very short timescales (< 10ms).

2178 **4.4.4 Replicating stimulus related quenching of neural variability**

2179 Churchland et al. (2010) inspected the effect of a stimulus on neural variability. One of the  
2180 measures of neural variability that they employed was the Fano factor of the spike counts of  
2181 individual cells (see section 4.3.4). They found a reduction in neural variability as measured  
2182 by the Fano factor in various cortical areas in a macaque at the onset of various visual stimuli,  
2183 or a juice reward (Churchland et al., 2010).

2184 We measured the Fano factor of the spike count of each cell in each brain region, during  
2185 each trial. We measured the mean and standard error of these Fano factors from 500ms  
2186 before stimulus onset until 1000ms after stimulus end. For the primary visual cortex, we  
2187 found a transient reduction in the Fano factor immediately after stimulus onset. We used  
2188 a Mann-Whitney U test to check that the Fano factors measured in a window starting at

#### 4.4. Results

---

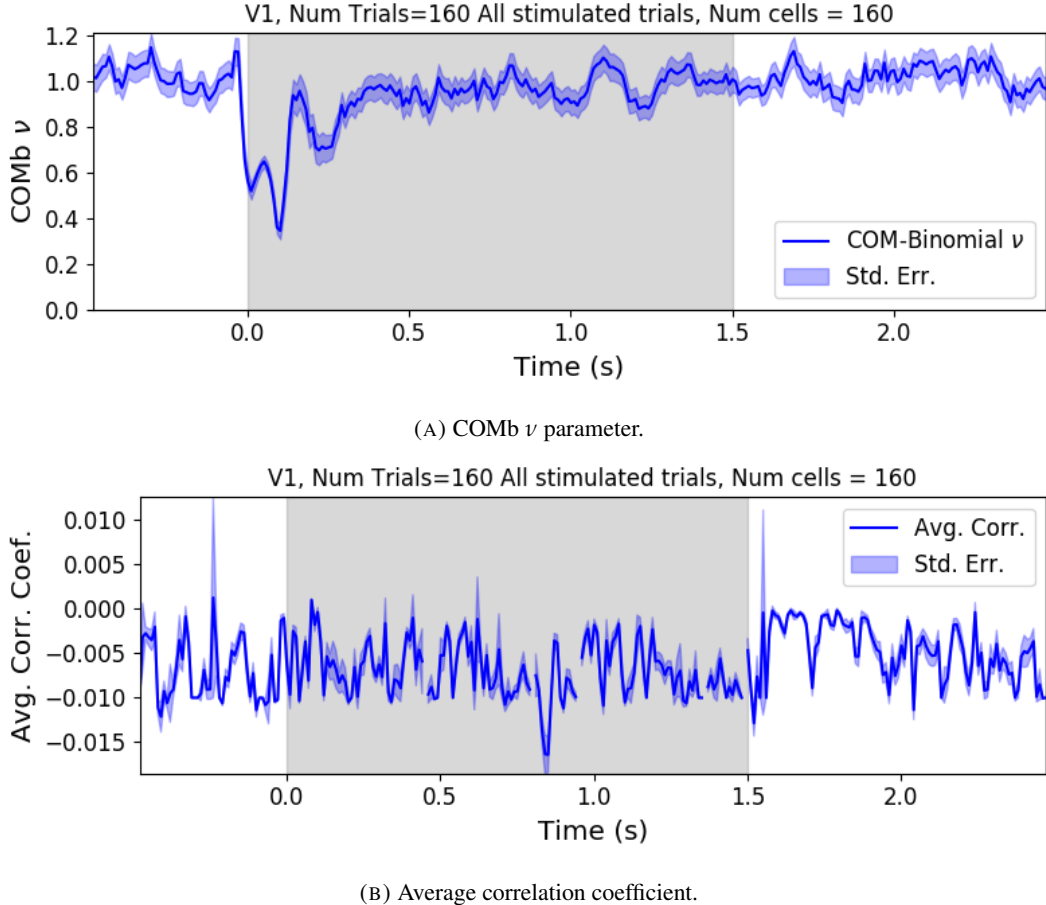


FIGURE 4.7: (A) We fit a Conway-Maxwell-binomial distribution to the number of active neurons in 1ms time bins of a 100ms sliding window. We did this for all trials with a visual stimulus and took the average across those trials. We see a transient drop in value for the distribution's  $\nu$  parameter at stimulus onset. This shows an increase in positive association between the neurons. (B) We measured the correlation coefficient between the spike counts of all possible pairs of neurons in the same sliding window. We took the average of those coefficients. We also did this for every visually stimulated trial, and took the average across trials. The increase in positive association is not reflected with an increase in average correlation.

stimulus onset and ending 100ms later were significantly lower than the factors measured in a window ending at stimulus onset ( $p < 0.001$ , see figure 4.8a). We did not get this statistically significant result in any other region.

Our findings agree with those of Churchland et al. for the primary visual cortex. However Churchland also found a reduction in the Fano factor in the dorsal premotor cortex (PMd) at stimulus onset. Our measurements from the mouse motor cortex show no change at stimulus onset (see figure 4.8b). This could indicate some difference in the functionality of the motor cortex in a macaque and the motor cortex of a mouse.

Similar to these findings in the Fano factor, we found a reduction in the  $\nu$  parameter of the COMB distribution on stimulus onset in V1 (figure 4.7a) and in no other region from

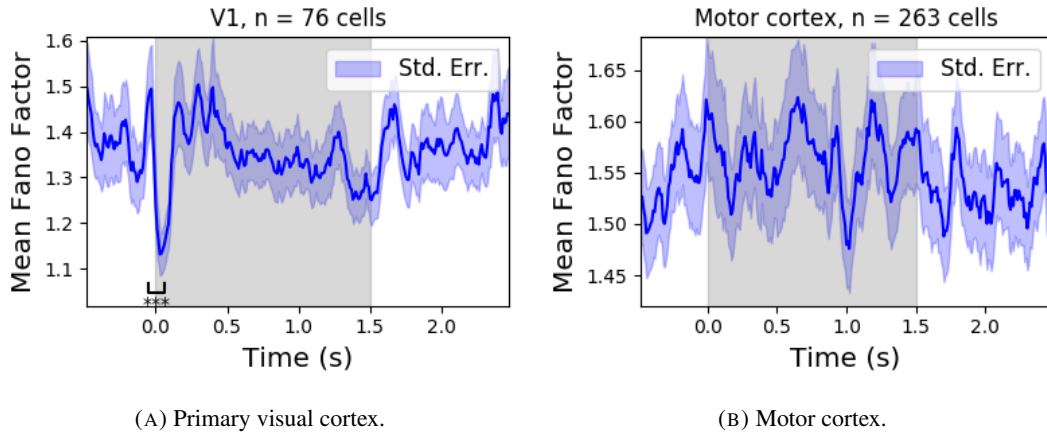


FIGURE 4.8: (A) The mean Fano factor of the spike counts of the cells in the primary visual cortex. Means were taken across cells first, then across trials. There was a significant decrease in the Fano factors immediately after stimulus onset. (B) The mean Fano factor of the spike counts of the cells in the motor cortex. No significant change in measurements at any point.

which we had data. Specifically, the  $\nu$  parameter reduced from around 1, to between 1 and 0. This represents a change from no association between the neurons, to a positive association. It is possible that this positive association may be responsible for the reduction in the Fano factor.

## 4.5 Discussion

Our aim in this research was to develop a new statistical method for analysing the activity of a neuronal ensemble at very short timescales. We wanted our method to use information taken from the whole ensemble, but we also wanted the method to be quick and easy to implement. It is likely that analysis methods with these characteristics will become valuable as electrophysiological datasets include readings from more cells over longer time periods. In this case, we used the number of active, or spiking, neurons in a very short time bin ( $< 10\text{ms}$ ) as a measure of ensemble activity.

First of all, we showed that there were changes in response that we could model at these very short time scales in some of the brain regions from which we had recordings. We observed changes in the average number of active neurons, and the variance of the number of active neurons in three different brain regions in response to visual stimuli. Since we know that correlated behaviour is associated with sensory perception (deCharms and Merzenich, 1996), we might hope to measure the pairwise correlations within the neuronal population in order to further investigate these responses. But, using such short time bins can produce

#### 4.5. Discussion

---

artificially small spike count correlation measurements (Cohen and Maunsell, 2009). Overcoming this limitation was one of our objectives for our new method. In order to do this, we abandoned the idea of measuring the correlations directly and embraced the concept of *association*. In order to quantify the association between neurons, we used the Conway-Maxwell-binomial distribution to model the number of active (spiking) neurons in an ensemble as a sum of possibly associated Bernoulli random variables.

We showed that the Conway-Maxwell-binomial distribution performed better than the more common options of the binomial and beta-binomial distributions. Furthermore, we showed that the positively associated behaviour between neurons in the primary visual cortex could be captured by fitting a Conway-Maxwell-binomial distribution, but was not captured by the more standard approach of measuring the spike count correlation. The associated behaviour could not be measured using spike count correlations, because of the very short bins required to capture short timescale behaviour.

We replicated a famous result from Churchland et al (2010) relating to the quenching of neural variability in cortical areas at stimulus onset, and in doing so, we established a correspondence between the association quantifying parameter of the Conway-Maxwell-binomial (COMb) distribution and the neural variability as measured by the Fano factor. We found a reduction in the  $\nu$  parameter of the COMB distribution at stimulus onset, indicating a change from no association to positive association between neurons in V1. We found a corresponding reduction in the Fano factor of the individual cells in V1. The positive association between neurons induced by the stimulus would constrain the neurons to fire at the same time. The stimulus also induced a larger number of neurons to spike. These two actions combined could cause an increase in the firing rate of individual cells that is greater in magnitude than the increase in firing rate variability. If this is indeed the case, then the association as captured by the COMB distribution could be regarded as one of the ‘natural parameters’ of the ensemble response for short timescales. That is, a quantity that directly measures some aspect of the behaviour of the ensemble. In this case, it the correlated behaviour of the individual neurons is captured.

This work could be just a first step in creating analysis methods based on the Conway-Maxwell-binomial distribution, or similar statistical models. One way to extend the method would be to pair it up with the ‘Population Tracking model’ (O’Donnell et al., 2017). This model attempts to characterise the interaction between an ensemble and each member of the ensemble by quantifying the probability of spiking for a given a cell, given the number of active cells in the whole population. Combining this model with the COMB distribution

2252 would give us a model that could accurately fit the number of active neurons at any moment,  
2253 and that gives a probability of firing for each cell, and therefore probabilities for full spiking  
2254 patterns, without adding a huge number of parameters to fit.

2255 A more complex way to extend the model would be to fit a Conway-Maxwell-binomial  
2256 distribution to data recorded from multiple brain regions simultaneously, with a different fit  
2257 for each region, then to analyse the temporal relationship between the fitted parameters of  
2258 each region. If we analysed the time series of the COMB distribution parameters from the  
2259 different regions, looking at cross-correlations between regions, this may give some results  
2260 relating to the timescales in which information is processed in different brain regions.

2261 **Chapter 5**

2262 **Studies with practical limitations &**  
2263 **negative results**

2264 *Abstract*

2265 Here I will present some details on research topics that I started, but that unfortunately did not  
2266 lead anywhere useful. There are two pieces of research, based on two papers. Each paper is  
2267 related to the overall theme of my PhD of analysing and modelling behaviours of populations  
2268 of neurons. The first part is based on a model of parallel spike trains including higher order  
2269 interactions by Shimazaki et al (2012). The second part is based on a multiscale model for  
2270 making inferences on hierarchical data.

2271 **5.1 Dynamic state space model of pairwise and higher order neu-**  
2272 **ronal correlations**

2273 In their paper Shimazaki et al (2012) aimed to model spike trains from populations of neurons  
2274 in parallel, with pairwise and higher order dynamic interactions between the trains. They  
2275 modelled the spike trains as multi-variate binary processes using a log-linear model, and they  
2276 extracted spike interaction parameters using a Bayesian filter/EM-algorithm. They developed  
2277 a goodness-of-fit measure for the model to test if including these higher order correlations  
2278 is necessary for an accurate model. Their measure was based on the Bayes factor but they  
2279 also assessed the suitability of higher order models using the AIC and BIC. So the increase  
2280 in the number of parameters associated with fitting higher order interactions was taken into  
2281 account. They tested the performance of the model on synthetic data with known higher  
2282 order correlations. They used the model to look for higher order correlations in data from  
2283 awake behaving animals. They use the model to demonstrate dynamic appearance of higher  
2284 order correlations in the monkey motor cortex (Shimazaki et al., 2012).

2285 We used the available Python repository to implement the model, and we successfully  
2286 worked through the tutorial provided. But we found that the model did not scale well to  
2287 larger populations. We attempted to fit the model to a population of 10 neurons and found we  
2288 didn't manage to finish the process. Since, our goal was to find a model to scale to hundreds  
2289 or thousands of neurons, we decided that this model was no longer worth pursuing.

2290 **5.2 A multiscale model for hierarchical data applied to**  
2291 **neuronal data**

2292 In their paper Kolaczyk et al (2001) developed a framework for a modelling hierarchically  
2293 aggregated data, and making inferences based on a model arising from this framework. They  
2294 assumed that a hierarchical aggregation existed on the data in question, where each element at  
2295 each level of the hierarchy had some associated measurements, an associated mean process,  
2296 which was the expected value of these measurements. They also assumed that the measure-  
2297 ments of each parent were equal to the sum of the measurements from all of its children.  
2298 They showed that these assumptions gave rise to a relationship between parent and child  
2299 measurements across all levels of the hierarchy, where the product of the likelihood of the  
2300 parameters of the lowest level of the hierarchy can be expressed as products of conditional  
2301 likelihoods of the elements of higher levels of the hierarchy (Kolaczyk and Huang, 2010).

2302 They gave examples of these expressions for measurements sampled from Gaussian dis-  
2303 tributions, and Poisson distributions, and showed the definitions of the hierarchical param-  
2304 eters which reparametrise the distribution of these data taking the hierarchy into account.  
2305 They go on to suggest prior distributions for this multiscale model, and integrate these priors  
2306 to give posterior distributions for the measurements from each element at each level in the hi-  
2307 erarchy, and expressions for the MAP estimated parameters of each the associated processes  
2308 (Kolaczyk and Huang, 2010).

2309 We implemented their model in Python by creating some synthetic data from Poisson  
2310 distributions, and defining a hierarchy by agglomerating these data. We calculated the MAP  
2311 estimates using our knowledge of the hierarchy, and using the expressions given in the paper.  
2312 We found that the MAP estimates were far less accurate than would be achieved by simply  
2313 ignoring the hierarchy during estimation, and using a maximum likelihood approach. After  
2314 that, we decided to move on.



2315 **Chapter 6**

2316 **Discussion**

2317 In this project, we attempted to address some of the challenges in data collection from  
2318 large neuronal ensembles (specifically with calcium imaging) and some of the problems in  
2319 analysing the data collected from large neuronal ensembles.

2320 Firstly, we investigated the relationship between cell biochemistry, action potentials and  
2321 the fluorescence traces produced by fluorescent calcium indicators. We did this by building  
2322 a biophysical model that takes in a spike train and returns the fluorescence trace that that  
2323 spike would induce. The model included mechanics for the binding of calcium to fluorescent  
2324 and endogenous mobile and immobile buffers, and the consequent changes in concentration  
2325 of free and bounded calcium. The model consisted of 17 parameters, 13 of which were  
2326 set according to data from the literature, and 4 of which were free parameters. We trained  
2327 the model using simultaneously collected spiking and calcium imaging data (Berens et al.,  
2328 2018). We fitted the model by matching the  $\Delta F/F_0$  in response to an action potential, and  
2329 by matching the power spectrum of the actual fluorescence trace. This meant that our model  
2330 would include the correct amount of noise as well as return the correct change in amplitude  
2331 in response to an action potential.

2332 Since our model produced fluorescence traces, we could apply spike inference algorithms  
2333 to the modelled fluorescence traces that our model produced after training, and compare the  
2334 performance of the algorithms on the modelled traces to their performance on the real traces.  
2335 We used three spike inference algorithms, two of which were based on modelling the cal-  
2336 cium trace as an autoregression (Friedrich and Paninski, 2016; Pnevmatikakis et al., 2016),  
2337 and another inference algorithm that was a little more biologically inspired, but amounted to  
2338 a very similar algorithm (Deneux et al., 2016). We compared the performance of the algo-  
2339 rithms by using them to infer spikes from 20 real and modelled fluorescence traces induced  
2340 by 20 corresponding real spike trains. We then used several binary classification measures  
2341 (true positive rate, accuracy etc.) to asses the quality of the spike inference for the real and

2342 modelled fluorescence traces. We found that the spike inference algorithms performed sim-  
2343 ilarly on real and modelled traces, showing that our model is capturing at least some of the  
2344 characteristics of the real fluorescence traces.

2345 In order to investigate the effect of indicator characteristics on the modelled fluorescence  
2346 trace and spike inference quality, we perturbed the indicator's affinity and dissociation rate  
2347 in parallel, keeping the ratio of the two the same for all perturbations. We measured the SNR  
2348 of the trace, and the true positive rate of the spike inference algorithms at each perturbed  
2349 value pair. We found that perturbing the values lower caused in decrease in SNR and spike  
2350 inference quality. This shows that our model could be used to test theoretical fluorescent cal-  
2351 cium indicators without having to actually manufacture them. Experimental neuroscientists  
2352 could also use our model to judge which indicator characteristics are most influential in their  
2353 experimental context.

2354 We then investigated the effect of perturbing buffer concentration, and indicator concen-  
2355 tration, on the signal-to-noise ratio of the modelled fluorescence trace and spike inference  
2356 quality. This was a worthwhile experiment because endogenous buffer concentrations vary  
2357 from cell to cell (Bartol et al., 2015; Maravall et al., 2000; Neher and Augustine, 1992), as  
2358 does indicator expression (Chen et al., 2013). We found that extreme perturbations away  
2359 from the indicator concentration taken from the literature lowered the SNR of the trace, and  
2360 the spike inference quality. We also found that increases in the concentration of endogenous  
2361 buffer above the value taken from the literature caused a decrease in the SNR and spike infer-  
2362 ence quality. This reiterates that the indicator and endogenous buffers compete to bind with  
2363 free calcium molecules, and this has an effect on fluorescence and consequently on spike  
2364 inference.

2365 We then created some synthetic spike trains with controlled mean firing rates sampled  
2366 the rates from an Ornstein-Uhlenbeck process. We found that the higher the firing rate, the  
2367 lower the accuracy of the spike inference algorithms. But the mean firing could perhaps be  
2368 inferred from the amplitude of the fluorescence traces. The higher firing rate, the higher the  
2369 amplitude. Calibrating the model to facilitate and accurate measurement would require some  
2370 kind of ground truth, but relative comparisons could be made without any other knowledge  
2371 of the underlying spiking process.

2372 One obvious limitation to our model is the lack of binding mechanics for both the indi-  
2373 cator and endogenous buffers. Greenberg et al included these mechanics in their successful  
2374 spike inference model. We felt that the timescale of these binding mechanics was so small in  
2375 comparison to the fluorescence dynamics that omitting them would make no difference. But

2376 it is possible that their inclusion would improve our model.

2377 After investigating the difficulties with inferring spiking data from calcium imaging data,  
2378 we moved from data collection to analysis and we decided to implement a new network anal-  
2379 ysis method on data from a neuronal ensemble. Using an electrophysiological dataset with  
2380 spike sorted data from 9 different brain regions in 3 mice (Steinmetz, Carandini, and Harris,  
2381 2019), we binned the spike times for each cell into spike counts for each cell and measured  
2382 the correlation coefficients between these spike counts for a selection of cells evenly dis-  
2383 tributed across the 9 regions. We repeated these measurements for time bin widths ranging  
2384 from 5ms to 3s. We rectified these measurements and, for a given time bin width, used them  
2385 as weights for a weighted undirected graph where each node represents a neuron, and the  
2386 weight of each edge is the correlation between the neurons represented by the nodes on that  
2387 edge. We applied a novel spectral analysis and community detection method (Humphries  
2388 et al., 2019) to this network. This clustered the nodes in our ensemble into communities  
2389 whose behaviour was more correlated than expected. Our measure of 'expected correlation  
2390 strength' were based on a random network that matched our data network's sparsity and total  
2391 weight. We compared the detected communities to the anatomical division of our cells using  
2392 clustering comparison measures. We then conditioned the binned spike counts on the be-  
2393 haviour of the mouse using the principal components of a video of the mouses face recorded  
2394 simultaneously with the electrophysiology. We broke the total covariance down into 'spike  
2395 count covariance' and 'signal covariance' components conditioning on the behavioural data  
2396 and using the law of total covariance. We then repeated our analysis for spike count corre-  
2397 lations, and signal correlation. Finally, since our community detection method was only valid  
2398 on graphs with non-negative weights, we used different methods for creating a non-negative  
2399 graph from our total correlations, and we repeated our analysis on those graphs.

2400 Our first finding was that the time bin width used to bin spike times into spike counts had  
2401 a effect on the mean magnitude of the correlations measured. The wider the bin, the higher  
2402 the correlations. Not only that, we separated the pairs into positively and negative correlated  
2403 pairs, and we found that positively correlated pairs have greater correlation coefficients when  
2404 using a wider bin, and negatively correlated pairs have more negative correlation coefficients  
2405 when using a wider bin. We also found that the width of the bin used had an effect on the  
2406 distribution of the spike counts. For smaller bin widths, the distribution of spike counts was  
2407 better represented by a skewed distribution like the Poisson distribution. For wider bins, the  
2408 spike counts were better represented by a Gaussian distribution.

2409 Next we investigated the differences between correlations within regions and between

regions. When we divided the pairs according to those two groups, we found that the mean within-region correlations were higher at every bin width, and the difference between the two means grew with increasing bin width. When we split the pairs of cells according to their regions, we found that the mean within-region correlations in any given region were usually greater than the mean between-region correlations for any region pair involving that region. The difference between the mean within-region correlation and the highest between-region correlations involving that region grew smaller with increasing bin width. To investigate this further, we plotted these mean correlations in matrices. Although the mean within-region correlations were usually the highest value in their row or column, as the bin width increased, the mean between-region correlations grew in magnitude relative to the within-region figure.

Next we chose a null network model, and we used the ‘Network Noise Rejection’ process (Humphries et al., 2019) to check for additional structure in our correlation based data network that was not captured by the null model. We found additional structure for any bin width that we used. We also found that the dimensionality of the additional structure reduced as we increased the bin width. This could mean that the processes or representations that take place over longer timescales within the brain also take place in a lower dimensional space.

We applied a community detection method (Humphries, 2011) to the signal correlation networks arising from the network noise rejection. We found that the number of communities detected decreased with increasing bin width. We also noticed that at shorter bin widths, the detected communities were more likely to consist of cells from one brain region only. We investigated this further by using clustering comparison methods to compare the detected communities with the anatomical division of the cells. We found that for short timescales  $< 50\text{ms}$  correlated communities tended to exist within anatomical regions, and for longer timescales  $> 100\text{ms}$ , the correlated communities tended to exist across anatomical regions. This is broadly in agreement with a similar finding for EEG data from humans performing semantic or memory tasks (Stein and Sarnthein, 2000). Von Stein et al. (2000) found that visual processing taking place locally in the visual system was captured in the gamma frequency range (25 – 70Hz), while semantic processing was captured in the beta range (12 – 18Hz), and tasks involving mental imagery and working memory retention were captured in the theta and alpha ranges (4 – 8Hz, and 8 – 12Hz respectively).

We then conditioned our correlation measures on the the mouse’s behaviour. This allowed us to create spike count correlation (or noise correlation) networks, and signal correlation networks (Cohen and Kohn, 2011). We applied our analysis to these networks. For the

2443 spike count correlation networks we found very similar results to the total correlation net-  
2444 works. More communities at smaller bin widths, and communities resembled the anatomical  
2445 division at smaller bin widths. Given that recent findings show that behaviour can account  
2446 for correlated spiking in many areas of the brain (Stringer et al., 2019), these results for the  
2447 spike count correlation show that this correlated behaviour is still processed locally at short  
2448 timescales, while processes and representations that take more time make use of correlated  
2449 activity across multiple regions.

2450 For the signal correlations, we still found additional structure in these networks. But we  
2451 always detected a smaller number of communities. These communities also had no relation  
2452 to the anatomical division of the cells. This result shows that there are groups of cells across  
2453 multiple brain regions that are activated similarly by certain behaviours.

2454 All of the networks so far were based on rectified correlation measures, because the  
2455 network noise rejection and community detection processing is (currently) only valid for  
2456 networks with non-negative weights. For the final part of our analysis, we tried different  
2457 ways of transforming our total correlations into non-negative quantities before applying our  
2458 analysis. First of all we took the absolute value of our correlation measures. Our results were  
2459 very similar to those for the rectified correlations with the exception that we detected more  
2460 communities consistently. It is possible that using this method detects both positively and  
2461 negatively correlated communities.

2462 We also tried reversing the sign of all the correlations, then rectifying the network. We  
2463 hope that this would allow us to detect the negatively correlated communities. We did detect  
2464 communities in these networks, but never more than three, and these communities bore no  
2465 relationship with the anatomical distribution of the cells.

2466 There is a lot of potential for network science applications in computational neuroscience.  
2467 For example, some pairwise measure other than correlation coefficients could be used as the  
2468 weights of the graph. A directed measure like synaptic connectivity could be used as the basis  
2469 for directed graphs. The analysis methods applicable to directed graphs could give insights  
2470 about the formation of synaptic connections, or the dynamic changes in these connections  
2471 over time. Other methods of community detection could be used on directed or undirected  
2472 graphs. We used a ‘hard’ clustering method in our research, that is, each neuron could be  
2473 a member of one cluster/community only. ‘Fuzzy-clustering’ methods do exist, where each  
2474 element of the set to be clustered could be a member of more than one cluster (Baadel,  
2475 Thabtah, and Lu, 2016).

2476 Having spent much time investigating correlated behaviour using coefficients of spike

counts, we decided to try another method for capturing correlated behaviour in neuronal ensembles. We used electrophysiological data taken from 5 brain regions of an awake mouse exposed to visual stimuli (Steinmetz et al., 2019). We modelled the number of active neurons in a given brain region as the number of successes in a collection of dependent Bernoulli random variables using the Conway-Maxwell-binomial distribution. To avoid violating the Bernoulli assumption, we binned the spike times using 1ms bins. The Conway-Maxwell-binomial distribution is a two parameter extension of the standard binomial distribution. The extra parameter allows the distribution to capture possible positive or negative association between the Bernoulli trials (Kadane, 2016). This means that we are assuming that all the neurons are dependent in the same way. This is not an accurate assumption, but it allows us model the data in a simple way.

First of all we established that there were changes in the number of active neurons in response to the visual stimuli. This was the case in the hippocampus, thalamus, and primary visual cortex. Each region had its own signature response. We measured the mean and variance of the number of active neurons in a sliding window starting before stimulus onset, and finishing after the end of stimulus presentation.

As well as the Conway-Maxwell-binomial distribution, we also fitted binomial, and beta-binomial distributions to the number of active neurons in a sliding window. We found that the Conway-Maxwell-binomial distribution was the best fit for over 90% of the samples. This means that the COMb distribution is capturing some dependency between the neurons, because the binomial distribution assumes independence. Also the COMb distribution captures this dependence more accurately than the beta-binomial distribution, which does have some capacity for over dispersion.

Next we showed that the Conway-Maxwell-binomial distribution captured the change in association at stimulus onset better than the correlation coefficient. The extremely small bin width artificially shrunk the correlation coefficient to the point where this measurement didn't detect any correlated activity. But the association parameter of the COMb distribution detected some positive association between the neurons at stimulus onset. So, for particularly short time bins, where neurons can be treated as Bernoulli random variables, the Conway-Maxwell-binomial distribution is a good way to capture correlated behaviour. There are other measurements for capturing association to which this distribution should be compared. Cross-correlograms could be used for some measure of synchrony, for example.

Finally, we replicated a famous finding of Churchland et al. (2010) relating to the quenching of neural variability at stimulus onset, thereby finding a parallel between this reduction

2511 in the Fano factor and a reduction in the association parameter of the COMb distribution.

2512 We showed that computational neuroscientists can make progress by being inventive with  
2513 their statistical models. A similar distribution to investigate would be the Conway-Maxwell-  
2514 Poisson distribution. This is similar to the standard Poisson distribution, but with an addi-  
2515 tional parameter that allows for over- or under- dispersion relative to a Poisson distribution.  
2516 This might be ideal for modelling firing rates of individual neurons. Some interaction be-  
2517 tween the fitted parameters could capture the association between neurons.

2518 There is one technology that has the potential to take over from both electrophysiology  
2519 and calcium imaging. The technique of voltage imaging has become more useful in recent  
2520 years. The aim for neuroscience would be to develop a voltage imaging dye or protein that  
2521 images the membrane potential of a neuron with enough spatial and temporal resolution to  
2522 detect action potentials. Genetically encoded voltage indicators have been developed, and  
2523 enable targeting of specific neuronal ensembles. But their spatial resolution is not yet high  
2524 enough to single out individual cells (Bando et al., 2019). These indicators have the potential  
2525 to take over from calcium imaging, and if imaging deep within the brain becomes possible,  
2526 electrophysiology could also be replaced. This is speculation, but the potential is there.



# <sup>2527</sup> Bibliography

- <sup>2528</sup> Allen, William E. et al. (2019). “Thirst regulates motivated behavior through modulation of  
<sup>2529</sup> brainwide neural population dynamics”. In: *Science* 364.6437.
- <sup>2530</sup> Baadel, S., F. Thabtah, and J. Lu (2016). “Overlapping clustering: A review”. In: *2016 SAI*  
<sup>2531</sup> *Computing Conference (SAI)*, pp. 233–237.
- <sup>2532</sup> Baldassano, Christopher et al. (2017). “Discovering Event Structure in Continuous Narrative  
<sup>2533</sup> Perception and Memory”. In: *Neuron* 95.3, 709 –721.e5.
- <sup>2534</sup> Bando, Yuki et al. (2019). “Genetic voltage indicators”. In: *BMC Biology* 17.1, p. 71.
- <sup>2535</sup> Bartol, Thomas M. et al. (2015). “Computational reconstitution of spine calcium transients  
<sup>2536</sup> from individual proteins”. In: *Frontiers in Synaptic Neuroscience* 7, p. 17.
- <sup>2537</sup> Berens, Philipp et al. (May 2018). “Community-based benchmarking improves spike rate in-  
<sup>2538</sup> ference from two-photon calcium imaging data”. In: *PLOS Computational Biology* 14.5,  
<sup>2539</sup> pp. 1–13.
- <sup>2540</sup> Bezanson, Jeff et al. (Sept. 2012). “Julia: A Fast Dynamic Language for Technical Comput-  
<sup>2541</sup> ing”. In: *MIT*.
- <sup>2542</sup> Buccino, Alessio P. et al. (2019). “SpikeInterface, a unified framework for spike sorting”. In:  
<sup>2543</sup> *bioRxiv*.
- <sup>2544</sup> Chen, Tsai-Wen et al. (July 2013). “Ultrasensitive fluorescent proteins for imaging neuronal  
<sup>2545</sup> activity”. In: *Nature* 499, 295–300.
- <sup>2546</sup> Churchland, Mark M. et al. (2010). “Stimulus onset quenches neural variability: a widespread  
<sup>2547</sup> cortical phenomenon”. eng. In: *Nature neuroscience* 13.3. 20173745[pmid], pp. 369–378.
- <sup>2548</sup> Cohen, Marlene R. and Adam Kohn (2011). “Measuring and interpreting neuronal corre-  
<sup>2549</sup> lations”. In: *Nature Neuroscience* 14.7, pp. 811–819.
- <sup>2550</sup> Cohen, Marlene R. and John H. R. Maunsell (2009). “Attention improves performance pri-  
<sup>2551</sup> marily by reducing interneuronal correlations”. eng. In: *Nature neuroscience* 12.12. 19915566[pmid],  
<sup>2552</sup> pp. 1594–1600.
- <sup>2553</sup> Dana, Hod et al. (Sept. 2014). “Thy1-GCaMP6 Transgenic Mice for Neuronal Population  
<sup>2554</sup> Imaging In Vivo”. In: *PloS one* 9, e108697.

- 2555 deCharms, R. Christopher and Michael M. Merzenich (1996). “Primary cortical representation of sounds by the coordination of action-potential timing”. In: *Nature* 381.6583,  
2556 pp. 610–613.
- 2558 Deneux, Thomas et al. (July 2016). “Accurate spike estimation from noisy calcium signals  
2559 for ultrafast three-dimensional imaging of large neuronal populations in vivo”. In: *Nature  
2560 Communications* 7.1.
- 2561 Dombeck, Daniel A. et al. (2010). “Functional imaging of hippocampal place cells at cellular  
2562 resolution during virtual navigation”. In: *Nature Neuroscience* 13.11, pp. 1433–1440.
- 2563 Éltes, Tímea et al. (2019). “Improved spike inference accuracy by estimating the peak am-  
2564 plitude of unitary [Ca<sub>2+</sub>] transients in weakly GCaMP6f-expressing hippocampal pyra-  
2565 midal cells”. In: *The Journal of Physiology* 597.11, pp. 2925–2947.
- 2566 Faas, Guido C. et al. (2011). “Calmodulin as a direct detector of Ca<sub>2+</sub> signals”. In: *Nature  
2567 Neuroscience* 14.3, pp. 301–304.
- 2568 Fiala, John C. and Kristen M. Harris (1999). *Dendrite Structure*.
- 2569 Flach, Boris (Sept. 2013). “A Class of Random Fields on Complete Graphs with Tractable  
2570 Partition Function”. In: *IEEE transactions on pattern analysis and machine intelligence*  
2571 35, pp. 2304–6.
- 2572 Forney, G. D. (1973). “The viterbi algorithm”. In: *Proceedings of the IEEE* 61.3, pp. 268–  
2573 278.
- 2574 Fosdick, Bailey et al. (Aug. 2016). “Configuring Random Graph Models with Fixed Degree  
2575 Sequences”. In: *SIAM Review* 60.
- 2576 Friedrich, Johannes and Liam Paninski (2016). “Fast Active Set Methods for Online Spike In-  
2577 ference from Calcium Imaging”. In: *Advances in Neural Information Processing Systems*  
2578 29. Ed. by D. D. Lee et al. Curran Associates, Inc., pp. 1984–1992.
- 2579 Ganmor, Elad, Ronen Segev, and Elad Schneidman (2011). “Sparse low-order interaction  
2580 network underlies a highly correlated and learnable neural population code”. In: *Pro-  
2581 ceedings of the National Academy of Sciences* 108.23, pp. 9679–9684.
- 2582 Girard, P., J. M. Hupé, and J. Bullier (2001). “Feedforward and Feedback Connections Be-  
2583 tween Areas V1 and V2 of the Monkey Have Similar Rapid Conduction Velocities”. In:  
2584 *Journal of Neurophysiology* 85.3. PMID: 11248002, pp. 1328–1331.
- 2585 Greenberg, David et al. (Nov. 2018). “Accurate action potential inference from a calcium  
2586 sensor protein through biophysical modeling:” in:
- 2587 Gründemann, Jan et al. (2019). “Amygdala ensembles encode behavioral states”. In: *Science*  
2588 364.6437.

## Bibliography

---

- 2589 Hodgkin, A. L. and A. F. Huxley (1939). “Action Potentials Recorded from Inside a Nerve  
2590 Fibre”. In: *Nature* 144.3651, pp. 710–711.
- 2591 Humphries, Mark et al. (Jan. 2019). “Spectral rejection for testing hypotheses of structure in  
2592 networks”. In:
- 2593 Humphries, Mark D. (2011). “Spike-Train Communities: Finding Groups of Similar Spike  
2594 Trains”. In: *Journal of Neuroscience* 31.6, pp. 2321–2336.
- 2595 Jun, James J. et al. (2017). “Fully integrated silicon probes for high-density recording of  
2596 neural activity”. In: *Nature* 551.7679, pp. 232–236.
- 2597 Kadane, Joseph B. (June 2016). “Sums of Possibly Associated Bernoulli Variables: The  
2598 Conway–Maxwell-Binomial Distribution”. In: *Bayesian Anal.* 11.2, pp. 403–420.
- 2599 Kilhoffer, Marie-Claude et al. (Sept. 1992). “Use of Engineered Proteins With Internal Tryp-  
2600 topahan Reporter Groups and Perturbation Techniques to Probe the Mechanism of Ligand-  
2601 Protein Interactions: Investigation of the Mechanism of Calcium Binding to Calmodulin”.  
2602 In: *Biochemistry* 31.34, pp. 8098–8106.
- 2603 Koch, Christoff (1999). *Biophysics of Computation: Information Processing in Single Neu-  
2604 rons*. Oxford University Press.
- 2605 Kolaczyk, Eric and Haiying Huang (Sept. 2010). “Multiscale Statistical Models for Hierar-  
2606 chical Spatial Aggregation”. In: *Geographical Analysis* 33, pp. 95 –118.
- 2607 Lee, Suk-HO et al. (July 2000). “Differences in Ca<sup>2+</sup> buffering properties between excitatory  
2608 and inhibitory hippocampal neurons from the rat”. In: *The Journal of Physiology* 525.
- 2609 Litwin-Kumar, Ashok, Maurice Chacron, and Brent Doiron (Sept. 2012). “The Spatial Struc-  
2610 ture of Stimuli Shapes the Timescale of Correlations in Population Spiking Activity”. In:  
2611 *PLoS computational biology* 8, e1002667.
- 2612 Maravall, M et al. (May 2000). “Estimating intracellular calcium concentrations and buffer-  
2613 ing without wavelength ratioing”. In: *Biophysical Journal* 78.5, pp. 2655–2667.
- 2614 Maugis, Pa (Jan. 2014). “Event Conditional Correlation: Or How Non-Linear Linear Depen-  
2615 dence Can Be”. In:
- 2616 Meilă, Marina (2007). “Comparing clusterings—an information based distance”. In: *Journal  
2617 of Multivariate Analysis* 98.5, pp. 873 –895.
- 2618 Murray, John D. et al. (2014). “A hierarchy of intrinsic timescales across primate cortex”. In:  
2619 *Nature Neuroscience* 17.12, pp. 1661–1663.
- 2620 Neher, E. and G. J. Augustine (1992). “Calcium gradients and buffers in bovine chromaffin  
2621 cells”. eng. In: *The Journal of physiology* 450. 1331424[pmid], pp. 273–301.

- 2622 O'Donnell, Cian et al. (Jan. 2017). "The population tracking model: a simple, scalable statistical model for neural population data". English. In: *Neural Computation* 29.1, pp. 50–93.
- 2625 Okun, Michael et al. (2015). "Diverse coupling of neurons to populations in sensory cortex". In: *Nature* 521.7553, pp. 511–515.
- 2627 Ouzounov, Dimitre G. et al. (2017). "In vivo three-photon imaging of activity of GCaMP6-labeled neurons deep in intact mouse brain". eng. In: *Nature methods* 14.4. 28218900[pmid], pp. 388–390.
- 2630 Patterson, Carolyn A. et al. (2014). "Similar adaptation effects in primary visual cortex and area MT of the macaque monkey under matched stimulus conditions". In: *Journal of Neurophysiology* 111.6. PMID: 24371295, pp. 1203–1213.
- 2633 Peron, Simon P. et al. (2015). "A Cellular Resolution Map of Barrel Cortex Activity during Tactile Behavior". In: *Neuron* 86.3, pp. 783–799.
- 2635 Pnevmatikakis, E.A. et al. (Jan. 2016). "Simultaneous Denoising, Deconvolution, and Demixing of Calcium Imaging Data". In: *Neuron* 89.2, pp. 285–299.
- 2637 Pnevmatikakis, Eftychios et al. (Nov. 2013). "Bayesian spike inference from calcium imaging data". In: *Conference Record - Asilomar Conference on Signals, Systems and Computers*.
- 2639 Pnevmatikakis, Eftychios et al. (Sept. 2014). "A structured matrix factorization framework for large scale calcium imaging data analysis". In:
- 2641 Schneidman, Elad et al. (2006). "Weak pairwise correlations imply strongly correlated network states in a neural population". eng. In: *Nature* 440.7087. 16625187[pmid], pp. 1007–1012.
- 2644 Shannon, C. E. (1948). "A Mathematical Theory of Communication". In: *Bell System Technical Journal* 27.3, pp. 379–423.
- 2646 Shimazaki, Hideaki et al. (2012). "State-space analysis of time-varying higher-order spike correlation for multiple neural spike train data". eng. In: *PLoS computational biology* 8.3. 22412358[pmid], e1002385–e1002385.
- 2649 Staude, Benjamin, Sonja Grün, and Stefan Rotter (2010). "Higher-Order Correlations and Cumulants". In: *Analysis of Parallel Spike Trains*. Ed. by Sonja Grün and Stefan Rotter. Boston, MA: Springer US, pp. 253–280.
- 2652 Stein, Astrid von and Johannes Sarnthein (2000). "Different frequencies for different scales of cortical integration: from local gamma to long range alpha/theta synchronization". In: *International Journal of Psychophysiology* 38.3, pp. 301 –313.

## Bibliography

---

- 2655 Steinmetz, Nick, Matteo Carandini, and Kenneth D. Harris (2019). "Single Phase3" and  
2656 "Dual Phase3" *Neuropixels Datasets*.
- 2657 Steinmetz, Nick et al. (Mar. 2019). "Eight-probe Neuropixels recordings during spontaneous  
2658 behaviors". In:
- 2659 Stevenson, Ian H. and Konrad P. Kording (2011). "How advances in neural recording affect  
2660 data analysis". In: *Nature Neuroscience* 14.2, pp. 139–142.
- 2661 Stringer, Carsen et al. (2019). "Spontaneous behaviors drive multidimensional, brainwide  
2662 activity". In: *Science* 364.6437.
- 2663 Tada, Mayumi et al. (2014). "A highly sensitive fluorescent indicator dye for calcium imaging  
2664 of neural activity in vitro and in vivo". In: *European Journal of Neuroscience* 39.11,  
2665 pp. 1720–1728.
- 2666 Tian, Lin et al. (2009). "Imaging neural activity in worms, flies and mice with improved  
2667 GCaMP calcium indicators". eng. In: *Nature methods* 6.12. 19898485[pmid], pp. 875–  
2668 881.
- 2669 Tkačik, Gašper et al. (2014). "Searching for collective behavior in a large network of sen-  
2670 sory neurons". eng. In: *PLoS computational biology* 10.1. 24391485[pmid], e1003408–  
2671 e1003408.
- 2672 Treves, Alessandro and Stefano Panzeri (1995). "The Upward Bias in Measures of Informa-  
2673 tion Derived from Limited Data Samples". In: *Neural Computation* 7.2, pp. 399–407.
- 2674 Vinh, Nguyen Xuan, Julien Epps, and James Bailey (Dec. 2010). "Information Theoretic  
2675 Measures for Clusterings Comparison: Variants, Properties, Normalization and Correc-  
2676 tion for Chance". In: *J. Mach. Learn. Res.* 11, 2837–2854.
- 2677 Vogelstein, Joshua T. et al. (Oct. 2010). "Fast nonnegative deconvolution for spike train infer-  
2678 ence from population calcium imaging". In: *Journal of neurophysiology* 104.6, 295–300.
- 2679 Wierzynski, Casimir M. et al. (2009). ""State-Dependent Spike-Timing Relationships be-  
2680 tween Hippocampal and Prefrontal Circuits during Sleep"". In: "Neuron" "61" ."4", "587  
2681 –596".
- 2682 Zariwala, Hatim A. et al. (2012). "A Cre-dependent GCaMP3 reporter mouse for neuronal  
2683 imaging in vivo". eng. In: *The Journal of neuroscience : the official journal of the Society  
2684 for Neuroscience* 32.9. 22378886[pmid], pp. 3131–3141.
- 2685 Zou, Hui and Trevor Hastie (2005). "Regularization and variable selection via the Elastic  
2686 Net". In: *Journal of the Royal Statistical Society, Series B* 67, pp. 301–320.